Institut für Theoretische Physik
Fakultät Mathematik und Naturwissenschaften
Technische Universität Dresden

Active Chiral Processes in Soft Biological Matter

Dissertation

Zur Erlangung des akademischen Grades

Doctor rerum naturalium
(Dr. rer. nat.)

vorgelegt von

Sebastian Fürthauer

geboren am 29.7.1980 in Wien

Max-Planck-Institut für
Physik komplexer Systeme

Dresden, 2012

Gutachter 1: Prof. Dr. Frank Jülicher

Gutachter 2: Prof. Dr. Holger Stark

eingereicht den: 26.03.2012

verteidigt den: 15.05.2012

Abstract

Biological matter is driven far from thermodynamic equilibrium by active processes on the molecular scale. These processes are usually driven by the chemical reaction of a fuel and generate spontaneous movements and mechanical stresses in the system, even in the absence of external forces or torques. Moreover these active stresses effectively fluidify the material. The cell cytoskeleton, suspensions of swimming microorganisms or tissues are prominent examples of active fluids.

Active processes in biological systems often exhibit chiral asymmetries. Examples are the chirality of cytoskeletal filaments which interact with motor proteins, the chirality of the beat of cilia and flagella as well as the helical trajectories of many biological microswimmers. Moreover, large scale chiral flows have been observed in the cell cortex of *C. elegans* and *Xenopus* embryos.

Active force generation induces force and torque dipoles in the material. If all forces are internal the total force and torque vanish as required by the conservation of momentum and angular momentum. The density of force dipoles is an active stress in the material. In addition, active chiral processes allow for the existence of active torque dipoles which enter the conservation of angular momentum and generate an active antisymmetric stress and active angular momentum fluxes.

We developed a generic description of active fluids that takes into account active chiral processes and explicitly keeps track of spin and orbital angular momentum densities. We derived constitutive equations for an active chiral fluid based on identifying the entropy production rate from the rate of change of the free energy and linearly expanding thermodynamic fluxes in terms of thermodynamic forces.

We identified four elementary chiral motors that correspond to localized distributions of chiral force and torque dipoles that differ by their symmetry and produce different chiral fluid flows and intrinsic rotation fields.

We employ our theory to analyze different active chiral processes. We first show that chiral flows can occur spontaneously in an active fluid even in the absence of chiral processes. For this we investigate the Taylor-Couette motor, that is an active fluid confined between two concentric cylinders. For sufficiently high active stresses the fluid generates spontaneous rotations of the two cylinders with respect to each other thus breaking the chiral symmetry of the system spontaneously.

We then investigate cases where active chiral processes on the molecular scale break the chiral symmetry of the whole system. We show that chiral flows occur in films of

chiral motors and derive a generic theory for thin films of active fluids. We discuss our results in the context of carpets of beating cilia or *E. coli* swimming close to a surface.

Finally, we discuss chiral flows that are observed in the cellular cortex of the nematode *C. elegans* at the one cell stage. Two distinct chiral flow events are observed. The first chiral flow event (i) is a screw like chiral rotation of the two cell halves with respect to each other and occurs around 15min after fertilization. This event coincides with the establishment of cortical cell polarity. The second chiral flow event (ii) is a chiral rotation of the entire cell cortex around the anterior posterior axis of the whole cell and occurs around 30min after fertilization. Measuring densities of molecular motors during episode (i) we fit the flow patterns observed using only two fit parameters: the hydrodynamic length and cortical chirality. The flows during (ii) can be understood assuming an increase of the hydrodynamic length. We hypothesize that the cell actively regulates the cortical viscosity and the friction of the cortex with the eggshell and cytosol.

We show that active chiral processes in soft biological matter give rise to interesting new physics and are essential to understand the material properties of many biological systems, such as the cell cortex.

Contents

Chapter 1

Introduction

The body plan of most animals and many plants breaks left-right symmetry in a way that is conserved between individuals of the same species. A prominent example is our own human anatomy, with the heart on the left of the body mid-plane in all but one in ten-thousand individuals [1–5].

The physiological functions of this chirality are diverse. Consistent chirality within one organism helps facing the packing problem of fitting organs into a confined space. Consistent chirality between different individuals of the same species can be important when they interact [2]. One example is the mating of snails that is physically awkward between individuals of different chirality, i.e. with their houses on different sides [6]. Even a conserved chirality between organisms of different species can be advantageous. For instance the jaws of some snail eating snakes are chiral. Their chirality is adapted to the chirality of their preys shells [7].

Unlike the establishment of the anterior-posterior axis $\mathbf{a}$ and the dorsal-ventral axis $\mathbf{b}$, which can occur independently, breakage of left-right symmetry requires taking into account the two preexisting axes. A mechanism is required to perform a right handed crossproduct, such that the left-right vector $\mathbf{l} = \mathbf{a} \times \mathbf{b}$ reliably distinguishes left from right [1–3]. Since a priori the laws of physics do not distinguish between left and right a preexisting cue is required to consistently define the cross product operator $\times$.

First signatures of chiral symmetry breaking are observed in individual cells. For instance the cell cortex of the one-cell stage *Xenopus* embryo displays chiral cortical flows [8, 9] and neurites crawl on chiral paths in in vitro experiments [10]. Therefore it has been hypothesized that individual cells have access to a molecular symmetry-cue in the form of a structurally chiral F-molecule [1]. The collective behavior of these F-molecules and molecular motors could give rise to flows that break left-right symmetry on cellular and multi cellular scales.

In fact, most biomolecules are chiral [5]. In vitro experiments provide examples which show that the chirality of biomolecules can be used to generate chiral motion [11, 12]. Similar mechanisms are exploited by biological structures in living organisms and are at the basis of the chiral beat of cilia [5, 13–16] and chiral flows in the cytoskeleton [8, 9]. Many pattern forming events in biological systems are governed by active chiral pro-

9

cesses. For example, it has been shown that the rotating beat of cilia, which drives chiral hydrodynamic flows, is at the basis of left-right symmetry breaking in vertebrate animals [17–19]. The interactions of motors and filaments drive movements and intracellular flows [20, 21] which can have chiral asymmetries [8, 11, 12, 16].

In the framework of this thesis, we develop a generic theory for fluids in which active chiral stresses and angular momentum fluxes are generated by the presence of molecular scale torque and force dipoles. We identify four elementary chiral motors that correspond to localized distributions of chiral force and torque dipoles that differ by their symmetry and produce different chiral fluid flows and intrinsic rotation fields. Our derivation is an extension of earlier work on liquid crystals [23–29] and active fluids [30–35].

We discuss our theory in the context of chiral micro-swimmers close to a surface and the cytoskeleton. To distinguish chiral flows generated by the intrinsic chirality of these structures from flows that spontaneously break chiral symmetry, we also provide an example for such a spontaneous chiral symmetry breaking in a Taylor-Couette geometry [36].

We start by introducing the cytoskeleton, as one paradigmatic example for an active chiral fluid [37]. Specifically we introduce one cytoskeletal structure, the cell cortex, which is a thin layer of helical actin filaments and molecular motors that resides under the cell membrane of eukaryotic cells, focusing on the cell cortex of *C. elegans* , which shows chiral motion. We also mention other examples of biological fluids that are active and chiral: (i) a fluid driven by beating chiral cilia; (ii) a suspension of flagellated bacteria, such as *E. coli*. We then give an overview of the concepts of non-equilibrium thermodynamics, which will provide the starting points for our derivation of a theory of active chiral fluids in chapter 2. Finally we outline the structure of the present work.

1.1   The cytoskeleton

Cells actively control and modify their own mechanical properties. The structure that enables them to do so is the cytoskeleton [5, 14, 38]. The cytoskeleton is instrumental in determining cell shape [39]. It is essential for cell locomotion and cell division [38, 40]. It is involved in the separation of chromosomes, the placement and formation of the cleavage furrow, and many other vital cellular processes. Its role is to provide the cell with a highly dynamic scaffolding that allows it to function as a mechanical entity that can rapidly adapt to achieve different tasks [1, 5, 14].

1.1.1   Main constituents of the cytoskeleton

The cytoskeleton is made up of filamentous polymers, molecular motors that exert forces between the filaments, crosslinking proteins that tie the filaments into a meshwork and a manifold of associated proteins that coordinate the actions of the various players in space and time. We now introduce its most important components.

Filamentous proteins

Filamentous proteins provide the backbone of the cytoskeleton. Three families of cytoskeletal filamentous proteins - actins, tubulins and intermediate filaments - exist [5].
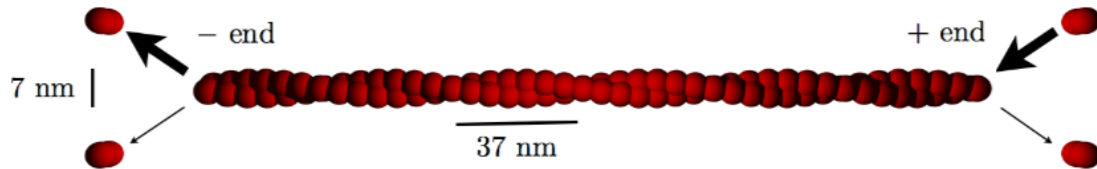
Figure 1.1: Sketch of an actin filament. The arrows indicate chemical reaction rates.

Monomeric **actin**, or G-actin is a globular protein that is ubiquitous in the cell and has an ATP binding site [41, 42]. It polymerizes into helical F-actin filaments, see Fig. 1.1. The actin filament is made up of two proto-filaments, that wind around each other. The pitch of the helix is approximately 37 nm, the diameter of the filament is around 7 nm. The persistence length of filamentous actin is around 17 microns [43, 44]. Actin filaments are structurally polar, in the sense that new monomers preferentially bind to the plus end of the filament and unbind from the minus end. Actin filaments undergo tread-milling [45], that is regulated by the consumption of ATP. Actin plays prominent roles in the changing and maintaining cell shape, in cell motility [46] and cell division [47].
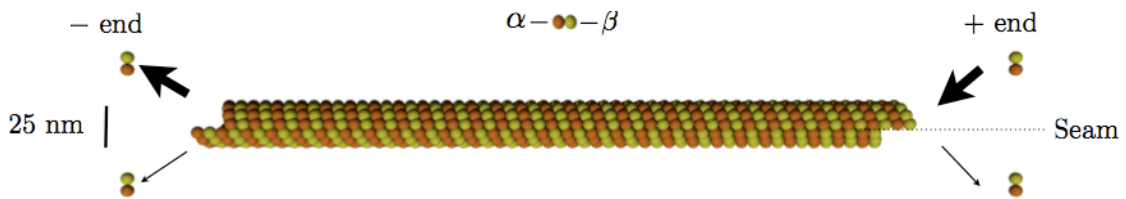
Figure 1.2: Sketch of a (N-S) 13-3 microtubule. The arrows indicate chemical reaction rates.

The second important filament forming proteins are **tubulins** [5, 48]. The two proteins, α- and β-tubulin associate to form a structurally polar $\alpha - \beta$ dimer, that is about $4nm$ long [49]. The dimers bind end to end. The resulting alternating α- and β-tubulin monomers, are called microfilaments. Microfilaments are structurally polar. N parallel protofilaments bind to form a tubular lattice [48]. Laterally the binding occurs preferentially between monomers of the same type. The lateral binding is slightly offset along the axis of the protofilament. Thus the arangement of monomers on the microtubule forms a helix with helix start number S, measured in monomer lengths. Lattices with $8 \leq N \leq 17$ and $2 \leq S \leq 4$ exist and are collectively referred to as microtubules, see Fig. 1.2. Microtubules with $S = 3$ have an additional distinguishing feature, the seam. The seam is the pair of adjacent micro-filaments that unlike the others laterally binds such that monomers of the same type are adjacent. The most common microtubule is the (N-
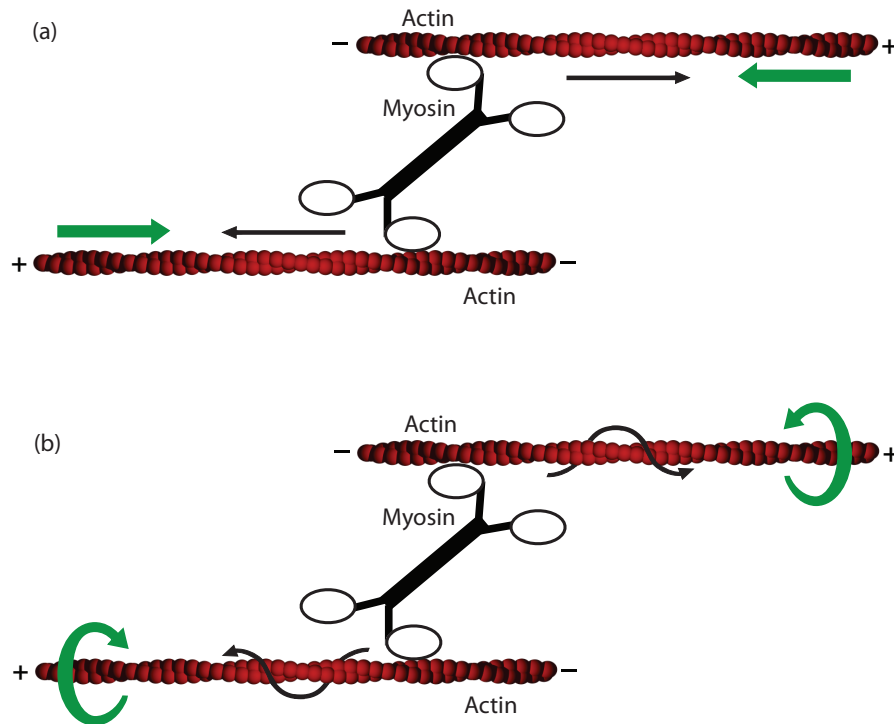
Figure 1.3: Schematic of a molecular scale force dipole (a), and a molecular scale torque dipole (b). Molecular motors (myosin, black and white) walk of filaments (actin, red). Black arrows denote the direction of motion of the motor-heads. In (a) green straight arrows denote forces. In (b) green curved arrows denote torques exerted on the fluid.

S) 13-3 type sketched in figure 1.2. Its radius is about 25nm. The persistence length of microtubule is around 1.4 ± 0.3 mm, which is much larger than the typical cell sizes and makes it stiffest of the cytoskeletal filaments [44]. One important role of microtubules is to act as pathways for intracellular transport [5]. They are also involved in many other processes such as the centering of the mitotic spindle [50–52]. Most importantly microtubules are structurally chiral [48].

An other structure formed by proteins of the tubulin family are microtubule doublets. In microtubule doublets a complete A-microtubule of 13 proto-filaments binds to an incomplete B-microtubule consisting of ten protofilaments [15]. These structures are essential in building the axoneme that resides at the core of beating cilia and flagella.

Besides microtubule and actin filaments, many cell types also produce other filament forming proteins. Many different such **intermediate filaments** filaments exist. Their function is often associated to providing mechanical stability [5].

Motor proteins

While filamentous proteins provide a strong yet flexible and dynamical scaffolding, motor proteins generate forces by coupling ATP hydrolysis to conformational changes [1,5,14]. Molecular motors are categorized in three super-families, that are distinguished by the type of filaments which they bind to. **Myosins** are actin associated motors, while **kinesins** and **dyneins** operate on microtubules [5,38].

The tasks of molecular motors are diverse [53]. Some are involved in cargo transport [54], others role it is to serve as force generators, and enable contraction of large structures such as myofibrils found in muscle-cells [5,38].

Motor proteins exert forces on cytoskeletal filaments. Since all forces are internal to the system, they are balanced by equal but opposite counter-forces in the way required by Newtons second laws. Thus molecular motors can not generate unbalanced forces but only force dipoles. As an example consider a myosin mini-filament acting between two anti-parallel actin filaments, see Fig. 1.3 (a). Myosins are directed motors that walk towards the plus end of the filaments. In this way they exert a pulling force on the filaments. The pulling force exerted on the first filament is equal and opposite to the pulling force exerted on the second filament. Densities of such force dipoles correspond to active stresses in the system [30,31]. Not only do motor proteins exert forces on cytoskeletal filaments, they also can exert torques. It has been shown that myosin motors attached to a glass cover slip induce rotations on actin filaments in a sliding essay [11]. The sense of rotation has been linked to the helicity of the actin filament itself [12]. Like the forces that act in the cytoskeleton, all torques are internal to the system and thus have to be balanced by equal but opposite counter-torques. As a consequence no torque monopoles are possible. However torque dipoles exist. One example for a possible torque dipole is shown in Fig. 1.3 (b). A myosin mini-filament is attached to two antiparallel actin filaments. While the motor walks towards the plus ends of both filaments it also infers a rotation to the filaments. In this way it generates a torque dipole in the fluid. In chapter 4 we will show that densities of torque dipoles and chiral force dipoles correspond to active angular momentum fluxes and antisymmetric stresses in the system, respectively.

Associated proteins

The majority of known cytoskeletal proteins are not filamentous proteins or motors. They are to numerous and diverse to discuss in detail here. Here we just review some of the most important functions these proteins can fulfill and refer to [5,41] for a more complete overview.

Nucleators help to provide a nucleation point for forming filaments. **Capping proteins** bind to the ends of filaments. Their role can be to stabilize the filaments growth. **Severing proteins** cut filaments. **Sequestering molecules** help with the recycling of monomers of filamentous proteins. **Sidebinding proteins** serve as molecular rulers for measuring the lengths of filaments. **Crosslinking** and **bundling** proteins, connect filaments with each other, organizing them into a structured network. **Linkers** link fil-
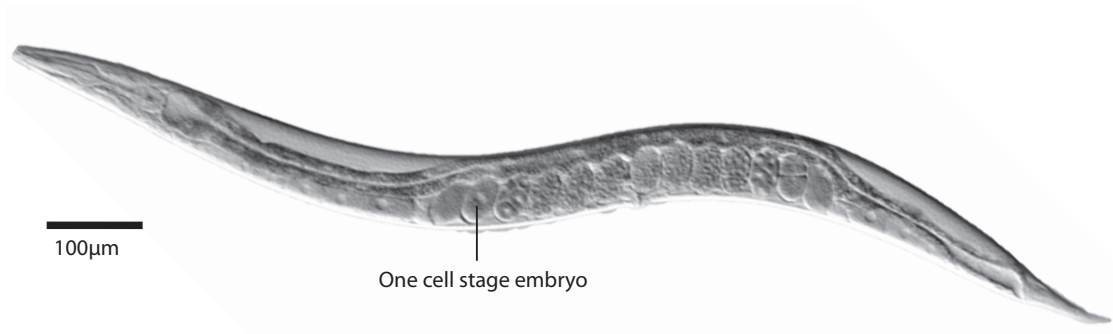
Figure 1.4: Microscope picture of *Caenorhabditis elegans*, by M. Leaver (used with permission). We marked the one cell stage embryo that is visible inside the gonad of the worm.

aments of different kinds. **Regulators** inhibit or facilitate the action of other proteins. Note that individual proteins can belong to several of these categories.

1.1.2   Chiral motion of cytoskeletal structures

Cytoskeletal filaments are organized into complex networks by associated proteins, and set under active stress by molecular motors [55]. Under sufficiently high active stresses the inert state of such cytoskeletal networks becomes unstable and spontaneous motion is generated [16, 36, 56]. Examples cytoskeletal structures that display large scale motion under the effect of molecular motors are, amongst many others, the *C. elegans* cell cortex and beating cilia. We will introduce these structures now.

The cell cortex of the *C. elegans* embryo

The nematode (roundworm) *Caenorhabditis elegans* represented in Fig. 1.4, is a popular model organism since its introduction in 1974 by Sidney Brenner [57–59]. The adult *C. elegans* is about $1mm$ long and transparent. Two sexes, one male and one hermaphrodite exist. The ratio of males to hermaphrodites is around one in two-hundred, if the growth conditions are favorable. The generation time of *C. elegans* is around four days. It is transparent and its development is highly stereotyped. Specifically the cell fate of all somatic cells is conserved between individuals and has been mapped out for all 959 and 1029 somatic cells of the adult male and hermaphrodite, respectively. The genome of *C. elegans* has been sequenced [59]. An important tool that researchers in *C. elegans* have at their disposal is RNA interference, which has been developed in *C. elegans* and was awarded the Nobel price in 2006 [60]. By this method it is possible to suppress the expression of targeted proteins and thus essay for their role in the cell in loss of function experiments [61].

The one cell stage *C. elegans* embryo, see Fig. 1.4, can be extracted from the worm and imaged. It is a single cell enveloped by a rigid eggshell, see 1.5 (a). The cell cortex
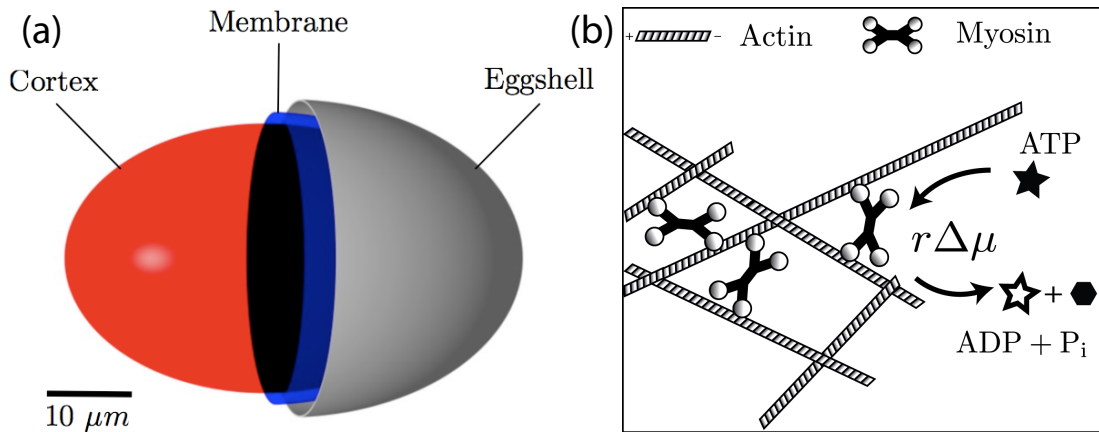
Figure 1.5: Sketch of the *C. elegans* one cell stage embryo (a). The cell cortex main constituent are myosin motors and actin filaments that form an entangled network (b). The myosin motors set the network under stress hydrolyzing adenosinetriphosphate (ATP) to adenosinediphosphate (ADP) on inorganic phosphate (P_i).

is a thin layer of cross-linked filamentous actin, and myosin motor proteins directly beneath the cell membrane. The motor proteins in the cortex exert force and torque dipoles between the actin filaments, see Fig. 1.3 and Fig. 1.5 (b). Densities of force dipoles and torque are active stresses and angular momentum fluxes, and provide the cell cortex with a tendency to actively contract [55]. This contractility of the cortex has been measured and quantified using laser ablation experiments [21]. The cell cortex is a dynamic structure that undergoes constant turnover. Cytoskeletal filaments assemble and disassemble, molecular motors and cross-linkers bind and unbind. In *C. elegans* was estimated to be on the order of 30 seconds experimentally [21]. One consequence of this permanent turnover is that elastic stresses in the cortical meshwork relax on time scales comparable to the turnover time. On longer time scales the cortex can thus be considered a viscous fluid.

The cell cortex is involved in many important cellular functions, such as shape change, cell division [1, 5, 14, 21, 40, 62]. The cortex of the one cell stage *C. elegans* embryo is particularly interesting to study, since it divides asymmetrically [63, 64]. During asymmetric cell division a single mother cell divides into two daughter cells of different cell fate [1, 5, 65]. This process allows an organism to develop from a single embryonic stem cell into a complex structured organism in which different cells assume different roles. In *C. elegans* the fertilized zygote P_0 divides in a bigger *AB*-cell, that will give rise to somatic cells only, and the smaller P_1 cell. The P_1, remains stem cell like. It later undergoes four more rounds of asymmetric division, and finally gives rise to the germ line cell P_4 [59, 63].

Asymmetric cell division requires breaking the symmetry between the two daughter cells. In the *C. elegans* zygote the symmetry is initially broken by the entry point of the sperm. This event starts a cascade of protein reactions which provide a trigger
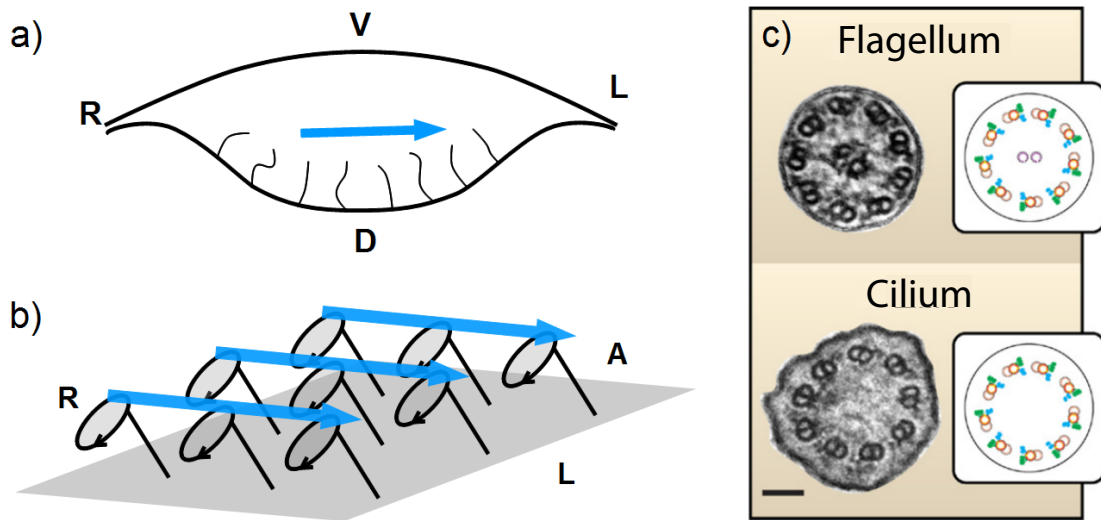
Figure 1.6: (a) Schematical representation of the *ventral node* of the mouse (adapted from Fig. 10 in [22]) and (b) a carpet of rotating cilia where black arrows indicate the sense of rotation. V, D, A, P, R, L denote the ventral, dorsal, anterior, posterior, right and left side of the organism, respectively. Cilia tilted towards the posterior drive a leftward fluid flow (blue arrows). (c) Cross-section of a flagellum and cilium, and their axoneme. Adapted from N. Hirokawa et al., Cell **125**, 33-45 (2006).

to start pattern forming process in the cell cortex, leading to an anterior (A) half of the cell which is biochemically different from its the posterior (P) [66]. Specifically, this cascade of events involves regulation of the activity of motor proteins, generating spacial gradients of active stress. Spacial imbalances in active stress give rise to long ranged flows [21] wich help translating the initial symmetry breaking cue into a pattern of proteins on the cell cortex [66] by a reaction diffusion advection process [62]. These cortical flows are chiral. Thus the *C. elegans* cell cortex is an active chiral fluid. We will discuss these chiral cortical flows in detail in chapter 6.

Flows driven by cilia

A second example for active chiral cytoskeletal structures are cilia and flagella. Cilia and flagella are whip like appendages of cells, that can actively generate motion thanks to a structure at their chore, the axoneme. The axoneme consists of nine microtubule doublets, that are arranged on a circle in a chiral fashion, see Fig.1.6 (c). Dynein motors exert forces between the microtubule doublets and generate motion [5, 14, 16]. Many different beating patterns of cilia exist, which in general are chiral and often exhibit rotating movements, as is the case for the cilia that govern the left-right symmetry breaking of organisms [19, 67].

Tissues with motile cilia are ubiquitous in biology. For instance they are found in the vertebrate lungs [68, 69], brains [70] and kidneys, where there role is to pump fluid.
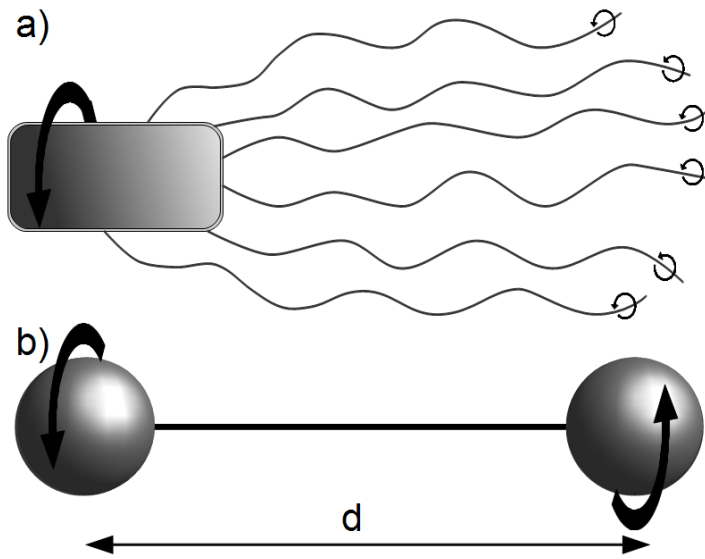
Figure 1.7: (a) Schematic representation of a swimming bacterium with rotating flagella. (b) Chiral motor consisting of two counter-rotating spheres at distance d. Arrows indicate senses of rotation.

Ciliated tissue also have an important role during the development of organisms [1–3]. For instance, in developing mice carpets of chiraly beating cilia are involved in the left-right symmetry breaking of the whole organism [17–19, 71, 72]. The embryo, which already has broken anterior-posterior and dorsal-ventral symmetry at this point, forms a flat cavity called the ventral node, see Fig. 1.6 (a). The ventral side of the node is covered with chiraly beating cilia, that are tilted towards the posterior. This arrangement generates a leftward fluid flow, see Fig. 1.6 (b), that triggers the left right symmetry breaking of the entire organism. Such carpets of chiral motors can be described as active chiral fluids, and will be discussed in chapter 5.

1.2 Other examples of active fluids

Many biological micro-swimmers are chiral. One example is the bacterium *E. coli* that derives its motility from chirally rotating flagella [14], see Fig. 1.7 (a). It is thus structurally similar to two counter-rotating spheres, i.e. a nematic chiral motor, see Fig.1.7 (b). One consequence of this is that it swims on curved trajectories, when close to a surface [14, 73]. Other microorganisms, such as *Paramecium* or *Volvox* possess carpets of cilia on their outer surface, which are used for self-propulsion along helical trajectories in a fluid [14].

Suspensions of such chiral swimmers can thus be considered an active chiral fluid. Recently, the collective behavior of swimming *E. coli* bacteria on solid surfaces was studied [74]. The *E. coli* were placed on a solid agar surface [74], where they produced a

thin fluid layer that promotes their motility. Some bacteria attach to the surface while others swim in the film. The bacteria which were attached to the surface also exerted torques on the solid substrate. Large scale chiral flow patterns were reported as a result of bacterial activity [74]. The bacterial suspension therefore represents an internally driven active chiral film supported by a surface. We will discuss this in more detail in chapter 5.

One further example of a rotating biological motors is F1-F0-ATP-Synthases. This structure, consisting of two subunits that are in contact across a membrane is involved in the production of ATP. It has however also be observed to hydrolyze ATP work as a motor [75]. A membrane with many such motors can thus be considered a two-dimensional active chiral fluid. The hydrodynamic interaction between the motors has been shown to lead to the formation of non-equilibrium patterns [76].

Outside the realm of biology collections of chiral particles on a vibrating surface have attracted some interest [77]. These systems are especially interesting for their conceptual simplicity.

1.3 Hydrodynamic theories of active fluids

In the previous section we introduced several examples of active chiral fluids. While the microscopic mechanisms at work in these systems are very different from each other, in the hydrodynamic limit, i.e. on large length and long time-scales the generic properties of active fluids are described by generic equations. Hydrodynamic modes are the result of conservation laws and of broken continuous symmetries [26, 27, 78]. Hydrodynamic equations can be obtained systematically by first identifying conjugate pairs of thermodynamic fluxes and forces. Constitutive material relations can be expressed by writing all linear coupling terms permitted by symmetry, respecting the Onsager reciprocity relations [26, 32, 33]. Note that similar approaches have also been used to describe bird flocks [79–81], swarms of hydrodynamically interacting swimmers [30, 31], active nematic fluids [82–85], or active solids [86–88]. In all these approaches, the complexities of the microscopic interactions are captured in a small number of phenomenological coefficients, that can be measured, or determined from microscopic models. Several approaches that model active fluids as suspensions of rods crosslinked by motor molecules have been proposed [82, 83, 89–91]. We now briefly outline the important concepts that underlie our approach to hydrodynamic theories for active fluids. We first discuss the concept of coarse grained theories and how to form the continuum limit, then we introduce the assumption of local equilibrium, the Onsager reciprocity theorem and Curies dissymmetry principle. Finally we discuss the constitutive equations that have been obtained for achiral viscous active gels in [32–34].

1.3.1 Coarse graining

Consider a fluid consisting of a large number N of particles at with masses $m^{(i)}$ and positions $\mathbf{x}^{(i)}$, and velocities $\mathbf{v}^{(i)}$. Describing the dynamics of such a fluid on the microscopic

scale requires to keep track of $6N$-degrees of freedom, which is of coarse impracticable. Instead we coarse grain our description of the fluid by dividing it into small volumina V, and defining coarse grained variables. For instance the mass density ρ in a volume V of fluid is given by,

$$\rho = \frac{M}{V} = \frac{1}{V} \sum_{\mathbf{x}^{(i)} \in V} m^{(i)} \quad , \tag{1.1}$$

where the total mass of the volume element in

$$M = \sum_{\mathbf{x}^{(i)} \in V} m^{(i)} \quad . \tag{1.2}$$

We can then define a center of mass velocity of the volume element

$$\mathbf{v} = \frac{1}{M} \sum_{\mathbf{x}^{(i)} \in V} m^{(i)} \mathbf{v}^{(i)} \quad . \tag{1.3}$$

and a momentum density

$$\mathbf{g} = \rho \mathbf{v} \quad . \tag{1.4}$$

The flux of momentum into the volume V is given by the stress tensor $\sigma_{\alpha\beta}^{tot}$, which obeys,

$$\int_{\partial V} \sigma_{\alpha\beta}^{tot} dS_\beta = \partial_t \int_V dx^3 \mathbf{g} \quad . \tag{1.5}$$

Here, the boundary of the considered volume V of fluid is written as ∂V. The stress tensor has the dimension of a force per area, and describes the force that acts along a virtual cutline through the material. The first index of the tensor denotes the direction along which the virtual force acts, while the second index refers to the direction of the virtual cutline. Equation (1.5) is nothing but the force balance equation of the volume element V.

1.3.2 The continuum limit

In the way we introduced the coarse grained variables in equations 1.1, 1.3 and 1.4 they are strictly speaking functions of the coarse graining volume V. To obtain a continuous theory we go to the limit where the coarse graining volumina are small and $V \to 0$. In the continuum limit the coarse grained variables can be written as continuous functions of space. Such that for instance,

$$\rho = \rho(\mathbf{r}) \quad . \tag{1.6}$$

where $\mathbf{r}$ is a position vector.

It is the aim of any hydrodynamic theory to derive dynamic equations for $\rho(\mathbf{r})$, $\mathbf{v}(\mathbf{r})$ and the other continuous coarse grained variables that exist in complex fluids, such as local order parameters or continuous broken symmetries.

1.3.3   Slow variables and local equilibrium

In order to apply thermodynamic principles to derive a hydrodynamic theory for active fluids, we make one essential assumption, which is the assumption of local equilibrium. Explicitly, we assume that each volume element V of the fluid is in thermodynamic equilibrium, but out of equilibrium with neighboring volume elements. Most of the $6N$-degrees of freedom relax towards a thermal distribution that is set by only a few slow variables on time scales that are fast compared to the time evolution of the slow variables. In general the slow variables are given by conserved quantities, continuous broken symmetries, and order parameters close to a phase transition.

Under the assumption of local equilibrium it is possible to locally define a free energy density f, that depends only on the slow variables. The free energy of a volume V of fluid is then defined as

$$F = \int_V f dx^3 \quad . \tag{1.7}$$

It is thus also possible to define an entropy of the volume V using that

$$S = \frac{1}{T}(U - F) \quad , \tag{1.8}$$

where U is the internal energy and T is the temperature. If the system is globally out of equilibrium entropy will be produced until the global equilibrium state, the state of highest entropy, is reached. The entropy production rate $\dot{\Theta}$ can be derived from 1.8, systematically as we shall show 2. In fact the entropy production rate can be used to systematically derive constitutive material equations for the fluid using the Onsager reciprocity theorem and Curie's dissymmetry principle.

1.3.4   Onsager reciprocity theorem

The entropy S is maximal at equilibrium. The entropy production rate for a system out of equilibrium is always positive,

$$\dot{\Theta} \geq 0 \quad . \tag{1.9}$$

In general, the entropy production rate can be expressed as a sum of products of thermodynamic fluxes $J^{(i)}$ and forces $X^{(i)}$ such that

$$\dot{\Theta} = \sum_i J^{(i)} X^{(i)} \quad , \tag{1.10}$$

where $J^{(i)}$ and $X^{(i)}$ vanish at equilibrium. Close to equilibrium the thermodynamic fluxes $J^{(i)}$ can be expressed as linear functions of the thermodynamic forces $X^{(i)}$, i.e.

$$J^{(i)} = \alpha_{ij} X^{(j)} \quad , \tag{1.11}$$

and thus

$$\dot{\Theta} = \alpha_{ij} X^{(i)} X^{(j)} \quad . \tag{1.12}$$

The equations (1.11) are the constitutive equations of the material and α_{ij} are phenomenological coefficients that capture the fluids material properties.

The second law of thermodynamics (1.9) imposes conditions on the coefficients of the matrix α_{ij}, that are known as the Onsager reciprocity principles. It has to be ensured that the entropy production rate stays positive if the directions of all microscopic velocities are reversed, an operation commonly termed time-reversal. Thus it can be shown that $\alpha_{ij} = \alpha_{ji}$ if $X^{(i)}$ and $X^{(j)}$ have the same behavior under time reversal, and that $\alpha_{ij} = -\alpha_{ji}$ if $X^{(i)}$ and $X^{(j)}$ have different behavior under time reversal [26].

Note that the Onsager reciprocity theorem only holds close to equilibrium, further away non-linear terms start to play a role.

1.3.5   The Curie dissymmetry principle

The possible phenomenological coefficients α_{ij} are further constrained by the symmetries of the system. The Curie dissymmetry principle states that a physical effect can not have a dissymmetry absent from its physical cause [26]. Thus in an isotropic fluid only isotropic couplings between thermodynamic fluxes and forces are possible. In a system with polar symmetry, polar couplings are also possible. In the chiral fluids, we investigate here the couplings between thermodynamic fluxes and forces can also lack inversion symmetry, and the constitutive equation need not be invariant towards the transformation $\mathbf{r} \rightarrow -\mathbf{r}$, where $\mathbf{r}$ is a position vector. As we will show this broken symmetry allows for interesting new physics, and new active terms in the constitutive equations.

1.3.6   Constitutive equations of active polar gels

Following the principles outlined in this section, constitutive equations for active gels have been derived in [32–35]. For an incompressible single component active viscous gel the thermodynamic fluxes have been identified. They are: (i) the symmetric part of the deviatoric stress,

$$\sigma_{\alpha\beta} = \sigma_{\alpha\beta}^{tot} - \sigma_{\alpha\beta}^{tot,a} - \rho v_\alpha v_\beta \quad + P\delta_{\alpha\beta}, \tag{1.13}$$

where $\sigma_{\alpha\beta}^{tot,a}$ is the antisymmetric part of the total stress tensor and $P = -\sigma_{\gamma\gamma}^{tot}$ is the pressure ; (ii): the co-rotational derivative of the polarity vector

$$\frac{Dp_\alpha}{Dt} = \partial_t p_\alpha + v_\gamma \partial_\gamma p_\alpha + \frac{1}{2} \left(\partial_\alpha v_\beta - \partial_\beta v_\alpha \right) p_\beta \quad , \tag{1.14}$$

and (iii): the rate r of hydrolysis of a chemical fuel. The thermodynamic force are given by (a): the symmetric strain rate tensor

$$u_{\alpha\beta} = \frac{1}{2} \left(\partial_\alpha v_\beta + \partial_\beta v_\alpha \right) \quad , \tag{1.15}$$

which describes local strain deformations in the fluid; (b): the polar distortion field

$$h_\alpha = -\frac{\delta F}{\delta p_\alpha} \quad , \tag{1.16}$$

which is the conjugated field to the polarity field **p**, that drives it towards its equilibrium configuration; and (c): the difference in chemical potential between a fuel molecule and its reaction products $\Delta\mu$. Material constitutive equations have been obtained by linearly expanding thermodynamic fluxes in terms of thermodynamic force,

$$\sigma_{\alpha\beta} = 2\eta u_{\alpha\beta} + \frac{\nu_1}{2}\left(p_\alpha h_\beta + p_\beta h_\alpha\right) + \zeta p_\alpha p_\beta \Delta\mu + \zeta' p_\gamma p_\gamma \delta_{\alpha\beta}\Delta\mu \quad, \quad (1.17)$$

$$\frac{Dp_\alpha}{Dt} = \frac{1}{\gamma}h_\alpha + \lambda_1 p_\alpha \Delta\mu - \nu_1 p_\beta u_{\alpha\beta} \quad, \quad (1.18)$$

$$r = \Lambda\Delta\mu + \lambda_1 p_\alpha h_\alpha + \zeta p_\alpha p_\beta u_{\alpha\beta} + \zeta' p_\alpha p_\alpha u_{\beta\beta} \quad. \quad (1.19)$$

Similar equations can be obtained by alternative methods such as the Poisson bracket approach [28, 29]. Here η, ν_1, γ, ζ, ζ', λ_1 and Λ are the phenomenological coefficients, that correspond to the α_{ij} in Eq. (1.11). Their values are specific to the fluid considered and can be measured in experiment or determined from microscopic models.

1.4   Overview of this work

The aim of this thesis is to develop a theory for active chiral fluids and discuss its implication to biological systems. Specifically we show that active chiral fluids can spontaneously generate fluid flows that break chiral symmetry. In contrast to spontaneous symmetry breaking that can exist in inversion symmetric active fluids, the chirality of flows in active chiral flow is set by the chirality of their constituents. The structure of this thesis is as follows. In chapter 2 we derive a generic theory of active chiral fluids based on symmetry considerations and conservation laws only and obtain the most general set of equations that describe an active chiral fluid. We discuss how the Navier Stokes eauation and preexisting hydrodynamic theories for inversion-symmetric active fluids can be obtained from our theory. We then move on to discuss different examples of active processes within the theoretical frameworks obtained in 2. In chapter 3 we discuss spontaneous flows generated in an inversion-symmetric fluid confined between two cylinders. These flows break chiral symmetry spontaneously, making the two cylinders rotate with respect to each other. This system, which we call the Taylor-Couette motor provides an example of an active chiral process, that does not require microscopic chirality. In chapter 4, we show how distributions of chiral torque and force dipoles in a fluid can give rise to the active chiral terms that we identified in chapter 2. We calculate the flow and rotation field, around localized distributions of such dipoles, that differ by their symmetry, which we call elementary motors. In chapter 5 we discuss films of chiral fluids. We show that an active chiral fluid confined between two surfaces generates spontaneous large scale flows by an active chiral boundary layer effect. Motivated by this observation we develop a generic theory for thin films of chiral active fluid. The coupling of the chiral bulk equations to the surface via frictional terms, generates new interesting effects that we discuss in the context of chiral swimmers adhering to a surface and carpets of beating cilia. Finally, in chapter 6 we discuss flows in the cell cortex of the one-cell stage embryo of the nematode worm *C. elegans* . We show that these flows

are chiral, and apply our theory to extract material properties of the cell cortex from experimental movies. Finally in chapter 7 we give a summary of our results and indicate possible directions for future research.

Chapter 2

Generic theory of active chiral fluids

In this chapter we derive the hydrodynamic theory for active chiral fluids, based on conservation laws and symmetry arguments alone. For simplicity, we consider an isothermal system at a fixed temperature T. Our derivation closely follows the logic outlined in Refs [25–27,32,33]. However unlike these references, we explicitly consider a spin angular momentum degree of freedom, which will reveal to be crucial in order to describe active chiral systems. The role of spin angular momentum was discussed in the frameworks of passive fluids in Ref [29]. Here we extend these ideas to active systems.

2.1 Conserved quantities

Mass, momentum and angular momentum, as well as energy are conserved quantities. This, of coarse remains valid in fluids. Here, we consider a fluid consisting of a large number N of particles at with masses $m^{(i)}$ and positions $\mathbf{x}^{(i)}$, and particle velocities $\mathbf{v}^{(i)}$. We explicitly state the conservation laws in small volume elements V of fluid, and show how they lead to continuity equations for densities of conserved the quantities.

2.1.1 Mass conservation

The mass of a volume V of fluid is given by

$$M = \sum_{\mathbf{x}^{(i)} \in V} m^{(i)} \quad , \tag{2.1}$$

and is a conserved quantity. Thus it can only change a mass flux across the boundary of the volume V. We introduce the mass density

$$\rho = \frac{M}{V} \quad , \tag{2.2}$$

and the center of mass velocity

$$\mathbf{v} = \frac{1}{M} \sum_{\mathbf{x}^{(i)} \in V} m^{(i)} \mathbf{v}^{(i)} \quad . \tag{2.3}$$

In the continuum limit where $\rho = \rho(\mathbf{r})$ and $\mathbf{v} = \mathbf{v}(\mathbf{r})$. the conservation of mass can be expressed by the continuity equation

$$\partial_t \rho = -\partial_\alpha (\rho v_\alpha) \quad . \tag{2.4}$$

Here and below greek indices assume the values x, y, z, which correspond to the three spatial dimensions. We adopt Einsteins summation convention over repeated indices.

2.1.2   Particle number conservation

The fluid we consider consists of K different species of particles, with $k^{(i)}$ being the species of the i-th particle. The volume V of fluid thus contains

$$N_k = \sum_{\mathbf{x}^{(i)} \in V} \delta_{k^{(i)} k} \quad , \tag{2.5}$$

particles of species k, and we can define particle number densities $n_k = N_k/V$. The mass density can then be written as

$$\rho = \sum_k n_k m_k \quad . \tag{2.6}$$

In the continuum limit the particle number densities obey continuity equations

$$\partial_t n_k = -\partial_\alpha J_\alpha^k + R_k \quad . \tag{2.7}$$

The flux of particles of species k, $\mathbf{J}^k$ can be split into a convective part $n_k v_\alpha$ and a deviatoric particle mass flux $\mathbf{j^k}$,

$$J_\alpha^k = n_k v_\alpha + \frac{j_\alpha^k}{m_k} \quad . \tag{2.8}$$

By definition $\sum_i j_\alpha^k = 0$. The source terms R_i in Eq. (2.7) account for chemical reactions between the components of the fluid. Conservation of mass (2.4) requires that

$$\sum_k m_k R_k = 0 \quad , \tag{2.9}$$

which is Lavoisiers principle that no mass is created or lost in chemical reactions.

2.1.3 Momentum

The total momentum in the volume V is

$$\mathbf{G} = \sum_{\mathbf{x}^{(i)} \in V} m^{(i)} \mathbf{v}^{(i)} \quad , \qquad (2.10)$$

conserved in the absence of external forces. The momentum density is given by $\mathbf{g} = \rho \mathbf{v} = \mathbf{G}/V$. In the continuum limit it obeys the continuity equation

$$\partial_t g_\alpha = \partial_\beta \sigma^{tot}_{\alpha\beta} + f^{ext}_\alpha \quad . \qquad (2.11)$$

The total stress tensor $\sigma^{tot}_{\alpha\beta}$ contains all momentum density fluxes. The force density $\mathbf{f}^{ext}$ contains all external momentum density sources. The total stress tensor can be split

(a) Isotropic Stress   (b) Shear Stress   (c) Antisymmetric Stress
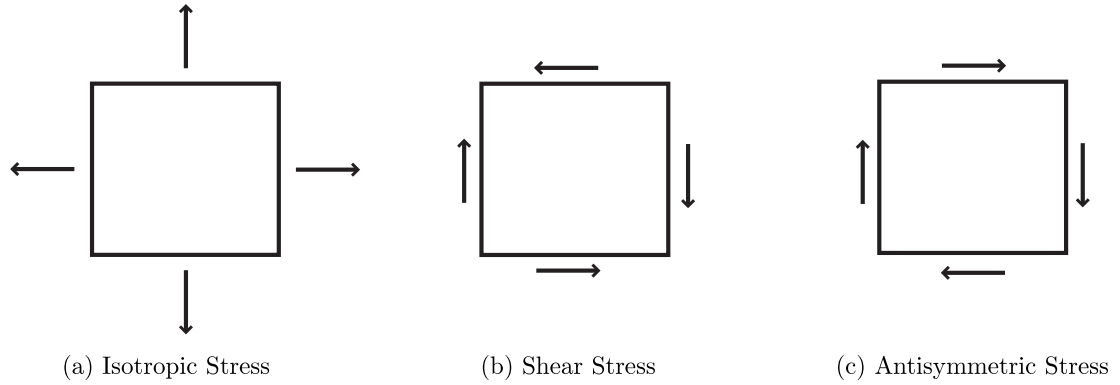
Figure 2.1: Sketch of the different components of the stress tensor. The arrows indicate the forces that a volume element (represented as a square) would exerts on its neighbors.

into three parts as displayed in Fig. 2.1, such that

$$\sigma^{tot}_{\alpha\beta} = \tilde{\sigma}^{tot}_{\alpha\beta} + \sigma^{tot,a}_{\alpha\beta} - P\delta_{\alpha\beta} \quad . \qquad (2.12)$$

Here $P = -\sigma^{tot}_{\gamma\gamma}$ is the pressure, see Fig. 2.1 (a) and $\tilde{\sigma}^{tot}_{\alpha\beta} = (\sigma^{tot}_{\alpha\beta} + \sigma^{tot}_{\beta\alpha})/2 + P\delta_{\alpha\beta}/3$ is the symmetric traceless shear stress , see Fig. 2.1 (b). Finally $\sigma^{tot,a}_{\alpha\beta} = (\sigma^{tot}_{\alpha\beta} - \sigma^{tot}_{\beta\alpha})/2$ is the antisymmetric part of the stress, see Fig. 2.1 (c). While the antisymmetric stress is zero in simple fluids, in complex fluids the antisymmetric stress can be finite. To understand its role it is instructive to consider angular momentum conservation.

2.1.4 Angular momentum

The total angular momentum of a volume V of fluid is given by,

$$L^{tot}_{\alpha\beta} = \sum_{\mathbf{x}^{(i)} \in V} m^{(i)} \left(x^{(i)}_\alpha v^{(i)}_\beta - x^{(i)}_\beta v^{(i)}_\alpha \right) \quad , \qquad (2.13)$$

and can be split into a orbital and a spin contribution,

$$L_{\alpha\beta}^{tot} = M\left(r_\alpha v_\beta - r_\beta v_\alpha\right) + L_{\alpha\beta} \quad, \tag{2.14}$$

where

$$\mathbf{r} = \frac{1}{M}\sum_{\mathbf{x}^{(i)} \in V} m^{(i)}\mathbf{x}^{(i)} \quad, \tag{2.15}$$

is the center of mass position of the volume element and

$$\begin{aligned} L_{\alpha\beta} &= L_{\alpha\beta}^{tot} - M\left(r_\alpha v_\beta - r_\beta v_\alpha\right) \\ &= \sum_{\mathbf{x}^{(i)} \in V} I_{\alpha\beta\gamma\mu}^{(i)}\Omega_{\gamma\mu}^{(i)} \quad, \end{aligned} \tag{2.16}$$

is its spin angular momentum. Here we have introduced the spin rotation rate $\Omega_{\alpha\beta}^{(i)}$ which fulfills,

$$\Omega_{\alpha\beta}^{(i)} = 2\left(\delta_{\alpha\gamma}\delta_{\beta\mu} - \delta_{\beta\gamma}\delta_{\alpha\mu}\right)\left(r_\gamma^{(i)} - r_\gamma\right)\left(v_\mu^{(i)} - v_\mu\right) \tag{2.17}$$

and the particle moment of inertia

$$I_{\alpha\beta\gamma\mu}^{(i)} = 2m^{(i)}(\mathbf{r}^{(i)} - \mathbf{r})^2\left(\delta_{\alpha\gamma}\delta_{\beta\mu} - \delta_{\beta\gamma}\delta_{\alpha\mu}\right) \quad. \tag{2.18}$$

We can now define a moment the inertia density of the volume element V as,

$$I_{\alpha\beta\gamma\delta} = \frac{1}{V}\sum_{\mathbf{x}^{(i)} \in V} I_{\alpha\beta\gamma\delta}^{(i)} \tag{2.19}$$

and its effective intrinsic rotation rate,

$$\Omega_{\alpha\beta} = I_{\alpha\beta\nu\delta}^{-1}\sum_{\mathbf{x}^{(i)} \in V} I_{\nu\delta\gamma\mu}^{(i)}\Omega_{\gamma\mu}^{(i)} \quad, \tag{2.20}$$

where

$$I_{\alpha\beta\nu\mu}^{-1}I_{\alpha'\beta'\nu'\mu'} = \delta_{\alpha\alpha'}\delta_{\beta\beta'}\delta_{\gamma\gamma'}\delta_{\mu\mu'} \quad. \tag{2.21}$$

Note that here we do not consider single particle spins. The spin angular momentum $L_{\alpha\beta}$ is entirely generated by the translational motion of particles within the volume element V.

The total angular momentum $L_{\alpha\beta}^{tot}$ is a conserved quantity. The total angular momentum density $l_{\alpha\beta}^{tot} = L_{\alpha\beta}^{tot}/V$ thus obeys a continuity equation in the continuum limit

$$\partial_t l_{\alpha\beta}^{tot} = \partial_\gamma M_{\alpha\beta\gamma}^{tot} + \tau_{\alpha\beta}^{ext} + r_\alpha f_\beta^{ext} - r_\beta f_\alpha^{ext} \quad. \tag{2.22}$$

Here, $M_{\alpha\beta\gamma}^{tot}$ is the total angular momentum flux and $\tau_{\alpha\beta}^{ext}$ is the externally applied bulk torque. The total angular momentum density consists of an orbital angular momentum density $r_\alpha g_\beta - r_\beta g_\alpha$ and a spin angular momentum density $l_{\alpha\beta} = L_{\alpha\beta}/V = l_{\alpha\beta}^{tot} - (r_\alpha g_\beta - r_\beta g_\alpha)$ which obeys

$$l_{\alpha\beta} = I_{\alpha\beta\gamma\delta}\Omega_{\gamma\delta} \quad. \tag{2.23}$$

The flux of spin angular momentum is given by

$$M_{\alpha\beta\gamma}^{\pi} = M_{\alpha\beta\gamma}^{tot} - M_{\alpha\beta\gamma}^{\sigma} \quad , \tag{2.24}$$

where $M_{\alpha\beta\gamma}^{\sigma} = r_\alpha \sigma_{\beta\gamma}^{tot} - r_\beta \sigma_{\alpha\gamma}^{tot}$ is the orbital angular momentum flux. Note that, while $l_{\alpha\beta}^{tot}$ and its flux $M_{\alpha\beta\gamma}^{tot}$ are explicitly coordinate system dependent, the spin angular momentum density $l_{\alpha\beta}$ and the spin angular momentum flux $M_{\alpha\beta\gamma}^{\pi}$ are not. In the spatially homogeneous system they therefore have no gradients. From Eqs. (2.11) and (2.22) we obtain continuity equations for the spin and the orbital angular momentum densities,

$$\partial_t \left(r_\alpha g_\beta - r_\beta g_\alpha \right) - \partial_\gamma M_{\alpha\beta\gamma}^{\sigma} = 2\sigma_{\alpha\beta}^{tot,a} + r_\alpha f_\beta^{ext} - r_\beta f_\alpha^{ext} \quad , \tag{2.25}$$

$$\partial_t l_{\alpha\beta} - \partial_\gamma M_{\alpha\beta\gamma}^{\pi} = -2\sigma_{\alpha\beta}^{tot,a} + \tau_{\alpha\beta}^{ext} \quad . \tag{2.26}$$

Eqs. (2.26) and (2.25) are coupled by the antisymmetric stress, which describes the conversion between spin and orbital angular momentum [26]. Note that the antisymmetric tensors $\Omega_{\alpha\beta}$ and $l_{\alpha\beta}$ can be equivalently represented by axial vectors, $\Omega_\alpha = \epsilon_{\alpha\beta\gamma}\Omega_{\beta\gamma}/2$ and $l_\alpha = \epsilon_{\alpha\beta\gamma}l_{\beta\gamma}/2$, where $l_\alpha = I_{\alpha\beta}\Omega_\beta$ with $I_{\alpha\beta} = \epsilon_{\alpha\delta\gamma}\epsilon_{\beta\mu\nu}I_{\delta\gamma\mu\nu}$, where $\epsilon_{\alpha\beta\gamma}$ is the Levi-Civita symbol, which is the pseudo-tensor that is antisymmetric with respect to any permutation of indices and $\epsilon_{xyz} = 1$. In the following we will use both notations interchangeably.

2.1.5 Energy conservation and entropy production

The total internal energy U of the fluid is a conserved quantity. It obeys

$$\dot{U} = \dot{W} - \int_{\partial V} dS_\alpha J_\alpha^{(U)} \quad , \tag{2.27}$$

where W is work and $\mathbf{J^{(U)}}$ is the flux of internal energy. Dots denote time derivatives. The power $\dot{W}$ is given by,

$$\dot{W} = \int_V dx^3 \left(\frac{1}{2}\Omega_{\alpha\beta}\tau_{\alpha\beta}^{ext} + v_\alpha f_\alpha^{ext} \right) \quad , \tag{2.28}$$

where $\frac{1}{2}\Omega_{\alpha\beta}\tau_{\alpha\beta}^{ext}$ is the power density exerted by external bulk torques and $v_\alpha f_\alpha^{ext}$ is the the power density exerted by external bulk forces.

The internal energy is related to the free energy F of the system via the relation

$$F = U - TS \quad , \tag{2.29}$$

where S is the entropy. Since here we consider an isothermal system $\dot{T} = 0$. The entropy S however changes with time according to the equation,

$$\dot{S} = \dot{\Theta} - \int_{\partial V} dS_\alpha J_\alpha^{(S)} \quad , \tag{2.30}$$

where $\dot{\Theta}$ is the entropy production rate and $\mathbf{J}^{(\mathbf{S})}$ is the entropy flux. In a system out of equilibrium entropy is constantly produced and the rate of entropy production is given by

$$T\dot{\Theta} = -\dot{F} + \dot{W} + \int_{\partial V} dS_\alpha J_\alpha^{(F)} \quad , \tag{2.31}$$

where

$$\mathbf{J}^{(\mathbf{F})} = \mathbf{J}^{(\mathbf{U})} - T\mathbf{J}^{(\mathbf{S})} \quad . \tag{2.32}$$

This relation will later allow us to identify the thermodynamic fluxes and forces of the system to obtain constitutive material equations.

2.2   Continuously broken symmetries

In complex fluids the constituent molecules can be anisotropic. For instance swimming bacteria have a well defined front and back, and so do actin filaments in the cytoskeleton. If particles locally align this gives rise to continuously broken symmetries. In suspensions of swimming bacteria, the symmetry can be broken by swarms of bacteria aligning their direction of motion . In the cytoskeleton symmetry can be locally broken when cytoskeletal filaments arrange or bundle. For this reason we now consider that each of the $6N$ particles of our fluid has an orientation vector $\mathbf{p}^{(i)}$.

(a) Isotropic

$|\mathbf{n}| = 0$

$|\mathbf{p}| = 0$

(b) Nematic

$|\mathbf{n}| = 1$

$|\mathbf{p}| = 0$

(c) Polar

$|\mathbf{n}| = 1$

$|\mathbf{p}| = 1$
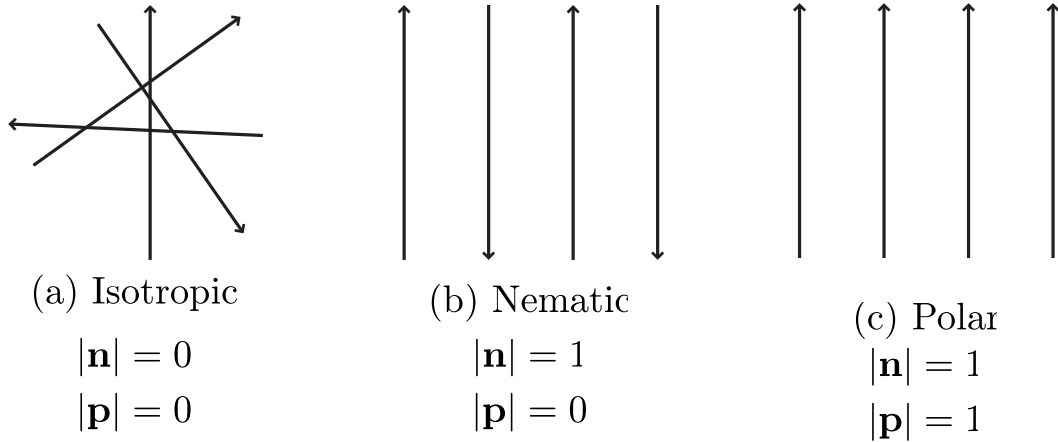
Figure 2.2: Continuous broken symmetries: The arrows denote the microscopic orientations $\mathbf{p}^{(i)}$ of particles. The system is in an isotropic state in (a), in a nematic state in (b) and in a polar state in (c).

2.2.1   Polar and nematic order

The fluid is said be locally ordered if the local distribution of $\mathbf{p}^{(i)}$ has non-vanishing moments. The first moment of the local distribution of particle orientations is the

polarity vector

$$\mathbf{p} = \sum_{\mathbf{x}^{(i)} \in V} \mathbf{p}^{(i)} / \sum_{\mathbf{x}^{(i)} \in V} \quad . \tag{2.33}$$

The vector $\mathbf{p}$ local if particles are locally aligned and parallel, see Fig. 2.2 (c). It is zero in an isotropic solution, see Fig. 2.2 (a), or if the if the particles are aligned but anti-parallel, see Fig. 2.2 (b). Such a nematic alignment is captured by the second moment of the distribution which is the nematic order tensor,

$$
\begin{aligned}
Q_{\alpha\beta} &= \sum_{\mathbf{x}^{(i)} \in V} \left(p_\alpha^{(i)} p_\beta^{(i)} - \frac{1}{3} p_\gamma^{(i)} p_\gamma^{(i)} \delta_{\alpha\beta} \right) / \sum_{\mathbf{x}^{(i)} \in V} \\
&= n_\alpha n_\beta - \frac{1}{3} \delta_{\alpha\beta} n_\gamma n_\gamma.
\end{aligned} \tag{2.34}
$$

The nematic tensor Q can be represented via the director $\mathbf{n}$ without loss of generality. In the discussion that follows, we focus on the polarity vector $\mathbf{p}$. It can however be generaliyed to the nematic vector $\mathbf{n}$ when considering, that in nematic fluids only terms that are invariant with respect to the transformation $\mathbf{n} \to -\mathbf{n}$ can appear. Higher moments of the filament distribution are usually ignored.

2.2.2 Distortion free energy

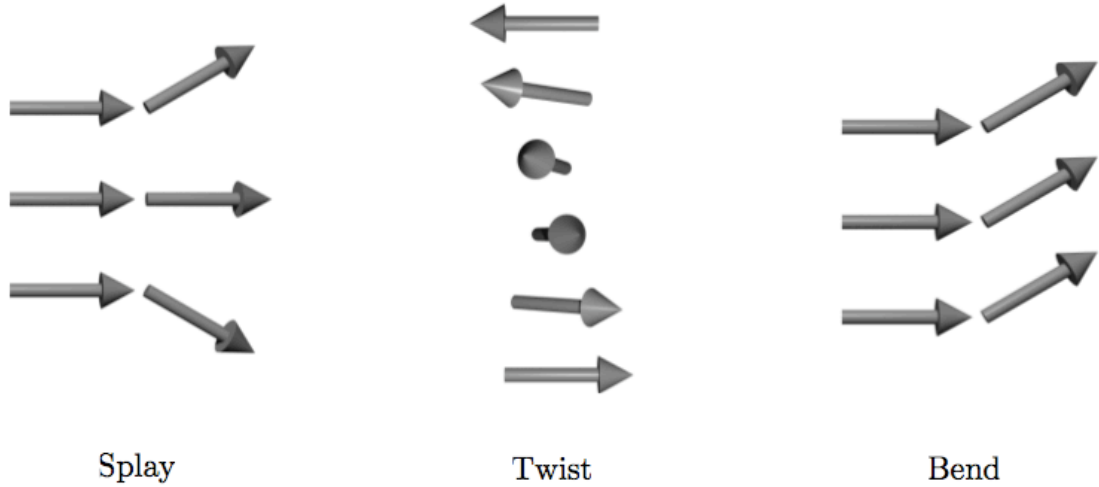

Splay   Twist   Bend

Figure 2.3: Modes of distortion of a nematic liquid crystal: (a) splay distortion; (b) twist distortion; (c) bend distortion.

The free energy density f_0, associated with the polarity field, is called the distortion free energy and

$$f_0 = f_0(p_\alpha, \partial_\beta p_\alpha) \quad . \tag{2.35}$$

In general, f_0 is a function of the vector field $\mathbf{p}$ and its spacial derivatives. A generic expression for f_0 can be obtained by writing all terms allowed by symmetry up to second order in spacial derivatives [27]. One finds

$$f_0 = K_1(\partial_\alpha p_\alpha + k_0)^2 + K_2(p_\alpha \epsilon_{\alpha\beta\gamma} \partial_\beta p_\gamma + q_0)^2 + K_3(\epsilon_{\alpha\beta\gamma} \epsilon_{\gamma\delta\mu} p_\beta \partial_\delta p_\mu)^2 + \lambda(p_\gamma p_\gamma - 1)^2 \quad ,$$
(2.36)

which is the Frank free energy. The distortion free energy Eq. (2.36) depends on six phenomenological coefficients that describe the properties of the polarity field. K_1 is the splay modulus, K_2 the twist modulus and K_3 the bend modulus. These three modes of deformations are sketched in Fig. 2.3. The coefficients k_0 and q_0 describe the spontaneous splay and twist of the material. Note that spontaneous bend is generally forbidden by symmetry. Furthermore spontaneous splay can only exist in polar fluids since the corresponding term is not symmetric with respect to the transformation $\mathbf{p} \to -\mathbf{p}$. Finally spontaneous twist is a property that is unique to chiral fluids, since the corresponding term changes sign with respect to mirroring at the origin of the coordinate system, i.e. $x \to -x$, $y \to -y$ and $z \to -z$. The coefficient λ penalizes the amplitude fluctuations of $\mathbf{p}$.

2.2.3   The polar distortion field

If the polarity field is locally displaced from its equilibrium direction the distortion free energy $F_0 = \int dx^3 f_0(p_\alpha, \partial_\beta p_\alpha)$ changes like

$$\delta F_0 \;=\; \int dx^3 \left(\frac{\partial f_0}{\partial p_\alpha} \delta p_\alpha + \frac{\partial f_0}{\partial(\partial_\beta p_\alpha)} \delta \partial_\beta p_\alpha \right) = \int dx^3 \left(-h_\alpha \delta p_\alpha + \partial_\beta \left(\frac{\partial f_0}{\partial(\partial_\beta p_\alpha)} \delta p_\alpha \right) \right) \quad .$$
(2.37)

Here we have introduced the conjugate variable to the polarity vector, the polar distortion field

$$h_\alpha = -\frac{\partial f_0}{\partial p_\alpha} + \partial_\gamma \frac{\partial f_0}{\partial \partial_\gamma p_\alpha} \quad .$$
(2.38)

For this reason a complex fluid, unlike a simple fluid, can carry torques. Under infinitesimal rotations defined by the pseudo-vector $\delta\theta_\alpha$, with $\delta p_\alpha = \epsilon_{\alpha\beta\gamma} \delta\theta_\beta p_\gamma$ equation 2.37 reads

$$\delta F_0 = -\int_V dx^3 \epsilon_{\alpha\beta\gamma} p_\beta h_\gamma \delta\theta_\alpha - \int_{\partial V} dS_\beta \frac{1}{2} M^e_{\alpha\gamma\beta} \epsilon_{\alpha\gamma\delta} \delta\theta_\delta \quad .$$
(2.39)

We identify the angular momentum flux carried by the polarization field as

$$M^e_{\alpha\beta\gamma} = \frac{\partial f_0}{\partial(\partial_\gamma p_\beta)} p_\alpha - \frac{\partial f_0}{\partial(\partial_\gamma p_\alpha)} p_\beta \quad .$$
(2.40)

To illustrate the importance of the angular momentum flux $M^e_{\alpha\beta\gamma}$ we turn to a simple example: the twisted nematic.
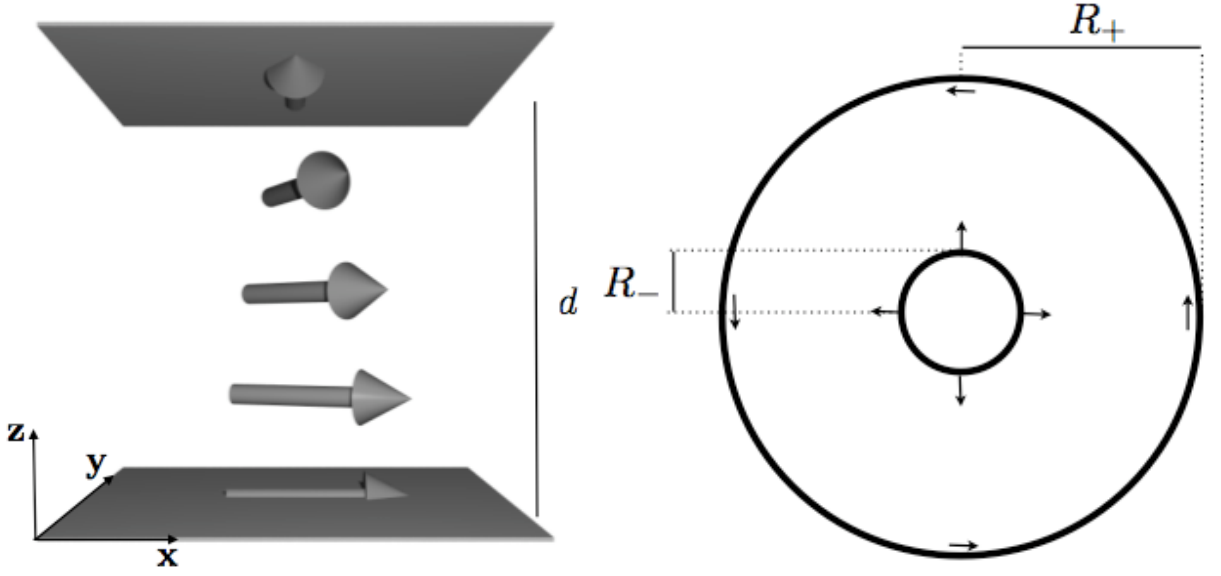
Figure 2.4: Sketches of a twisted nematic (left) and the magical spiral (right).

2.2.4 The twisted nematic

Consider a nematic fluid confined between two parallel plates in the xy plane at $z = 0$ and $z = d$ as shown in the left panel of Fig. 2.4 (left). The boundary conditions are such that $\mathbf{p}(0) = \hat{e}_x$ and $\mathbf{p}(d) = \hat{e}_y$. The vector $\mathbf{p}$ is confined to the xy-plane and its length fixed to one, such that $p_x = \cos\psi$ and $p_y = \sin\psi$. The distortion free energy is then

$$f_0 = K_2(\nabla\psi)^2 \quad , \tag{2.41}$$

where we choose $q_0 = 0$ such that the material has no spontaneous twist, for simplicity. The fluid between the two plates is in equilibrium when $\mathbf{h} = 0$. With the boundary conditions we find,

$$\psi(z) = \frac{\pi}{2d}z \quad . \tag{2.42}$$

It follows immediately that a constant angular momentum flux

$$M^e_{xyz} = 2K_2\partial_z\psi = K_2\frac{\pi}{d} \neq 0 \quad , \tag{2.43}$$

flows through the system. A constant torque needs to be applied between the two plates to maintain this steady state. This example illustrates that in contrast to Newtonian fluids, complex fluids can carry torques.

2.3 The hydrostatic stress

The total stress tensor can be divided in a hydrostatic and a dynamic contribution. The fluid we consider is in local equilibrium, such that locally the microscopic degrees of

freedom relax rapidly towards a distribution that is set by a few slow variables. The hydrostatic stress is the contribution to the total stress that is generated by microscopic degrees of freedom for given values of the slow variables. The hydrostatic stress can be non-vanishing even in equilibrium . In a simple fluid it is given by the hydrostatic pressure. In complex fluids it is given by the Ericksen stress [23, 24, 27, 34]. We now derive an expression for the hydrostatic stress.

2.3.1   Derivation of the Ericksen stress

If the system is in local equilibrium, the free energy density $f(g_\alpha, l_\alpha, p_\alpha, \partial_\beta p_\alpha, n_i)$ is well defined. The free energy of a volume V of fluid is given by

$$
F = \int_V dx^3 f(g_\alpha, l_\alpha, p_\alpha, \partial_\beta p_\alpha, n_i) = \int_V dx^3 \left(\frac{g_\gamma g_\gamma}{2\rho} + \frac{I_{\gamma\delta}^{-1}}{2} l_\gamma l_\delta + f_0(p_\alpha, \partial_\beta p_\alpha) + \mu_i n_i \right) \quad .
$$
(2.44)

We define the chemical potential, $\mu_i^{tot} = \partial F/\partial n_i$, and the polar distortion field $\mathbf{h}^{tot} = -\delta F/\delta \mathbf{p}$. Note that μ_i^{tot} and h^{tot} are different from the equilibrium chemical potential μ_i and the equilibrium distortion field $\mathbf{h} = -\delta F_0/\delta \mathbf{p}$ by kinetic contributions. We obtain an expression for infinitesimal variations of the free energy,

$$
\delta F = \int_{\partial V} \left[f u_\alpha \delta_{\alpha\beta} + \frac{\partial f_0}{\partial(\partial_\beta p_\gamma)} \delta p_\gamma \right] dS_\beta + \int_V dx^3 \left[v_\alpha \delta g_\alpha + \Omega_\alpha \delta l_\alpha - h_\alpha^{tot} \delta p_\alpha + \mu_i^{tot} \delta n_i \right]
$$
(2.45)

where vector $\mathbf{u}$ describes an infinitesimal displacement of the boundary. Now consider the transformation where $\delta g_\alpha = -u_\gamma \partial_\gamma g_\alpha$ and alike for δp_α , δl_α and δn_i. This is the transformation, where the values of all hydrodynamic fields are convected with the deformation field $\mathbf{u}$. Then δF reads,

$$
\begin{aligned}
\delta F \;=\; & \int_{\partial V} \left\{ (f - n_i \mu_i^{tot} - g_\gamma v_\gamma - l_\gamma \Omega_\gamma) \delta_{\alpha\beta} - \frac{\partial f}{\partial(\partial_\beta p_\gamma)} \partial_\alpha p_\gamma \right\} u_\alpha dS_\beta \\
& + \int_V dx^3 u_\gamma \left(g_\alpha \partial_\gamma v_\alpha + l_\alpha \partial_\gamma \Omega_\alpha + h_\alpha^{tot} \partial_\gamma p_\alpha + n_i \partial_\gamma \mu_i^{tot} \right) \\
& + \int_V dx^3 \left(\mu_i^{tot} n_i + g_\alpha v_\alpha + l_\gamma \Omega_\gamma \right) \partial_\gamma u_\gamma \quad .
\end{aligned}
$$
(2.46)

We identify the hydrostatic stress from the surface term as

$$
\sigma_{\alpha\beta}^e = (f - n_i \mu_i^{tot} - g_\gamma v_\gamma - l_\gamma \Omega_\gamma) \delta_{\alpha\beta} - \frac{\partial f}{\partial(\partial_\beta p_\gamma)} \partial_\alpha p_\gamma.
$$
(2.47)

The hydrostatic stress tensor $\sigma_{\alpha\beta}^e$ is known from the liquid crystal literature as the Ericksen stress and is a generalization of the hydrostatic pressure [23, 24, 27, 34].

2.3.2 Properties of the hydrostatic stress

The hydrostatic stress has some interesting properties that follow from the translational and rotational invariance of the fluid. The system is translation invariant. Therefore the variation with constant $\mathbf{u}$ does not change the free energy and $\delta F = 0$. This yields the Gibbs-Duhem relation,

$$\partial_\beta \sigma^e_{\alpha\beta} = -g_\gamma \partial_\alpha v_\gamma - l_\gamma \partial_\alpha \Omega_\gamma - h^{tot}_\gamma \partial_\alpha p_\gamma - n_i \partial_\alpha \mu^{tot}_i, \qquad (2.48)$$

which couples gradients of the Ericksen stress to gradients of the other intensive variables.

Moreover the free energy is invariant towards rotations. A rotation by an infinitesimal angle θ is the transformation where, $u_\alpha = \epsilon_{\alpha\beta\gamma}\theta_\beta r_\gamma$, $\delta p_\alpha = -u_\gamma \partial_\gamma p_\alpha + \epsilon_{\alpha\beta\gamma}\theta_\beta p_\gamma$, $\delta l_\alpha = -u_\gamma \partial_\gamma l_\alpha + \epsilon_{\alpha\beta\gamma}\theta_\beta l_\gamma$, $\delta g_\alpha = -u_\gamma \partial_\gamma g_\alpha + \epsilon_{\alpha\beta\gamma}\theta_\beta g_\gamma$, $\delta n_i = 0$ and $\delta F = 0$. This imposes a condition on the antisymmetric part of the Ericksen stress $\sigma^{e,a}$,

$$\sigma^{e,a}_{\alpha\beta} = \frac{1}{2}\left\{ \partial_\gamma M^e_{\alpha\beta\gamma} + (h^{tot}_\alpha p_\beta - h^{tot}_\beta p_\alpha) - (\Omega_\alpha l_\beta - \Omega_\beta l_\alpha) \right\}. \qquad (2.49)$$

Interestingly in a complex fluid the antisymmetric stress be non-vanishing even in equilibrium. Comparing Eq. (2.49) expression to the torque balance Eq. (2.22), we see that the antisymmetric stress can exert a torque on the boundary even in equilibrium. This observation is best understood when considering the example of the magical spiral [27].

2.3.3 The magical spiral

Consider a complex fluid confined between two cylinders of radius R_- and R_+ oriented along the z-axis as shown in the right panel of Fig. 2.4. The polarity vector is confined to the xy-plane and normalized to one, such that $\mathbf{p} = \cos\psi \,\hat{\mathbf{e}}_r + \sin\psi \,\hat{\mathbf{e}}_\theta$ in cylindrical coordinates. Furthermore for simplicity the polarity field shall be be rotationally symmetric and isotropic in the z direction, and $K_1 = K_3 = K$. The polar distortion field is given by

$$h_\perp = K\frac{1}{r}\partial_r(r\partial_r\psi) \quad, \qquad (2.50)$$

with $h_\perp = (p_r h_\theta - p_\theta h_r)$. Consider the boundary conditions $\psi(R_-) = 0$ (the polarity field is normal to the wall of the inner cylinder) and $\psi(R_+) = \frac{\pi}{2}$ (the polarity field is parallel to the wall of the outer cylinder). In equilibrium where $h_\perp = 0$ we then find

$$\psi(r) = \frac{\pi}{2}\frac{\ln r - \ln R_-}{\ln R_+ - \ln R_-} \quad. \qquad (2.51)$$

An angular momentum flux through this configuration is induced by the polarity field and exerts a net torque on the system walls,

$$\int_0^{2\pi} d\theta\, r M^e_{r\theta r} = \pi^2 K\left[\ln\left(R_+\right) - \ln\left(R_-\right)\right] \quad. \qquad (2.52)$$

If this was the only torque acting in the system the magical spiral would be a perpetuum mobile, which is of coarse impossible. In fact, the torque exerted on the boundary by the antisymmetric part of the hydrostatic stress exactly cancels the torque exerted by the polarization field as can be seen directly from Eq. (2.49). This example shows the critical importance of considering the anisotropic part of the hydrostatic stress properly when considering complex fluid [27]. We will discuss a generalization of the magical spiral to active systems in chapter 3.

This concludes our discussion of the hydrostatic properties of complex fluids. We next discuss its dynamics.

2.4   Hydrodynamics of active fluids

We now derive equations of motion for the slow variables. For this purpose, we first obtain constitutive equations for the complex fluid by identifying the thermodynamic fluxes and forces from the rate of entropy production $\dot{\Theta}$. Close to equilibrium the thermodynamic fluxes are linear functions of the thermodynamic forces. We obtain constitutive equations by writing down all terms allowed by symmetry respecting the Onsager reciprocity principle. We then combine the constitutive relations, the hydrostatic properties of the fluid and the conservation laws of the system to obtain dynamic equations. We start by deriving the entropy production rate.

2.4.1   Entropy production rate

We consider a variation of the free energy where $\delta F = \dot{F}\delta t$, $u_\gamma = v_\gamma \delta t$, $\delta g_\alpha = \partial_t g_\alpha \delta t$, $\delta l_\alpha = \partial_t l_\alpha \delta t$, $\delta p_\alpha = \partial_t p_\alpha \delta t$, and $\delta n^i = \partial_t n^i \delta t$, and find

$$
\begin{aligned}
\dot{F} &= \int_{\partial V} \left[f v_\alpha \delta_{\alpha\beta} + \frac{\partial f_0}{\partial(\partial_\beta p_\gamma)} \partial_t p_\gamma \right] dS_\beta \\
&+ \int_V dx^3 \left[v_\alpha \partial_t g_\alpha + \frac{1}{2}\Omega_{\alpha\beta}\partial_t l_{\alpha\beta} - h_\alpha^{tot}\partial_t p_\alpha + \mu_i^{tot}\partial_t n_i \right] \quad .
\end{aligned}
\tag{2.53}
$$

In order to identify the entropy production rate we need to identify the parts of $\dot{F}$ that stem from free energy fluxes, the part comes from external work, and the part that is the proper entropy production rate. To guide us, we will use the invariance of the entropy production rate to changes of coordinate system, i.e. that it is invariant to translations and rotations. To recast the expression for $\dot{F}$ in the appropriate form we start by using the force balance Eq (2.11), the Gibbs-Duhem relation Eq. (2.48) and performing a

partial integration, this can be rewritten as,

$$
\begin{aligned}
\dot{F} \;=\; & \int\limits_{\partial V} \left[f v_\alpha \delta_{\alpha\beta} + \frac{\partial f_0}{\partial(\partial_\beta p_\gamma)} \partial_t p_\gamma + \left\{ \sigma^{tot}_{\alpha\beta} - \sigma^e_{\alpha\beta} - (n_i \mu^{tot}_i + \Omega_\gamma l_\gamma)\delta_{\alpha\beta} \right\} v_\alpha \right] dS_\beta \\
& + \int\limits_{V} dx^3 \left[v_\alpha f^{ext}_\alpha - (\sigma^{tot}_{\alpha\beta} - \sigma^e_{\alpha\beta} + g_\alpha v_\beta - n_i \mu^{tot}_i \delta_{\alpha\beta}) \partial_\beta v_\alpha \right. \\
& \left. + \frac{1}{2}\Omega_{\alpha\beta}(\partial_t l_{\alpha\beta} + \partial_\gamma(l_{\alpha\beta} v_\gamma)) - h^{tot}_\alpha \frac{d}{dt} p_\alpha + \mu^{tot}_i \frac{d}{dt} n_i \right] \quad .
\end{aligned}
\tag{2.54}
$$

We split the stress tensor in its symmetric its and antisymmetric part and write

$$
\begin{aligned}
(\sigma^{tot}_{\alpha\beta} - \sigma^e_{\alpha\beta})\partial_\beta v_\alpha \;=\; & \left\{ \sigma^{tot}_{\alpha\beta} - \sigma^{tot,a}_{\alpha\beta} - (\sigma^e_{\alpha\beta} - \sigma^{e,a}_{\alpha\beta}) \right\} u_{\alpha\beta} \\
& -(\sigma^{tot,a}_{\alpha\beta} - \sigma^{e,a}_{\alpha\beta})\omega_{\alpha\beta} \quad ,
\end{aligned}
\tag{2.55}
$$

where we introduced the strain rate $u_{\alpha\beta} = \frac{1}{2}\left(\partial_\alpha v_\beta + \partial_\beta v_\alpha\right)$ and the vorticity $\omega_{\alpha\beta} = \frac{1}{2}\left(\partial_\alpha v_\beta - \partial_\beta v_\alpha\right)$. The torque balance (2.22) together with Eq. (2.49) reads

$$
\begin{aligned}
\partial_t l_{\alpha\beta} + \partial_\gamma(l_{\alpha\beta} v_\gamma) \;=\; & \partial_\gamma \left\{ M^{tot}_{\alpha\beta\gamma} - M^e_{\alpha\beta\gamma} - (r_\alpha \sigma^{tot}_{\beta\gamma} - r_\beta \sigma^{tot}_{\alpha\gamma}) + l_{\alpha\beta} v_\gamma \right\} \\
& -2(\sigma^{tot,a}_{\alpha\beta} - \sigma^{e,a}_{\alpha\beta}) - (h^{tot}_\alpha p_\beta - h^{tot}_\beta p_\alpha) \\
& +(\Omega_\alpha l_\beta - \Omega_\beta l_\alpha) + \tau^{ext}_{\alpha\beta} \quad .
\end{aligned}
\tag{2.56}
$$

The particle number conservation Eq. (2.7) can be rewritten as

$$
\mu^{i,tot}(\partial_t n^i + \partial_\alpha(n^i v_\alpha)) = -\partial_\alpha \left(j^i_\alpha \frac{\mu^{i,tot}}{m^i} \right) + j^i_\alpha \partial_\alpha \frac{\mu^{i,tot}}{m^i} + \mu^{i,tot} R^i \quad .
\tag{2.57}
$$

By definition $\sum_{i=1}^{k} \mathbf{j}^i = 0$. We therefore introduce $\bar{\mu}_i = \frac{\mu^{tot,i} m^k - \mu^{tot,k} m^i}{m^i m^k}$. Using that $\Omega_\alpha \Omega_{\alpha\beta} l_\beta = 0$ by construction we find

$$
\begin{aligned}
\dot{F} =\ & \int_{\partial V} \left[f v_\alpha \delta_{\alpha\beta} + \frac{\partial f_0}{\partial(\partial_\beta p_\gamma)} \partial_t p_\gamma + (\sigma^{tot}_{\alpha\beta} - \sigma^e_{\alpha\beta} - (n_i \mu^{tot}_i + \Omega_\gamma l_\gamma) \delta_{\alpha\beta}) v_\alpha \right. \\
& \left. + \frac{1}{2} \Omega_{\alpha\delta} \left\{ M^{tot}_{\alpha\beta\gamma} - M^e_{\alpha\beta\gamma} - (r_\alpha \sigma^{tot}_{\beta\gamma} - r_\beta \sigma^{tot}_{\alpha\gamma}) + l_{\alpha\beta} v_\gamma \right\} - j^i_\beta \frac{\mu^{tot}_i}{m_i} \right] dS_\beta \\
& + \int_V dx^3 \left(\frac{1}{2} \Omega_{\alpha\beta} \tau^{ext}_{\alpha\beta} + v_\alpha f^{ext}_\alpha \right) \\
& + \int_V dx^3 \left[- \left\{ \sigma^{tot}_{\alpha\beta} - \sigma^{tot,a}_{\alpha\beta} - (\sigma^e_{\alpha\beta} - \sigma^{e,a}_{\alpha\beta}) + g_\alpha v_\beta \right\} u_{\alpha\beta} - \left(\sigma^{tot,a}_{\alpha\beta} - \sigma^{e,a}_{\alpha\beta} \right) (\Omega_{\alpha\beta} - \omega_{\alpha\beta}) \right. \\
& - \frac{1}{2} \left\{ M^{tot}_{\alpha\beta\gamma} - M^e_{\alpha\beta\gamma} - (r_\alpha \sigma^{tot}_{\beta\gamma} - r_\beta \sigma^{tot}_{\alpha\gamma}) + l_{\alpha\beta} v_\gamma \right\} \partial_\gamma \Omega_{\alpha\beta} - h^{tot}_\alpha \left(\frac{d}{dt} p_\alpha + \Omega_{\alpha\beta} p_\beta \right) \\
& \left. + \sum_{i=1}^{k-1} j^i_\alpha \partial_\alpha \bar{\mu}_i + R_i \mu^{tot}_i \right] \quad ,
\end{aligned}
$$
(2.58)

Equation (2.58) is the Gallilei invariant way of writing the change of free energy $\dot{F}$. Since we know the expression for the external power,

$$
\dot{W} = \int_V dx^3 \left(\frac{1}{2} \Omega_{\alpha\beta} \tau^{ext}_{\alpha\beta} + v_\alpha f^{ext}_\alpha \right) \quad ,
$$
(2.59)

we can unambiguously identify the free energy flux over the boundaries $\mathbf{J}^{(F)}$

$$
\begin{aligned}
-J^{(F)}_\beta =\ & f v_\alpha \delta_{\alpha\beta} + \frac{\partial f_0}{\partial(\partial_\beta p_\gamma)} \partial_t p_\gamma + (\sigma^{tot}_{\alpha\beta} - \sigma^e_{\alpha\beta} - (n_i \mu^{tot}_i + \Omega_\gamma l_\gamma) \delta_{\alpha\beta}) v_\alpha \\
& + \frac{1}{2} \Omega_{\alpha\delta} \left\{ M^{tot}_{\alpha\beta\gamma} - M^e_{\alpha\beta\gamma} - (r_\alpha \sigma^{tot}_{\beta\gamma} - r_\beta \sigma^{tot}_{\alpha\gamma}) + l_{\alpha\beta} v_\gamma \right\} - j^i_\beta \frac{\mu^{tot}_i}{m_i} \quad ,
\end{aligned}
$$
(2.60)

and the entropy production rate,

$$
\begin{aligned}
T \dot{\Theta} =\ & \int dx^3 \left\{ \sigma_{\alpha\beta} u_{\alpha\beta} + \sigma^a_{\alpha\beta} (\Omega_{\alpha\beta} - \omega_{\alpha\beta}) - \frac{1}{2} M_{\alpha\beta\gamma} \partial_\gamma \Omega_{\alpha\beta} \right. \\
& \left. + h^{tot}_\alpha \frac{D}{Dt} p_\alpha - \sum_{i=1}^{k-1} j^i_\alpha \partial_\alpha \bar{\mu}_i - \mu^{tot}_i R^i \right\} \quad .
\end{aligned}
$$
(2.61)

Here

$$
\sigma_{\alpha\beta} = \sigma^{tot}_{\alpha\beta} - \sigma^e_{\alpha\beta} - \sigma^a_{\alpha\beta} + g_\alpha v_\beta
$$
(2.62)

is the symmetric part of the deviatoric stress,

$$\sigma_{\alpha\beta}^{a} = \sigma_{\alpha\beta}^{tot,a} - \sigma_{\alpha\beta}^{e,a} \tag{2.63}$$

is the antisymmetric part of the deviatoric stress,

$$M_{\alpha\beta\gamma} = M_{\alpha\beta\gamma}^{\pi} - M_{\alpha\beta\gamma}^{e} + v_{\gamma}l_{\alpha\beta} \tag{2.64}$$

is the deviatoric internal angular momentum density flux, and

$$\frac{D}{Dt}p_{\alpha} = \frac{d}{dt}p_{\alpha} + \Omega_{\alpha\beta}p_{\beta} \tag{2.65}$$

is the co-rotational time derivative of the **p**-field.

The constitutive equation of the complex fluid can be obtained by linearly expanding the thermodynamic fluxes in terms of thermodynamic forces.

2.4.2   Constitutive relations of an active chiral fluid.

For simplicity, we assume a three component fluid made of the gel, the fuel molecules and their reaction products. If the concentrations of fuel and reaction products are kept constant by contact with an external buffer $\mathbf{j}^{i} = 0$ and $\mu_{i}^{tot}R^{i}$ can be rewritten as $r\Delta\mu$, where $r = R^{\text{product}} = -R^{\text{fuel}}$ and $\Delta\mu = \bar{\mu}^{\text{fuel}} - \bar{\mu}^{\text{product}}$. The fluid is kept out of equilibrium by the consumption of a chemical fuel that is hydrolyzed at a rate r. The chemical energy difference between the fuel and its reaction products is denoted $\Delta\mu$. In the main text we assume a constant local supply of fuel molecules and that the reaction products are constantly evacuated such that $\Delta\mu$ is a constant. The entropy production associated to the consumption of fuel is $r\Delta\mu/T$. The entropy production rate simplifies to,

$$T\dot{\Theta} = \int dx^{3} \left\{ \sigma_{\alpha\beta}u_{\alpha\beta} + \sigma_{\alpha\beta}^{a}(\Omega_{\alpha\beta} - \omega_{\alpha\beta}) + \frac{1}{2}M_{\alpha\beta\gamma}\partial_{\gamma}\Omega_{\alpha\beta} + h_{\alpha}^{tot}\frac{D}{Dt}p_{\alpha} + r\Delta\mu \right\} \quad . \tag{2.66}$$

Equation (2.66) leads us to identify the following thermodynamic fluxes and forces. The thermodynamic fluxes are the deviatoric shear stress $\sigma_{\alpha\beta}$, the deviatoric antisymmetric stress, $\sigma_{\alpha\beta}^{a}$, the deviatoric angular momentum density flux, $M_{\alpha\beta\gamma}$ the co-rotational time derivative of the **p**-field, Dp_{α}/Dt and the rate of fuel consumption r. The thermodynamic forces are the symmetric strain rate $u_{\alpha\beta}$, the rotational strain rate $\Omega_{\alpha\beta} - \omega_{\alpha\beta}$, the polar distortion field $\mathbf{h^{tot}}$ and the free energy difference between fuel molecules and their reaction products $\Delta\mu$.

We obtain constitutive equations by expanding the thermodynamic fluxes as linear functions of the thermodynamic forces, respecting the symmetries of the system and Onsager reciprocity principle. Here, we include all terms allowed by symmetry up to second order **p**. Because of chiral asymmetry, the tensor $\epsilon_{\alpha\beta\gamma}$ can be used to create

couplings. For simplicity, we ignore anisotropic viscous terms and passive chiral terms, which are not the focus of this work. The constitutive equations then read:

$$
\sigma_{\alpha\beta} = 2\eta u_{\alpha\beta} + \frac{\nu_1}{2}\left(p_\alpha h_\beta^{tot} + p_\beta h_\alpha^{tot}\right) + \bar{\nu}p_\gamma h_\gamma^{tot}\delta_{\alpha\beta} + \bar{\zeta}\delta_{\alpha\beta}\Delta\mu
$$
$$
+\zeta p_\alpha p_\beta \Delta\mu \quad , \tag{2.67}
$$

$$
\sigma_{\alpha\beta}^a = 2\eta'\left(\Omega_{\alpha\beta} - \omega_{\alpha\beta}\right) + \frac{\nu_2}{2}\left(h_\alpha^{tot}p_\beta - h_\beta^{tot}p_\alpha\right) + \tilde{\zeta}\Delta\mu\epsilon_{\alpha\beta\gamma}p_\gamma \quad , \tag{2.68}
$$

$$
M_{\alpha\beta\gamma} = \kappa_0\partial_\gamma\Omega_{\alpha\beta} + \zeta_1\epsilon_{\alpha\beta\gamma}\Delta\mu + \zeta_2\Delta\mu\epsilon_{\alpha\beta\delta}p_\delta p_\gamma + \zeta_3\Delta\mu(\epsilon_{\alpha\gamma\delta}p_\delta p_\beta - \epsilon_{\beta\gamma\delta}p_\delta p_\alpha)
$$
$$
+\zeta_4\Delta\mu(\delta_{\alpha\gamma}p_\beta - \delta_{\beta\gamma}p_\alpha) \quad , \tag{2.69}
$$

$$
\frac{Dp_\alpha}{Dt} = \frac{1}{\gamma}h_\alpha^{tot} + \lambda_1 p_\alpha\Delta\mu - \nu_1 p_\beta u_{\alpha\beta} - \bar{\nu}u_{\beta\beta}p_\alpha - \nu_2\left(\Omega_{\alpha\beta} - \omega_{\alpha\beta}\right)p_\beta \quad , \tag{2.70}
$$

$$
r = \Lambda\Delta\mu + \lambda_1 p_\alpha h_\alpha^{tot} + \bar{\zeta}u_{\alpha\alpha} + \zeta p_\alpha p_\beta u_{\alpha\beta} + \tilde{\zeta}\left(\Omega_{\alpha\beta} - \omega_{\alpha\beta}\right)\epsilon_{\alpha\beta\gamma}p_\gamma
$$
$$
+\frac{\zeta_1}{2}\epsilon_{\alpha\beta\gamma}\partial_\gamma\Omega_{\alpha\beta} + \frac{\zeta_2}{2}\epsilon_{\alpha\beta\delta}p_\delta p_\gamma\partial_\gamma\Omega_{\alpha\beta} + \frac{\zeta_3}{2}(\epsilon_{\alpha\gamma\delta}p_\delta p_\beta - \epsilon_{\beta\gamma\delta}p_\delta p_\alpha)\partial_\gamma\Omega_{\alpha\beta}
$$
$$
+\frac{\zeta_4}{2}(\delta_{\alpha\gamma}p_\beta - \delta_{\beta\gamma}p_\alpha)\partial_\gamma\Omega_{\alpha\beta} \quad . \tag{2.71}
$$

We have introduced the viscosities η, η' and γ. The coefficients ν_1, $\bar{\nu}$, and ν_2 describe the coupling between the polarity vector and velocity gradients. The coeffient κ_0 accounts for dissipative angular momentum fluxes generated by gradients of local rotation rates $\Omega_{\alpha\beta}$. The coefficient λ_1 describes magnitude changes of the vector $\mathbf{p}$ due to active processes. The coefficient $\bar{\zeta}$ describes the isotropic active stresses, ζ the anisotropic active stress and $\tilde{\zeta}$ the active antisymmetric stress. Active antisymmetric stresses and active angular momentum fluxes appear as a result of the action of active chiral processes in the fluid. These contributions are described by the coefficients ζ_1, ζ_2, ζ_3, ζ_4 and $\tilde{\zeta}$ which describe the strength and densities of isotropic, nematic rod , nematic ring, polar chiral, and polar ring motors respectively, that we will discuss in chapter 4.

2.4.3   Equations of motion

Knowing the constitutive equations, we can write down the equations of motion of the fluid. The first equation of motion is given by the force balance,

$$
\partial_t g_\alpha = \partial_\beta\left(\sigma_{\alpha\beta} + \sigma_{\alpha\beta}^a + \sigma_{\alpha\beta}^e - g_\alpha v_\beta\right) + f_\alpha^{ext} \quad . \tag{2.72}
$$

The second equation of motion is the angular momentum balance,

$$
\partial_t l_{\alpha\beta} = \partial_\gamma\left(M_{\alpha\beta\gamma} - v_\gamma l_{\alpha\beta}\right) - 2\sigma_{\alpha\beta}^a - (h_\alpha p_\beta - h_\beta p_\alpha) + (\Omega_\alpha l_\beta - \Omega_\beta l_\alpha) + \tau_{\alpha\beta}^{ext} \quad . \tag{2.73}
$$

They are completed by the dynamic equation of motion for the polarity equation (2.70) and the mass continuity equation (2.4).

2.5   Simpler fluids as limiting cases of the generic theory

In this section we discuss two limiting cases of the generic theory we developed. The first limit we discuss is that of a Newtonian fluid, where we show how to recover the

Navier Stokes equation. Then we discuss how to recover the limit of older theories for active fluids, that did not consider a local spin degree of freedom.

2.5.1 The Newtonian fluid

The constitutive equations for the Newtonian fluid are

$$\sigma_{\alpha\beta} = 2\eta u_{\alpha\beta} \quad , \tag{2.74}$$

$$\sigma^a_{\alpha\beta} = 2\eta' \left(\Omega_{\alpha\beta} - \omega_{\alpha\beta}\right) \quad , \tag{2.75}$$

$$M_{\alpha\beta\gamma} = \kappa_0 \partial_\gamma \Omega_{\alpha\beta} \quad . \tag{2.76}$$

The equations of motion (2.72) and (2.73) then read

$$\partial_t g_\alpha + \partial_\beta(v_\beta g_\alpha) = 2\eta\partial_\beta u_{\alpha\beta} + 2\eta'\partial_\beta \left(\Omega_{\alpha\beta} - \omega_{\alpha\beta}\right) - \partial_\alpha P \tag{2.77}$$

and

$$\partial_t l_{\alpha\beta} + \partial_\gamma(v_\gamma l_{\alpha\beta}) = \kappa_0 \partial^2_\gamma \Omega_{\alpha\beta} - 4\eta' \left(\Omega_{\alpha\beta} - \omega_{\alpha\beta}\right) \quad , \tag{2.78}$$

respectively, where we used the fact that the moment of inertia tensor is diagonal for the Newtonian fluid. Moreover the fluid is incompressible, such that

$$\partial_\alpha v_\alpha = 0 \quad . \tag{2.79}$$

If we finally use $l_{\alpha\beta} = I\Omega_{\alpha\beta}$,

$$\frac{dg_\alpha}{dt} = \eta\partial^2_\gamma v_\alpha - \partial_\alpha P + \frac{\kappa_0}{4\eta'} \left(\partial^2_\gamma - \frac{I}{\kappa_0}\frac{d}{dt}\right) \left[\frac{dg_\alpha}{dt} - (\eta + \eta')\partial^2_\gamma v_\alpha + \partial_\alpha P\right] \tag{2.80}$$

Equation (2.80) is the Navier Stokes equation with some additional higher order correction terms that are proportional to κ_0/η', which has the dimension of a length squared, and is thus set by some molecular scale length of the system. In the limit where the molecular length scale $l = \sqrt{\kappa_0/\eta'}$ tends to zero, Eq. (2.80) converges to the well known form of the the Navier-Stokes equation.

2.5.2 Active fluids without spin degree of freedom

We now discuss how to recover earlier theories for active fluids do not explicitly consider the spin degree of freedom of the angular momentum [27, 32–34]. These older theories for active fluids where derived under the assumption that there are no dissipative contribution to the angular momentum flux [27], i.e.

$$M_{\alpha\beta\gamma} = 0 \quad , \tag{2.81}$$

and thus

$$M^\pi_{\alpha\beta\gamma} = M^e_{\alpha\beta\gamma} \quad . \tag{2.82}$$

The torque balance Eq.(2.22) then reads

$$\sigma_{\alpha\beta}^{tot,a} = \frac{1}{2}\partial_\gamma M_{\alpha\beta\gamma}^e \quad . \tag{2.83}$$

Using the Eq. (2.49) for the antisymmetric part of the Erickson stress one finds that

$$\sigma_{\alpha\beta}^a = \sigma_{\alpha\beta}^{tot,a} - \sigma_{\alpha\beta}^{e,a} = -\frac{1}{2}\left(h_\alpha p_\beta - h_\beta p_\alpha\right) \quad . \tag{2.84}$$

The entropy production rate Eq. (2.66) then simplifies to

$$T\dot{\Theta} = \int\limits_V dx^3 \left(\sigma_{\alpha\beta} u_{\alpha\beta} + \frac{\tilde{D}p_\alpha}{\tilde{D}t} h_\alpha + r\Delta\mu\right) \quad , \tag{2.85}$$

where

$$\frac{\tilde{D}p_\alpha}{\tilde{D}t} = \partial_t p_\alpha + v_\gamma\partial_\gamma p_\alpha + \omega_{\alpha\beta}p_\beta \quad . \tag{2.86}$$

Interestingly the intrinsic rotation rate $\Omega_{\alpha\beta}$ drops out of Eq. (2.85). From Eq. (2.85) we identify the thermodynamic fluxes $\sigma_{\alpha\beta}$, $\tilde{D}p_\alpha/\tilde{D}t$, and r as well as the respective corresponding thermodynamic forces $u_{\alpha\beta}$, h_α, and $\Delta\mu$, of the simplified theory. Expanding the fluxes in terms of the forces, respecting the symmetries of the system and the Onsager reciprocity principle, we obtain the generic constitutive equations of the active polar fluid [33]:

$$2\eta u_{\alpha\beta} = \sigma_{\alpha\beta} - \frac{\nu_1}{2}\left(p_\alpha h_\beta + p_\beta h_\alpha\right) - \bar{\nu}_1 p_\gamma h_\gamma \delta_{\alpha\beta} + \bar{\zeta}\delta_{\alpha\beta}\Delta\mu + \zeta p_\alpha p_\beta\Delta\mu$$
$$+ \zeta' p_\gamma p_\gamma \delta_{\alpha\beta}\Delta\mu \quad , \tag{2.87}$$

$$\frac{Dp_\alpha}{Dt} = \frac{1}{\gamma}h_\alpha + \lambda_1 p_\alpha \Delta\mu - \nu_1 p_\beta u_{\alpha\beta} - \bar{\nu}_1 u_{\beta\beta} p_\alpha \quad , \tag{2.88}$$

$$r = \Lambda\Delta\mu + \lambda_1 p_\alpha h_\alpha + \bar{\zeta} u_{\alpha\alpha} + \zeta p_\alpha p_\beta u_{\alpha\beta} + \zeta' p_\alpha p_\alpha u_{\beta\beta} \quad . \tag{2.89}$$

The same simplified constitutive equations Eqns (2.67)-(2.71) can also be obtained by making appropriate choices for the phenomenological coefficients in the more general constitutive equations (2.67) to (2.71).

2.6   Summary

In the present chapter we derived a generic theory for active fluids. In contrast to earlier theories for active fluids we explicitly consider a spin degree of freedom. Similar work had been considered earlier in liquid crystals [24,28], here we extend it to active systems.

Our derivation is based on conservation laws and symmetry arguments only, and is independent of any assumption on the microscopic mechanisms in the fluid and is thus generic. This approach allowed us to systematically identify active contributions to the angular momentum flux and the antisymmetric stress, that were previously unknown.

We discussed how previously known theories for fluids emerge from the theoretical framework that we presented here, as simple limiting cases. Notably we explained how to recover the Navier-Stokes equation and how to recover older theories of active fluids without spin degrees of freedom. In previous work on active fluids the key assumption was that there are no dissipative contributions to the angular momentum flux. This assumption obviously breaks down in fluids where active chiral processes generate torque dipoles in the fluid on microscopic scales, and directly generate dissipative angular momentum fluxes.

Chapter 3

The Taylor-Couette motor: Spontaneous chiral symmetry breaking

In the last chapter we derived generic theory for active fluids. Here and in the following, we use this theory to discuss active chiral processes. In the present chapter we discuss an example for the complex rheological properties of active fluids, showing how chiral motion can be generated by a spontaneous symmetry breaking process, in a fluid that is not chiral. We consider a fluid that obeys the constitutive equation derived in Sec. 2.5.2 in a Taylor Couette geometry.

The results of the present chapter have been obtained in close collaboration with Marc Neef and professor Karsten Kruse from the university of Saarbrücken, and have been published here [36]. The text closely follows reference [36].

3.1 Taylor-Couette geometry

In the Taylor-Couette geometry a fluid is confined between two impermeable concentric cylinders of radii R_+ and R_-, as shown in Fig. 3.1 (a).

In the classical Taylor Couette setup the two cylinders are rotated by applying an external torque, and the resulting flow fields are studied. A large number of instabilities of such externally driven flows are known, some of which have been analyzed in remarkable detail [92]. In this context, complex fluids such as ferrofluids in the presence of a magnetic field or visco-elastic fluids have also been considered. For the latter, notably, finite-amplitude instabilities of linearly stable states have been found even at low Reynolds numbers if elastic stresses decay sufficiently slowly [93, 94].

Here we study an active fluid in the Taylor-Couette geometry. We will discuss situations where the two cylinders are either stationary or rotate relative to each other at a rate $\Delta\omega$. At low Reynolds number we can choose to keep the inner cylinder fixed without loss of generality. We only consider cases that are invariant with respect to
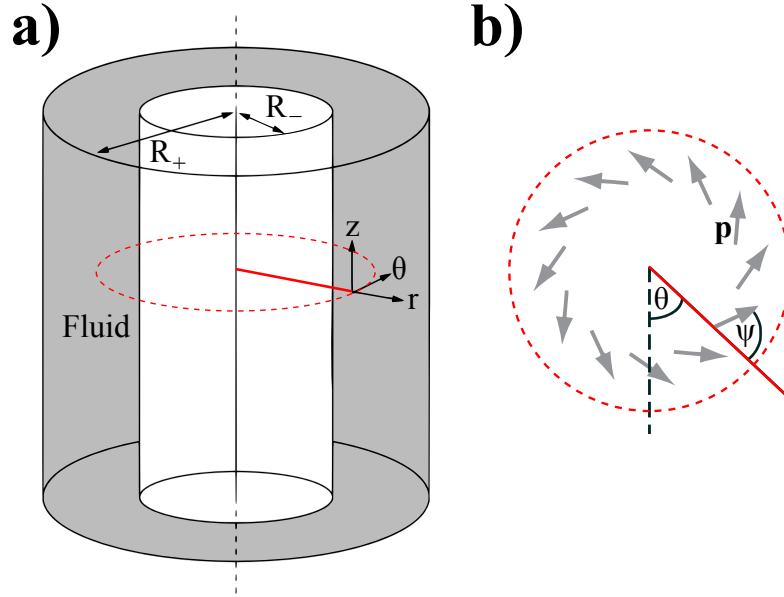
Figure 3.1: Schematic illustration of the Taylor-Couette geometry. a) Fluid between two coaxial cylinders with radii R_- and R_+. The system is invariant under translations along and rotations around the z-axis. b) Planar cut perpendicular to the z-axis. The polarization vector $\mathbf{p}$ and the polarization angle ψ with $\mathbf{p} = (\cos\psi, \sin\psi)$ are shown.

rotations around and translations along the cylinders' long axes. Furthermore, the fluid is incompressible, which together with the symmetry constraints we impose leads to $v_r = 0$. Finally, the fluid we consider has a local polarity $\mathbf{p}$. We only consider cases where the vector $\mathbf{p}$ is confined to the $r - \theta$ plane. Furthermore, since the magnitude of $\mathbf{p}$ is not a hydrodynamic variable, we only consider the orientation dynamics of the polarity vector. The orientational dynamics is captured by choosing $\mathbf{p}^2 = 1$. Therefore, the polarity $\mathbf{p}$ can be expressed in terms of the polarization angle ψ such that $p_r = \cos\psi$ and $p_\theta = \sin\psi$, see Fig. 3.1 (b).

3.2   Boundary forces and torques

The Taylor-Couette system permits to apply a torque $\Gamma^+ = -\Gamma^-$ per unit axial length on the outer and inner cylinder surfaces, respectively, such that the total torque $\Gamma^+ + \Gamma^-$ on the surface vanishes.

We only consider situations where the total external force and torque applied on the system is zero and where external bulk forces and torques vanish, i.e. $f_\alpha^{ext} = 0$ and $\tau_{\alpha\beta}^{ext} = 0$. In this case, external forces $\sigma_{\alpha\gamma}^{tot} dS_\gamma$ and torques

$$d\Gamma_{\alpha\beta} = dS_\gamma M_{\alpha\beta\gamma}^{\text{tot}} \tag{3.1}$$

can still act locally on the boundary ∂V at a surface element dS_γ pointing outward.

Vanishing external force and torque imply $\int_{\partial V} \sigma^{tot}_{\alpha\gamma} dS_\gamma = 0$ and

$$\int\limits_{\partial V} d\Gamma_{\alpha\beta} = \int\limits_{\partial V} dS_\gamma M^{\text{tot}}_{\alpha\beta\gamma} = 0 \quad . \tag{3.2}$$

Note that even if the total flux $M^{tot}_{\alpha\beta\gamma}$ vanishes at the boundary, the contributions due to $M_{\alpha\beta\gamma}$ and $\sigma^{tot}_{\alpha\beta}$ can be nonzero according to Eq. (2.22). Using Eq. (3.1) we find an expression for the torque Γ_- applied to the outer cylinder,

$$\Gamma^- = -\int\limits_0^{2\pi} d\theta \, r M^{\text{tot}}_{\theta rr}(r,\theta) \quad , \tag{3.3}$$

which is independent of r for $R^- \le r \le R^+$ because of angular momentum conservation. Using Eqs. (2.22) and (2.87), this implies

$$\Gamma^- = \int_0^{2\pi} d\theta \, r^2 \left(\sigma_{\theta r} + \frac{1}{2}(h_r p_\theta - h_\theta p_r) \right) \quad . \tag{3.4}$$

3.3   Equation of motion and boundary conditions

We now present the equations of motion governing the system in polar coordinates. The only non-vanishing component of the strain rate tensor is $u_{\theta r}$. From Eq. (2.87) we obtain

$$2\eta u_{\theta r} = \sigma_{\theta r} - \frac{\nu_1}{2} \left(h_\perp \cos 2\psi + h_\parallel \sin 2\psi \right) + \frac{\zeta}{2} \Delta\mu \sin 2\psi \quad , \tag{3.5}$$

where $h_\parallel = \mathbf{h} \cdot \mathbf{p}$ and $h_\perp = h_r p_\theta - h_\theta p_r$. Projecting Eq. (2.88) onto the directions parallel and perpendicular to the polarization vector yields

$$\frac{1}{\gamma} h_\parallel = \nu_1 u_{\theta r} \sin 2\psi - \lambda_1 \Delta\mu \tag{3.6}$$

$$\partial_t \psi = \frac{1}{\gamma} h_\perp - u_{\theta r} (\nu_1 \cos 2\psi - 1) \quad . \tag{3.7}$$

The parallel component of the distortion field $h_\parallel = \mathbf{p} \cdot \mathbf{h}$ acts as a Lagrange multiplier to impose the constraint $\mathbf{p}^2 = 1$. The perpendicular component $h_\perp$ is the torque exerted by the polarization field and is given by the expression $h_\perp = -\delta F / \delta \psi$. The force balance Eq. (2.11) becomes

$$\partial_r \left(\sigma_{\theta r} + \frac{h_\perp}{2} \right) + \frac{2\sigma_{\theta r}}{r} + \frac{h_\perp}{r} = 0 \quad , \tag{3.8}$$

where we have neglected inertial terms. Integration of Eq. (3.8) yields,

$$\sigma_{\theta r} = \frac{\Gamma^-}{2\pi r^2} - \frac{1}{2} h_\perp \quad . \tag{3.9}$$

where the integration constant Γ^- is the torque applied between the cylinder as can be seen by comparing Eq. (3.9) and Eq. (3.4). Combining Eqs. (3.5)-(3.7) and (3.9) we obtain the equation of motion for the polarization field:

$$\partial_t \psi = \left[\frac{1}{\gamma} + \frac{(\nu_1^2 \cos^2 2\psi - 1)}{4\eta + \nu_1^2 \gamma (\sin 2\psi)^2} \right] h_\perp - \left(\tilde{\zeta} \Delta\mu \sin 2\psi + \frac{\Gamma^-}{2\pi r^2} \right) \frac{\nu_1 \cos 2\psi - 1}{2\eta + \frac{\nu_1^2 \gamma}{2}(\sin 2\psi)^2} \quad ,$$

(3.10)

where $\tilde{\zeta} = \frac{1}{2}(\zeta + \gamma\nu_1\lambda_1)$. For given polarity field $\psi(r)$ we can determine the flow field v_θ by integrating Eq. (3.5).

The boundary conditions that we consider are the following. We prescribe the polarization angle $\psi = \psi_0$ at both cylinder surfaces at R_- and R_+. We impose no-slip boundary conditions for the velocity of the fluid at both cylinders. At the fixed inner cylinder, this implies $v_\theta(R_-) = 0$, at the outer cylinder $v_\theta(R_+) = \Delta\omega R^+$. At the outer cylinder we have the choice of two ensembles: (i) prescribed torque $\Gamma^+ = -\Gamma^-$ or (ii) prescribed rotation rate $\Delta\omega$. We will discuss both cases.

3.4   Equilibrium steady states

In equilibrium, all thermodynamic fluxes and forces vanish. In particular, $h_\perp = 0$ and $\Delta\mu = 0$. In addition, equilibrium requires that $\Gamma^- = 0$ and that no movements occur, $v_\theta = 0$. The polarization field ψ of an equilibrium steady state is obtained by solving the equation $h_\perp = 0$, with the specified boundary conditions. Choosing the standard Landau-de Gennes form for the free energy of the polarization field,

$$F_p = 2\pi \int dr \, r \left\{ \frac{K}{2} \left(\frac{1}{r}\frac{d}{dr} r \cos\psi \right)^2 + \frac{K + \delta K}{2} \left(\frac{1}{r}\frac{d}{dr} r \sin\psi \right)^2 \right\} \quad , \qquad (3.11)$$

we have

$$h_\perp = -\frac{\delta F_p}{\delta \psi} = (K + \delta K \cos^2(\Psi)) \left(\Psi'' + \frac{\Psi'}{r} \right) - \frac{\delta K}{2} \sin(2\Psi) \left(\frac{1}{r^2} + \Psi'^2 \right) \quad , \qquad (3.12)$$

where primes indicate derivatives with respect to r. In this expression K is the splay elastic modulus and $K + \delta K$ is the bend elastic modulus. If the boundary condition are chosen accordingly equilibrium steady states with a constant $\psi(r) = \psi_0$ exist for certain values of ψ_0. These special solutions are "asters" with $\psi_0 = 0$ or π and "vortices" with $\psi_0 = \pm\pi/2$.

3.5   Non-equilibrium steady states

We now discuss how the equilibrium situation is changed as $\Delta\mu$ becomes nonzero. We start by analyzing the stability of the symmetric aster and vortex states with the boundary condition (i) prescribed torque $\Gamma^- = 0$.

No external torque at the outer surface

We write $\psi(r,t) = \psi_0 + \delta\psi(r,t)$ with $\delta\psi = 0$ at both boundaries. The time evolution described by Eqs. (3.10) can be linearized around a steady state with $\psi = \psi_0$. For aster solutions, i.e. $\psi_0 = 0$ we find,

$$
\begin{aligned}
\partial_t \delta\psi(r,t) &= (K + \delta K) \left(\frac{1}{\gamma} + \frac{\nu_1^2 - 1}{4\eta} \right) \left(\delta\psi''(r,t) + \frac{\delta\psi'(r,t)}{r} \right) \\
&\quad - \delta K \left(\frac{1}{\gamma} + \frac{\nu_1^2 - 1}{4\eta} \right) \frac{\delta\psi(r,t)}{r^2} - \tilde{\zeta}\Delta\mu \frac{\nu_1 - 1}{\eta} \delta\psi(r,t) \quad .
\end{aligned}
\tag{3.13}
$$

Using the separation Ansatz $\delta\psi(r,t) = \delta\psi(r)\, e^{st}$, we can solve for $\delta\psi(r)$

$$
\delta\psi(r) = C_1\, J_n\,(k\,r) + C_2\, Y_n\,(k\,r) \quad ,
\tag{3.14}
$$

where J_n and Y_n are Bessel-Functions of the first kind with $n^2 = \delta K/(K + \delta K)$ and

$$
k^2 = -\frac{2\,(\nu_1 - 1)\,\tilde{\zeta}\,\Delta\mu + 4\,\eta\,s}{\left(4\,\eta/\gamma + (\nu_1^2 - 1)\right)(K + \delta K)} \quad .
\tag{3.15}
$$

Asters are stable if the real parts of all growth exponents s are negative. The possible values k_i of k with $i \in \mathbb{N}$ are restricted by the boundary conditions $\delta\psi(R_-) = \delta\psi(R_+) = 0$. Explicitly, the values k_i satisfy the equation

$$
Y_n(k_i R_+) J_n(k_i R_-) - J_n(k_i R_+) Y_n(k_i R_-) = 0 \quad .
\tag{3.16}
$$

We find that k_i^2 and the corresponding values of s are real. By setting $s = 0$ in Eq. (3.15), we can thus determine a critical value $\tilde{\zeta}\Delta\mu_c$ for the activity, such that asters are unstable if $\tilde{\zeta}\Delta\mu < \tilde{\zeta}\Delta\mu_c$. Explicitly,

$$
\tilde{\zeta}\Delta\mu_c = -k_{\min}^2 \frac{\left(4\,\eta + \gamma(\nu_1^2 - 1)\right)}{2\gamma\,(\nu_1 - 1)} (K + \delta K) \quad ,
\tag{3.17}
$$

where $k_{\min}^2 = \min\{k_i^2\}$. Following the same logic it is also possible to determine the stability of vortices. We find that the activity threshold for the stability of vortices is

$$
\tilde{\zeta}\Delta\mu_c = -l_{\min}^2 \frac{\left(4\,\eta + \gamma(\nu_1^2 - 1)\right)}{2\gamma(\nu_1 + 1)} K \quad ,
\tag{3.18}
$$

where $l_{\min}^2$ is the smallest l^2 satisfying $Y_m(lR_+)J_m(lR_-) - J_m(lR_+)Y_m(lR_-) = 0$ with $m^2 = -\delta K/K$. The limit $R_- \to 0$ corresponds to point defects that where studied in Ref. [33]. Note that our results differ slightly since the sign of the antisymmetric part of the deviatory stress was chosen incorrectly in Ref. [33].

Our predictions on the stability of asters and vortices are in perfect agreement with numerical solutions of the Eq. (3.10). We obtain the bifurcation diagram of the Taylor-Couette motor for $\Gamma^- = 0$ that we display in Figure 3.2 for vortices with $\psi_0 = \pm\pi/2$. The numerical solution allows us to investigate the behavior of the system beyond the

instability. We determine stable steady states with spontaneous fluid flow and rotating outer cylinder which emerge at the bifurcation. The direction of this rotation is determined by a spontaneous symmetry breaking. Therefore two stable branches exist in the bifurcation diagram. Moving further away from the bifurcation point, additional unstable steady states appear. These states correspond to the next higher values of l^2 and have been determined by numerical solutions of the equation for the steady state, see Fig. 3.2.
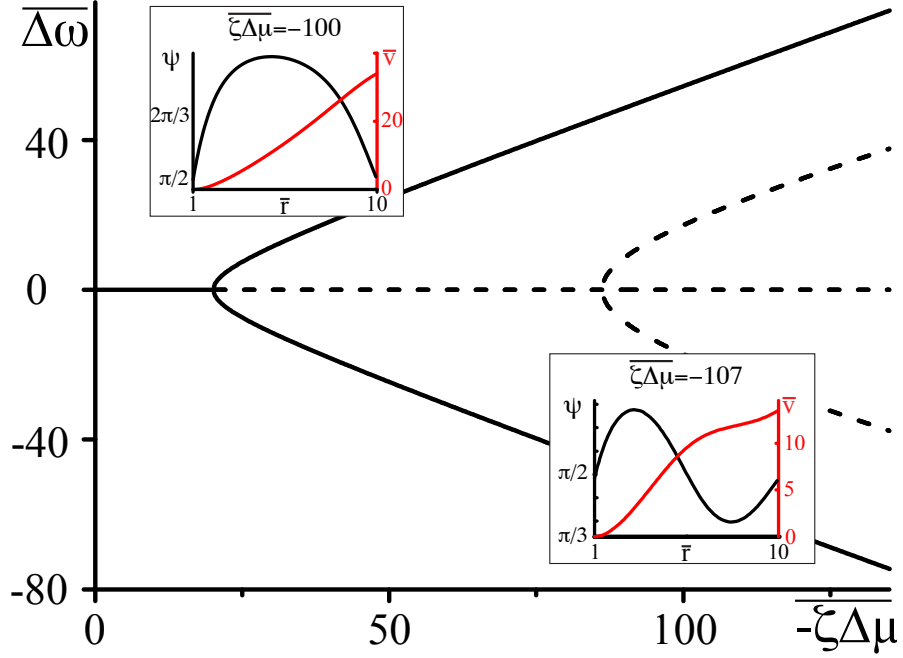

Figure 3.2: Bifurcation diagram for an active polar fluid confined between two coaxial cylinders with the vortex boundary conditions, $\psi(R_-) = \psi(R_+) = \pi/2$ as a function of the dimensionless activity $\overline{\zeta\Delta\mu} = R_+^2 \tilde{\zeta}\Delta\mu/K$. No torque is applied to the outer cylinder $\Gamma^- = 0$. The non-equilibrium steady states are characterized by the angular velocity of the outer cylinder $\overline{\Delta\omega} = \eta v_\theta(R_+)R_+/K$. For $\overline{\zeta\Delta\mu} > \overline{\zeta\Delta\mu}_c = -20.13$, the system exhibits spontaneous flows and rotation. For increasing values of $-\overline{\zeta\Delta\mu}$ further unstable steady states exist with an increasing number of nodes in the polarization angle (dashed lines). The profiles of polarization ψ and dimensionless flow velocity $\bar{v} =$ are shown in the insets for a stable (above, $\overline{\zeta\Delta\mu} = -100$) and unstable (below, $\overline{\zeta\Delta\mu} = -107$) solution as a function of $\bar{r} = r/R^-$. Parameter values are $R = R_-/R_+ = 0.1$, $\eta/\gamma = 2$, $\nu_1 = 2$, and $\delta K = 0$.

3.5.1   The stalled system

The emergence of spontaneous rotations indicates that the system can act as a rotatory motor.
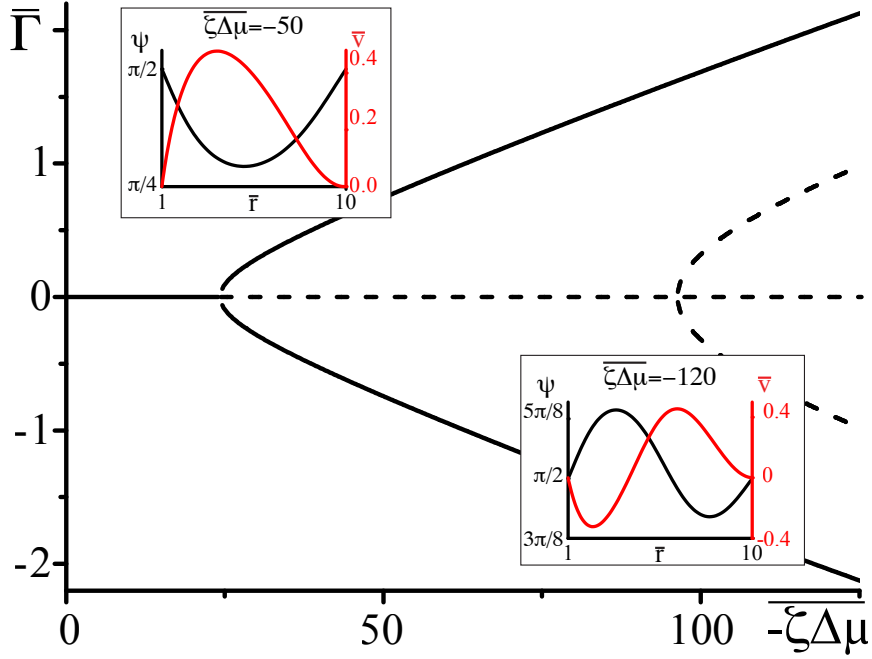
Figure 3.3: Bifurcation diagram for the system shown in Fig. 3.2 but with stall boundary conditions $\overline{\Delta \omega} = 0$. The non-equilibrium steady states are characterized by their torque $\bar{\Gamma} = \Gamma^-/(2\pi)K$. Full lines indicate stable, dashed lines unstable solutions. Insets present a stable solution for $\overline{\tilde{\zeta}\Delta\mu} = -50$ and an unstable solution for $\overline{\tilde{\zeta}\Delta\mu} = -120$. All other parameters are chosen as in Figure 3.2

The stall torque can be determined by imposing $\Delta\omega = 0$. The stability of stalled steady states can be determined by the method described above, however the torque Γ^- becomes time-dependent when the system is linearly perturbed. For the stationary vortex solution with $\psi_0 = \pm\pi/2$, we again find an instability at a critical value $\zeta\Delta\mu_c$ at which spontaneous flows occur. These solutions with $\Delta\omega = 0$ are characterized by non-vanishing torques Γ^-. The symmetry is again broken spontaneously. The bifurcation diagram is shown in Fig. 3.3.

3.5.2 Relation between rotation rate and applied torque

We determine the relation between applied torque Γ^- and rotation rate $\Delta\omega$ by numerically determining stationary solutions of Eqs. (3.5) and (3.7). In the passive case $\tilde{\zeta}\Delta\mu = 0$, the rotation rate $\Delta\omega$ is always proportional to the torque, $\Delta\omega \propto \Gamma^-$ and vanishes for $\Gamma^- = 0$. Our results for finite $\tilde{\zeta}\Delta\mu$ are displayed in Fig. 3.4. For sufficiently small $\tilde{\zeta}\Delta\mu$, the rotation rate $\Delta\omega$ increases monotonically as a function of Γ^-, see Fig. 3.4(a). For $\tilde{\zeta}\Delta\mu = \tilde{\zeta}\Delta\mu_c \simeq -20.134$ a critical point appears. As a consequence, three solutions coexist for $\tilde{\zeta}\Delta\mu < \tilde{\zeta}\Delta\mu_c$, two of which are stable (solid lines) and one is unstable (dashed line), see Fig. 3.4(b). As a consequence, the rotation rate exhibits
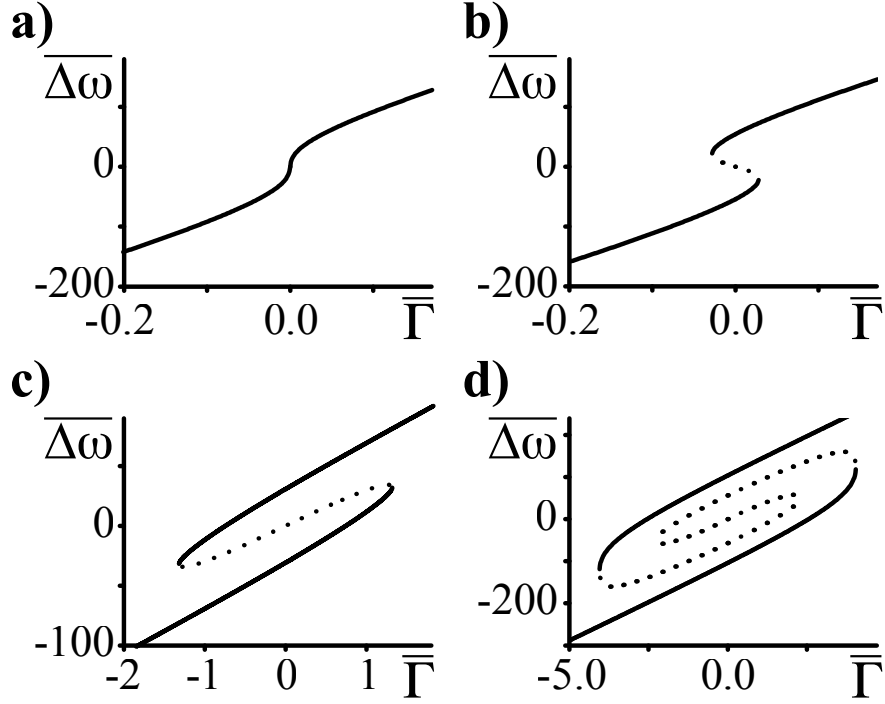
Figure 3.4: Relationship between rotation rate and applied torque of the Taylor-Couette motor with vortex-boundary conditions for different values of the dimensionless active stress $\overline{\zeta\,\Delta\mu}$. Full lines indicate stable, dotted lines unstable steady states. Parameter values are $\overline{\zeta\,\Delta\mu} = -20.134$ (a), $\overline{\zeta\,\Delta\mu} = -22$ (b), $\overline{\zeta\,\Delta\mu} = -100$ (c), and $\overline{\zeta\,\Delta\mu} = -150$ (d). Other parameters are $\eta/\gamma = 2$, $\nu_1 = 2$, and $\delta K = 0$.

discontinuous changes as a function of torque and hysteresis occurs. If $\tilde{\zeta}\Delta\mu$ is decreased further, a more complex set of branches of unstable steady states emerges, see Fig. 3.4 (c) and (d). In all cases there are two stable branches and a regime of hysteresis. Note, that the stable branches always have positive slope, while the slope of unstable branches can have either sign. This relation between torque and rotation rate is very similar to the properties of the force-velocity relation of symmetric collections of molecular motors [95].

3.5.3   Variation of the boundary conditions of the polarization field

Changing the polarization angle ψ_0 leads in general to a non-symmetric motor which has a spontaneous rotation rate even in the absence of a torque. In Fig. 3.5, we show the the steady state rotation rate $\Delta\omega$ for $\Gamma^- = 0$ as a function of the polarization angle ψ_0 at the boundaries for different values of the active stress. This figure shows that the system rotates spontaneously except for $\psi_0 = 0$ and vortices $\pi/2$. As the magnitude of the active stress is increased, unstable branches appear and the rotation rate exhibits discontinuous changes and hysteresis. The instability of the vortex ($\psi_0 = \pi/2$) with the
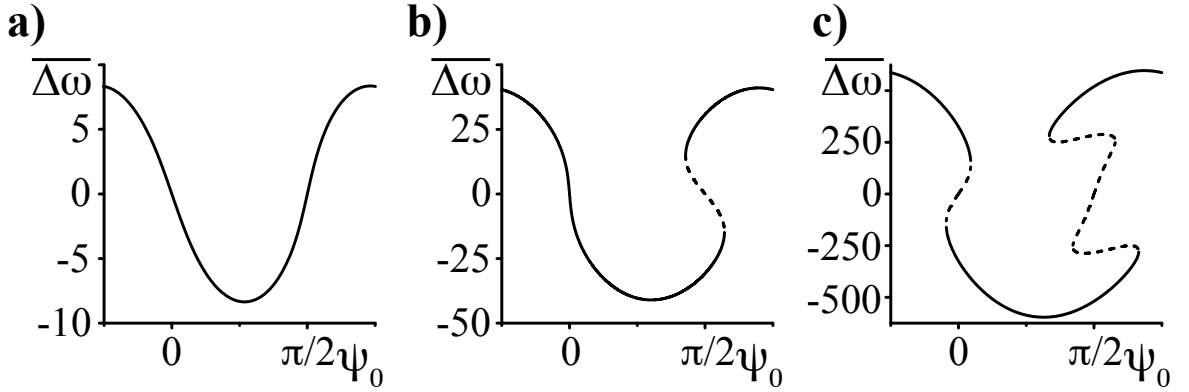
Figure 3.5: Dimensionless rotation rate $\bar{\Delta}\omega$ as a function of the polarization angle $\psi = 0$ at the boundaries in the absence of an external torque and for different values of the active stress $\overline{\zeta\Delta\mu} = -10$ (a), $\overline{\zeta\Delta\mu} = -50$ (b), and $\overline{\zeta\Delta\mu} = -150$ (c). Other parameters are $\eta/\gamma = 2$, $\nu_1 = 2$, and $\delta K = 0$. Stable states are shown as solid lines, unstable states by dashed lines.

aster ($\psi_0 = 0$) still stable is apparent in Fig. 3.5 (b). Similarly Fig. 3.5 (c) reveals the subsequent emergence of additional unstable branches as well as the instability of the vortex at $\psi_0 = \pi/2$.

3.6 A possible experimental realization

To give an idea of the possibility for an experimental realization of the Taylor Coutte, we now estimate critical stresses and the achievable forces and torques for realistic parameter values.

In a Taylor-Couette system with an outer radius $R_+ = 5$mm and an inner radius $R_- = 1$mm, the critical active stress would be on the order of 10^{-6} Pa, and thus the system should start to rotate even at very small active stresses. The order of magnitude of the stall torque can be obtained from $\Gamma \sim |\tilde{\zeta}\Delta\mu|R_+^2$, see Eq. (3.4) and Fig. 3.3. Using again $R_+ \simeq 5$mm and $\zeta\Delta\mu \simeq 10^3$Pa, we estimate a stall torque per unit length $\Gamma \simeq 25 \ 10^{-3}$N. To estimate the corresponding rotation rate $\Delta\omega \sim u_{r\theta}$, we note that it scales as $\Delta\omega \sim |\tilde{\zeta}\Delta\mu|/\eta$, see Eq. (3.5), and Fig. 3.2. The viscosity η of an actin gel can be estimated as $\eta \simeq E\tau$, where E is the gel elastic modulus and τ denotes the characteristic visco-elastic relaxation time. The elastic modulus of a passive actin gel scales as $E \simeq k_B T L_p \lambda^{-4}$, where L_p is the persistence length of actin filaments and λ is the mesh-size of the gel. For $k_B T \simeq 4$pN nm, $L_p \simeq 17\mu$m, and $\lambda \simeq 100$nm [96], we estimate $E \simeq 10^3$Pa, which is consistent with measurements for actin gels under various conditions [97–99]. Using $\tau \simeq 30$s [100], we obtain $\eta \simeq 10^4$Pa s. For $\zeta\Delta\mu \simeq 10^3$Pa, we estimate a rotation rate of about $\Delta\omega \simeq 0.1$ s^{-1}.

The Taylor-Couette motor could be realized at small scales with radii of several μm

using micro-fabrication techniques [101]. This leads to a stall torque of the order of several nN and, since the rotation rate is rather insensitive to the system size again to rotation rates of the order of $0.1s^{-1}$. Note, that when the system size approaches the mesh site of the acto-myosin gel, the hydrodynamic limit will no longer provide an accurate approximation. Note also that a symmetric system would only rotate if the characteristic length ξ is smaller than the system size. However, even in micrometer sized systems, we expect many of the general features and the scaling relations to still hold. Thus, the Taylor-Couette motor described here is a promising candidate for the construction of artificial rotational micro-motors.

3.7   Summary

In this chapter, we analyzed the dynamics of an achiral active polar fluid confined in the Taylor-Couette geometry between two coaxial cylinders. This system is especially interesting since it shows chiral motion through a spontaneous symmetry breaking process.

The active stress can induce spontaneous circular flows, which drive the rotation of the outer cylinder relative to the inner cylinder even in the absence of an externally applied torque. If the polarization angle at the boundary is either parallel or perpendicular to the cylinder wall, relative motion between the two cylinders occurs by spontaneous symmetry breaking if the contractile active stress exceeds a critical value. Beyond this instability two steady states with opposite rotation rate coexist. For any other boundary condition imposed on the polarization, rotation in the absence of torque occurs for non-zero active stress If an external torque is applied between the two cylinders, the system behaves as a rotary motor that can perform mechanical work. In the special cases where the polarization is parallel or perpendicular to the boundary, this motor only works beyond the instability and can act in both senses of rotation. We find dynamic transitions between states of different rotation rates and hysteresis. We sketch possible experimental realizations of the Taylor Couette motor. On larger scales this system might be interesting to experimentally explore the rheological properties of active fluids. On micro-scales it is a promising candidate for the creation of rotational micro-motors.

Chapter 4

Elementary chiral motors

The active terms in the constitutive Eqs (2.67)-(2.71) result from the action of molecular scale force and torque dipoles in the fluid. Densities of such dipoles correspond to active stresses and angular momentum fluxes. In the present chapter we will show that localized distributions of dipoles give rise to the new active terms in Eqs (2.67)-(2.71). We will first list the different torque and chiral force dipole that can be constructed, see Fig 4.1 (left column). We then identify the five elementary motors, see Fig 4.1 (right column), which correspond to localized distributions of force and torque dipoles with different symmetries. Four of these elementary motors are chiral. The fifth, although originating from microscopically chiral processes, is not. We will show that different elementary motors generate flow and rotation fields that differ by their symmetry.

4.1 Chiral force and torque dipoles

In the absence of external forces any microscopic process that generates a force must generate an equal but opposite counterforce as well. This is the nothing but Newtons second law. Thus active processes on the microscopic scale can not generate forces, but only force dipoles. An example of a microscopic process that generates a force dipole is a myosin minifilament pulling two actin filaments towards each other, see Fig. 1.3 (a).

For the same reason microscopic processes can not generate torque monopoles but only torque dipoles. An example of a process generating a torque dipole on the microscopic scale is shown in Fig. 1.3 (b). Myosin motors do not only infer a translational motion to the filaments they act on, but also make them rotate [11], thus generating a torque dipole. Another example for a torque dipole is the bacterium *E. coli*, which consist of rotating flagella, and a counter-rotating cell body, see Fig. 1.7.

4.1.1 Torque dipoles

A torque dipole $\tau_{\alpha\beta}$ consists of two identical torque monopoles of with torque $\pm q_{\alpha\beta}$ that are separated by a distance d along the unit vector $\mathbf{p}^{(i)}$. The torque this object exerts
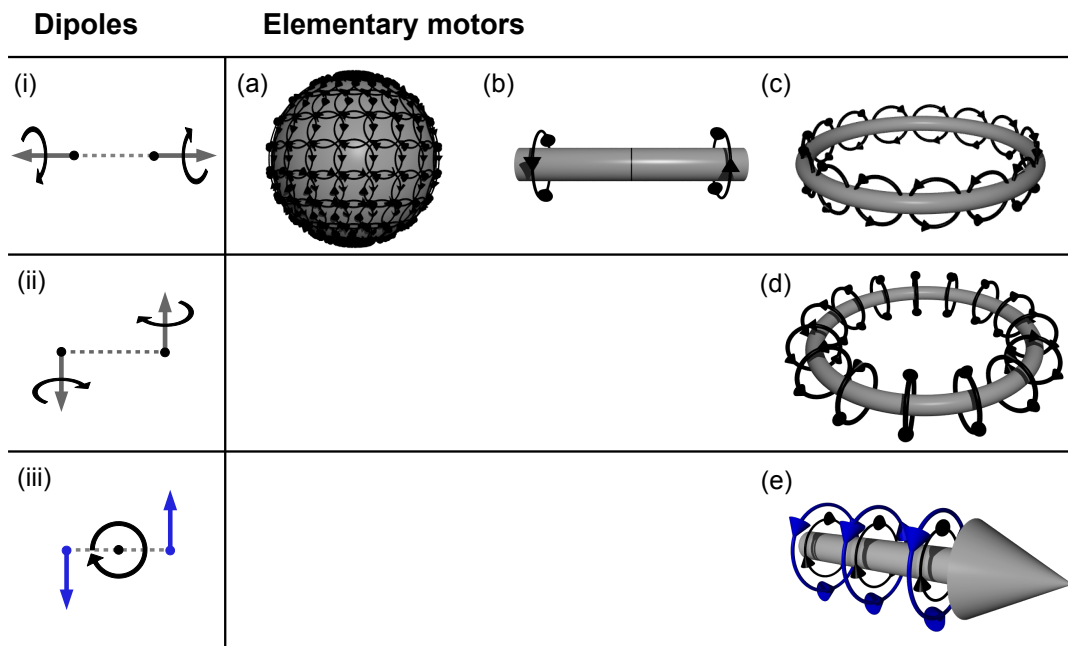
Figure 4.1: Schematic representation of chiral torque and force dipoles as well as elementary motors. We distinguish two types of torque dipoles, (i) and (ii), and introduce a chiral force dipole paired with torque monopole to balance torques (iii). Here gray arrows indicate torques. Their sense of rotation is indicated by curved black arrows. Forces are indicated by blue arrows. The dipoles (i-iii) can be used to create the elementary motors (a-e) of higher symmetry. For details see text.

on the fluid is

$$\tau_{\alpha\beta} \;\; = \;\; q_{\alpha\beta}\left[\delta(\mathbf{r}^{(i)} - d\mathbf{p}^{(i)}/2) - \delta(\mathbf{r}^{(i)} + d\mathbf{p}^{(i)}/2)\right] \tag{4.1}$$

$$\simeq -q_{\alpha\beta}dp_\gamma^{(i)}\partial_\gamma\delta(\mathbf{r}^{(i)}) \quad , \tag{4.2}$$

where $\mathbf{r}^{(i)}$ is the position of the dipole. Comparing this result to the torque balance equation Eq. (2.22) we see that the torque dipole corresponds to an active angular momentum flux

$$M_{\alpha\beta\gamma}^{act} = q_{\alpha\beta}dp_\gamma^{(i)}\partial_\gamma\delta((\mathbf{r}^{(i)}) \quad , \tag{4.3}$$

that obeys

$$\partial_\gamma M_{\alpha\beta\gamma}^{act} = \tau_{\alpha\beta} \quad . \tag{4.4}$$

We distinguish two types of torque dipoles that differ by their symmetry. The torque dipole of type (i) is a torque dipoles in which the axis of the torque monopoles is parallel to the vector $\mathbf{p}^{(i)}$, (see Fig 4.1 (i)). The torque dipole of type (ii) is a torque dipole in which the axis of the torque monopoles is orthogonal to the vector $\mathbf{p}^{(i)}$, (see Fig 4.1 (ii)).

In a torque dipole of type (i)

$$q_{\alpha\beta} = q\epsilon_{\alpha\beta\gamma}p_\gamma^{(i)}. \tag{4.5}$$

This corresponds to an angular momentum flux,

$$M_{\alpha\beta\gamma}^{act} = qd\epsilon_{\alpha\beta\delta}p_\delta^{(i)}p_\gamma^{(i)}\partial_\gamma\delta(\mathbf{r}^{(i)}) \quad . \tag{4.6}$$

In a torque dipole of type (ii)

$$q_{\alpha\beta} = q\epsilon_{\alpha\beta\gamma}t_\gamma \quad , \tag{4.7}$$

where the unit vector $\mathbf{t}$ is orthogonal to $\mathbf{p}^{(i)}$,

$$\mathbf{p}^{(i)} \cdot \mathbf{t} = 0 \quad . \tag{4.8}$$

The angular momentum flux generated by this object is given by

$$M_{\alpha\beta\gamma}^{act} = qd\epsilon_{\alpha\beta\delta}t_\delta p_\gamma^{(i)}\delta(\mathbf{r}^{(i)}) \quad . \tag{4.9}$$

A general torque dipole can be represented as a linear superposition of torque dipoles of type (i) and torque dipoles of type (ii). We now turn to chiral force dipoles.

4.1.2 Chiral force dipoles

A force dipole consist of two opposing force monopoles $\pm\varphi_\alpha$ separated by a distance d along the unit vector $\mathbf{p}^{(i)}$. It exerts a force

$$f_\alpha = \varphi_\alpha(\delta(\mathbf{r}^{(i)} + \mathbf{p}^{(i)}/2) - \delta(\mathbf{r}^{(\mathbf{i})} - \mathbf{p}^{(i)}/2)) \simeq \partial_\gamma(\varphi_\alpha d_\gamma) \quad , \tag{4.10}$$

on the fluid that surrounds it. This dipole can be interpreted as an active contribution to the stress tensor with

$$\sigma_{\alpha\beta}^{act} = \frac{d}{2}\left(\varphi_\alpha p_\beta^{(i)} + \varphi_\beta p_\alpha^{(i)}\right) \quad , \tag{4.11}$$

and

$$\sigma_{\alpha\beta}^{act,a} = \frac{d}{2}\left(\varphi_\alpha p_\beta^{(i)} - \varphi_\beta p_\alpha^{(i)}\right) \quad . \tag{4.12}$$

Force dipoles in which the vector φ is parallel to the vector $\mathbf{p}^{(i)}$, generate symmetric stresses only. Such force dipoles have been discussed extensively in the past [30, 31, 88]. On the other hand if φ is not parallel to the vector $\mathbf{p}^{(i)}$ an antisymmetric stress is also generated. The torque of the force dipole has to be offset by a torque monopole, such that the total torque the object exerts on the fluid,

$$\tau_{\alpha\beta} = (\varphi_\alpha r_\beta^{(i)} - \varphi_\beta r_\alpha^{(i)})\left(\delta(\mathbf{r}^{(i)} + d\mathbf{p}^{(i)}/2) - \delta(\mathbf{r}^{(i)} - d\mathbf{p}^{(i)}/2)\right) + q_{\alpha\beta}\delta(\mathbf{r}^{(i)}) = 0 \quad , \tag{4.13}$$

vanishes. Here

$$q_{\alpha\beta} = -(r_\beta^{(i)}\varphi_\alpha - r_\alpha^{(i)}\varphi_\beta) \quad . \tag{4.14}$$

We call the dipole with φ is orthogonal to the vector $\mathbf{p}^{(i)}$, the chiral force dipole or dipole of type (iii), see Fig 4.1 (iii) The dipole (iii) is a mixed dipole since it consists of two force and one torque monopole.

4.2   Elementary chiral motors

The constitutive equations for the active chiral fluid (2.67) - (2.71) contain several active terms. We now show that all of these are generated by localized distributions of chiral force dipoles (iii) and torque dipoles (i, ii). We call such local distributions of dipoles elementary chiral motors. We identify five different elementary chiral motors that differ by their symmetry. Four of these are chiral. We now discuss them one by one, show how they are generated and discuss the flow and rotation fields they create.

4.2.1   Isotropic chiral motors

The first active term which we discuss is the one parametrized by the coefficient ζ_1 in Eq. (5.3), which corresponds to an isotropic chiral motor. The structure of this motor is sketched in Fig 4.1 (a).

The isotropic chiral motor is generated by a distribution of torque dipoles of type (i) or (ii) whose orientation vectors $\mathbf{p}^{(i)}$ point in all directions with equal likelihood. Consider a collection N of identical torque dipoles of type (i) at positions $\mathbf{r}^{(i)}$. Collectively they generate an angular momentum flux

$$M_{\alpha\beta\gamma}^{act}(\mathbf{r}) \;=\; q\epsilon_{\alpha\beta\delta}\sum_i p_\delta^{(i)} p_\gamma^{(i)} \partial_\gamma \delta(\mathbf{r} - \mathbf{r}^{(i)}) \quad . \tag{4.15}$$

Since the microscopic orientations of the torque dipoles are isotropically distributed we find

$$M_{\alpha\beta\gamma}^{act}(\mathbf{r}) = \zeta_1 \Delta\mu(\mathbf{r})\epsilon_{\alpha\beta\gamma} \quad , \tag{4.16}$$

where $\zeta_1 \Delta\mu(\mathbf{r}) = qdn(\mathbf{r})/3$ and $n(\mathbf{r})$ is the local density of torque dipoles. This corresponds to the isotropic active chiral term in Eq (5.3). A localized distribution $n(\mathbf{r}) = \delta(\mathbf{r})$ corresponds to the the isotropic chiral elementary motor, see Fig. 4.1 (a).

We now consider a single elementary isotropic chiral motor that exerts an angular momentum flux $M_{\alpha\beta\gamma}^{act} = \zeta_1 \epsilon_{\alpha\beta\gamma} \Delta\mu_0 \delta(\mathbf{r})$ and is embedded in an otherwise passive, Newtonian fluid. The stresses and angular momentum fluxes in the fluid are given by

$$\sigma_{\alpha\beta} = 2\eta u_{\alpha\beta} \quad , \tag{4.17}$$

$$\sigma_{\alpha\beta}^a = 2\eta'(\Omega_{\alpha\beta} - \omega_{\alpha\beta}) \quad , \tag{4.18}$$

$$M_{\alpha\beta\gamma} = \kappa_0 \partial_\gamma \Omega_{\alpha\beta} + \zeta_1 \Delta\mu_0 \epsilon_{\alpha\beta\gamma} \delta(\mathbf{r}) \quad . \tag{4.19}$$

We consider no flow boundary conditions at infinity. Using the force balance (2.11) the torque balance (2.22) and the incompressibility condition $\partial_\gamma v_\gamma = 0$, we find the equations of motion for no flows at infinity

$$2\eta \partial_\gamma^2 v_\alpha = \frac{\kappa_0}{2\eta'}(\eta + \eta')\partial_\gamma^4 v_\alpha \tag{4.20}$$

$$0 = \kappa_0 \partial_\gamma^2 \Omega_{\alpha\beta} + \zeta_1 \Delta\mu_0 \epsilon_{\alpha\beta\gamma} \partial_\gamma \delta(\mathbf{r}) - 4\eta'(\Omega_{\alpha\beta} - \omega_{\alpha\beta}) \quad . \tag{4.21}$$

Because ζ_1 does not enter in Eq. (4.20), the velocity field vanishes everywhere, $v_\alpha = 0$. From Eq (4.21) we find that the intrinsic rotation rate obeys an inhomogeneous Helmholtz equation,

$$\Omega_{\alpha\beta} - \frac{\kappa_0}{4\eta'}\partial_\gamma^2 \Omega_{\alpha\beta} = \frac{\zeta_1 \Delta\mu_0}{4\eta'}\epsilon_{\alpha\beta\gamma} \partial_\gamma \delta(\mathbf{r}) \quad . \tag{4.22}$$

In spherical coordinates the intrinsic rotation field $\Omega_{\alpha\beta}$ is thus given by $\Omega_{r\theta} = \Omega_{r\varphi} = 0$ and

$$\Omega_{\theta\varphi} = -\frac{\zeta_1 \Delta\mu_0}{4\pi\kappa_0}e^{-2|\mathbf{r}|/\ell}\left(\frac{2}{|\mathbf{r}|\ell} + \frac{1}{|\mathbf{r}|^2}\right) \quad , \tag{4.23}$$

which decays on the length $\ell = (\kappa_0/\eta')^{1/2}$. Note that in the near field, for $r \ll \ell$, the intrinsic rotation rate $\Omega_{\alpha\beta}$ is different from the vorticity $\omega_{\alpha\beta} = 0$ of the flow and that it vanishes for $\ell \ll r$. Moreover we numerically solve for the intrinsic rotation field using a fast Fourier transform with periodic boundary conditions in a periodic box. The result is displayed in Fig. 4.2.

4.2.2 Nematic chiral rod

We next discuss the active angular momentum flux parametrized by the coefficient ζ_2 in Eq. (5.3). The corresponding elementary motor is the chiral rod, see Fig. 4.1 (b).
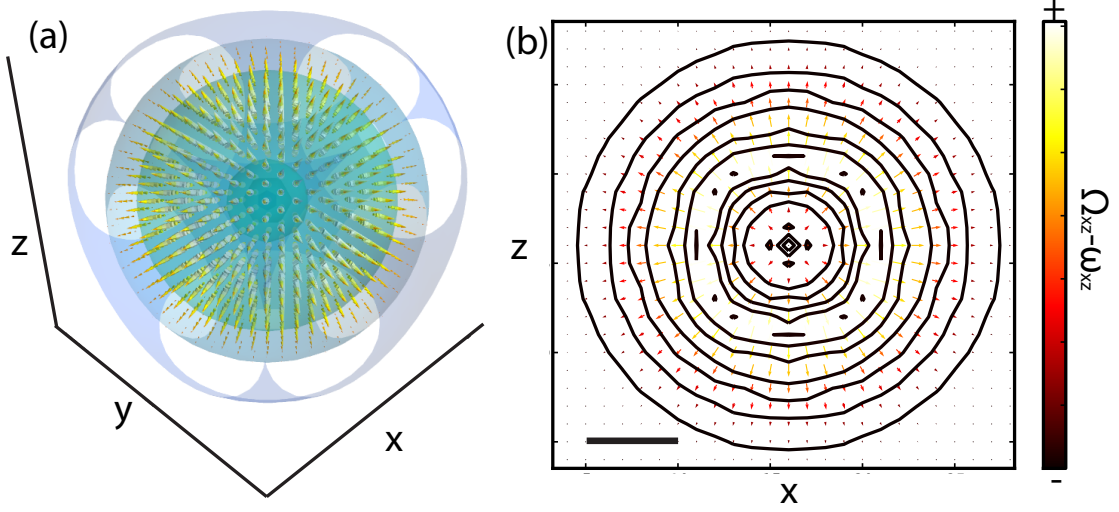
Figure 4.2: Isotropic chiral motor: Difference of intrinsic rotation rate and vorticity in 3d (a) and as a cut through the xz plane (b). Cones and arrows represent $\epsilon_{\alpha\beta\gamma}(\Omega_{\beta\gamma} - \omega_{\beta\gamma})$ in (a) and (b), respectively. Surfaces (a) and lines (b) represent equal magnitudes of $\mathbf{\Omega} - \omega$. The black scale-bar indicates the length ℓ. The parameters are $\eta/\eta' = 1$. The size of the periodic box is 26ℓ.

This object is generated by a distribution of torque dipoles of type (i) if all dipoles are aligned along the unit vector $\mathbf{p}$. Eq. (4.15) then becomes

$$M^{act}_{\alpha\beta\gamma}(\mathbf{r}) = \zeta_2\Delta\mu(\mathbf{r})\epsilon_{\alpha\beta\delta}p_\delta p_\gamma \quad, \tag{4.24}$$

where $\zeta_2\Delta\mu = qdn(\mathbf{r})$ and $n(\mathbf{r})$ is the density of dipoles.

The stresses and angular momentum fluxes induced by an isolated chiral rod motor in an otherwise passive Newtonian fluid are given by

$$\sigma_{\alpha\beta} = 2\eta u_{\alpha\beta} \quad, \tag{4.25}$$

$$\sigma^a_{\alpha\beta} = 2\eta'(\Omega_{\alpha\beta} - \omega_{\alpha\beta}) \quad, \tag{4.26}$$

$$M_{\alpha\beta\gamma} = \kappa_0\partial_\gamma\Omega_{\alpha\beta} + \zeta_2\Delta\mu_0\epsilon_{\alpha\beta\delta}p_\delta p_\gamma\delta(\mathbf{r}) \quad. \tag{4.27}$$

Using boundary condition of no flows at infinity the equations of motion read

$$2\eta\partial^2_\gamma v_\alpha = -\partial_\beta\partial_\gamma\left\{\zeta_2\Delta\mu_0\epsilon_{\alpha\beta\delta}p_\delta p_\gamma\delta(\mathbf{r})\right\} + \frac{\kappa_0}{2\eta'}(\eta + \eta')\partial^4_\gamma v_\alpha \tag{4.28}$$

$$0 = \kappa_0\partial^2_\gamma\Omega_{\alpha\beta} + \zeta_2\Delta\mu_0\partial_\gamma(\epsilon_{\alpha\beta\delta}p_\delta p_\gamma\delta(\mathbf{r})) - 4\eta'(\Omega_{\alpha\beta} - \omega_{\alpha\beta}) \quad. \tag{4.29}$$

The velocity field can be determined numerically by solving Eqns (5.4) and (5.5) using a periodic box and spatial Fourier transformations is displayed in Fig. 4.3 (a) and (b). The chiral rod motor induces a velocity field consisting of two opposing vortices in front and behind the motor. At the position $\mathbf{r} = 0$ the velocity field vanishes, implying

that the motor does not move. The far field can be obtained analytically and is given by

$$v_\alpha \simeq \frac{\zeta_2 \Delta\mu_0}{4\pi\eta} \frac{\mathbf{p} \cdot \mathbf{r}}{|\mathbf{r}|^5} \epsilon_{\alpha\beta\gamma} r_\beta p_\gamma \quad , \tag{4.30}$$

for $r \gg \ell$. This is the same as the far field of two counter-rotating spheres, separated along the vector $\mathbf{p}$ by a small distance.

The chiral rod motor generates an intrinsic rotation field $\Omega_{\alpha\beta}$. The far field of $\Omega_{\alpha\beta}$ is given by $\Omega_{\alpha\beta} = \omega_{\alpha\beta}$, where $\omega_{\alpha\beta}$ is the vorticity of the velocity field give in Eq. (4.30). Fig. 4.3 (c) and (d) displays $\Omega_{\alpha\beta} - \omega_{\alpha\beta}$ of the chiral rod. This difference is finite only in the near field.

4.2.3 Nematic chiral ring

The active angular momentum flux parametrized by the coefficient ζ_3 in Eq. (5.3) corresponds to the active chiral ring motor sketched in Fig. 4.1 (c). This term can be generated by a distribution of torque dipoles of type (i). Consider a distribution of the torque dipoles confined to the plane defined by its normal vector $\mathbf{p}$, such that $\mathbf{p} \cdot \mathbf{p}^{(i)} = 0$. The angular momentum flux (4.15) then becomes

$$M_{\alpha\beta\gamma}^{act}(\mathbf{r}) = \zeta_3 \Delta\mu(\mathbf{r})(\epsilon_{\alpha\delta\gamma} p_\delta p_\beta - \epsilon_{\beta\delta\gamma} p_\delta p_\alpha) \quad , \tag{4.31}$$

where $\zeta_3 \Delta\mu = qdn(\mathbf{r})$. The stresses and angular momentum fluxes induced by a single nematic ring motor in an otherwise passive Newtonian fluid are given by

$$\sigma_{\alpha\beta} = 2\eta u_{\alpha\beta} \quad , \tag{4.32}$$

$$\sigma_{\alpha\beta}^a = 2\eta'(\Omega_{\alpha\beta} - \omega_{\alpha\beta}) \quad , \tag{4.33}$$

$$M_{\alpha\beta\gamma} = \kappa\partial_\gamma\Omega_{\alpha\beta} + \zeta_3\Delta\mu_0(\epsilon_{\alpha\gamma\delta} p_\delta p_\beta - \epsilon_{\beta\gamma\delta} p_\delta p_\alpha)\delta(\mathbf{r}) \quad , \tag{4.34}$$

and the equations of motion read,

$$2\eta\partial_\gamma^2 v_\alpha = -\partial_\beta\partial_\gamma \{\zeta_3\Delta\mu_0\epsilon_{\alpha\beta\delta} p_\delta p_\gamma\delta(\mathbf{r})\} + \frac{\kappa_0}{2\eta'}(\eta + \eta')\partial_\gamma^4 v_\alpha \tag{4.35}$$

$$0 = \kappa_0\partial_\gamma^2\Omega_{\alpha\beta} + \zeta_3\Delta\mu_0\partial_\gamma(\epsilon_{\alpha\gamma\delta} p_\delta p_\beta - \epsilon_{\beta\gamma\delta} p_\delta p_\alpha)\delta(\mathbf{r})) - 4\eta'(\Omega_{\alpha\beta} - \omega_{\alpha\beta}) \tag{4.36}$$

Interestingly the active term ζ_3 enters the equation of motion for the velocity field Eq. (4.35) in exactly the same way ζ_2 entered Eq. (4.28). The velocity fields of the nematic ring is therefore exactly the same as the one generated by the nematic rod, see Fig 4.3 (a,b).

However, the intrinsic rotation rate generated by the nematic ring is different from the one of the chiral nematic rod. The far field of $\Omega_{\alpha\beta}$ is given by $\Omega_{\alpha\beta} = \omega_{\alpha\beta}$, where $\omega_{\alpha\beta}$ is the vorticity of the velocity field give in Eq. (4.30). Fig. 4.3 (e,f) displays $\Omega_{\alpha\beta} - \omega_{\alpha\beta}$. This difference is finite only in the near field.
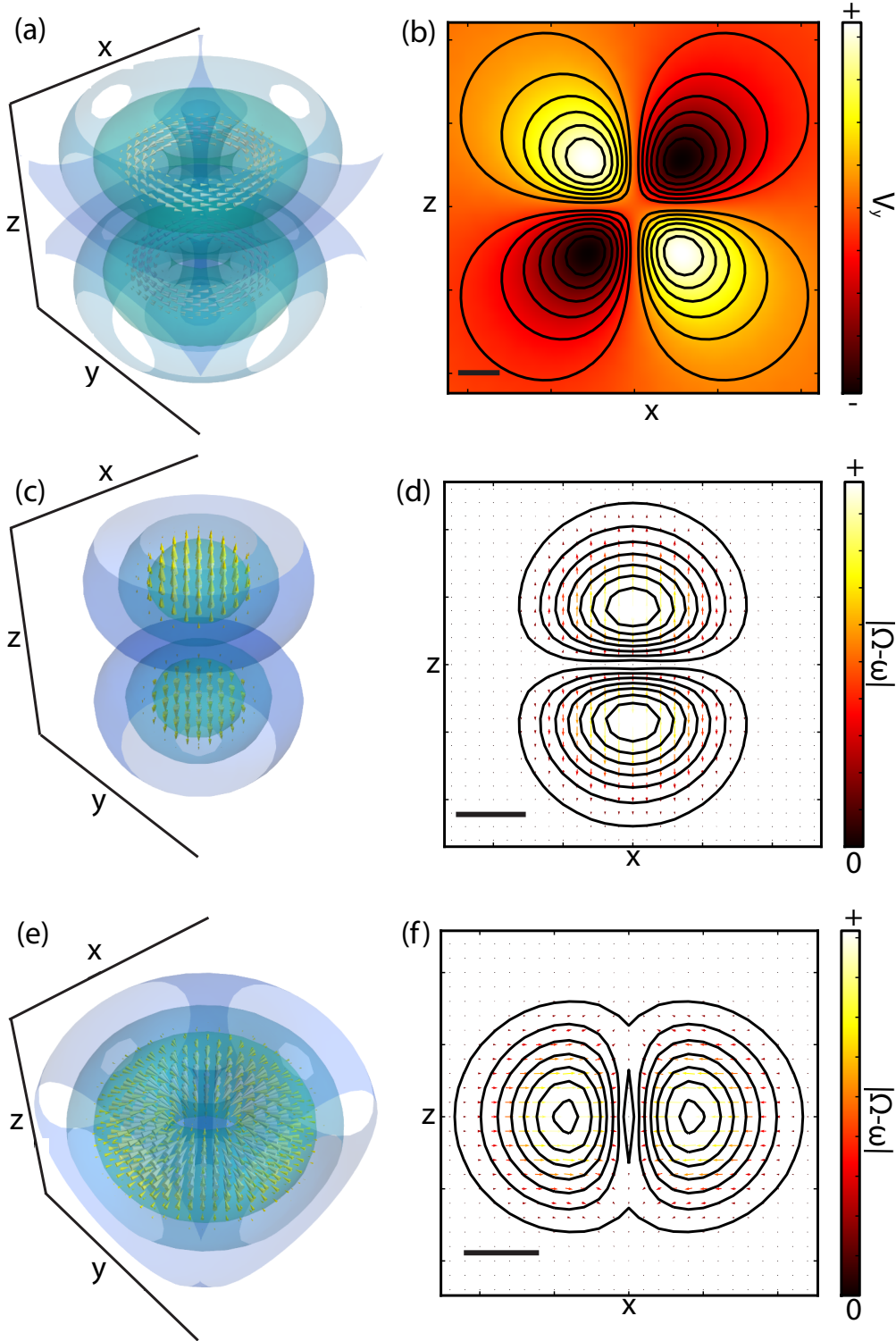
Figure 4.3: Flow $\mathbf{v}$ and rotation field $\mathbf{\Omega} - \omega$ of the nematic elementary motors (Fig. 4.1 (b) and (c)). Both elementary motors share the same velocity $\mathbf{v}$ shown in (a) and (b). Velocity vectors as well as surfaces of constant $|\mathbf{v}|$ are indicated in (a). The flow in the xz-plane for $y = 0$ is shown in (b). The rotation fields differ for both elementary motors. The rotation field of the chiral rod is shown in (c) and (d). The rotation field of the chiral ring is shown in (e) and (f). The rotation vectors $\mathbf{\Omega} - \omega$ are indicated as cones and surfaces of constant magnitude are indicated in (c) and (e). Cross sections in the xz-plane at $y = 0$ are shown in (d) and (f). The black scale bar indicates the length ℓ. The parameters are $\eta/\eta' = 1$. The size of the periodic box is 26ℓ.

4.2.4 Polar chiral motor

The antisymmetric stress parametrized by the coefficient $\tilde{\zeta}$ corresponds to the polar chiral elementary motor, see Fig 4.1 (e). It is generated by a distributions of dipoles of type (iii), see Fig 4.1 (iii).

A distribution of dipoles of type (iii) that the vector $\mathbf{p}^{(i)} \times \varphi$ is parallel to a unit vector $\mathbf{p}$ generates an active antisymmetric stress

$$\sigma_{\alpha\beta}^{a,act} = \tilde{\zeta}\Delta\mu\epsilon_{\alpha\beta\gamma}p_\gamma \quad , \tag{4.37}$$

where $\tilde{\zeta}\Delta\mu = n(\mathbf{r})/2$. The stresses and angular momentum fluxes induced by a single polar chiral motor in an otherwise passive Newtonian fluid are given by

$$\sigma_{\alpha\beta} = 2\eta u_{\alpha\beta} \quad , \tag{4.38}$$

$$\sigma_{\alpha\beta}^a = 2\eta'(\Omega_{\alpha\beta} - \omega_{\alpha\beta}) + \tilde{\zeta}\Delta\mu_0\epsilon_{\alpha\beta\gamma}p_\gamma\delta(\mathbf{r}) \quad , \tag{4.39}$$

$$M_{\alpha\beta\gamma} = \kappa\partial_\gamma\Omega_{\alpha\beta} \quad . \tag{4.40}$$

The equations of motion therefore read,

$$2\eta\partial_\gamma^2 v_\alpha = \frac{\kappa_0}{2\eta'}\left((\eta + \eta')\partial_\gamma^4 v_\alpha + \tilde{\zeta}\Delta\mu_0\epsilon_{\alpha\beta\gamma}p_\gamma\partial_\delta^2\partial_\beta\delta(\mathbf{r})\right) \quad , \tag{4.41}$$

$$0 = \kappa_0\partial_\gamma^2\Omega_{\alpha\beta} - 4\eta'(\Omega_{\alpha\beta} - \omega_{\alpha\beta}) - 2\tilde{\zeta}\Delta\mu_0\epsilon_{\alpha\beta\gamma}p_\gamma\delta(\mathbf{r}) \quad . \tag{4.42}$$

Integrating Eq. (4.41) for no flows at infinity yields

$$v_\alpha - \frac{\kappa_0}{4\Phi}\partial_\gamma^2 v_\alpha = \frac{\tilde{\zeta}\Delta\mu_0}{2\eta}\epsilon_{\alpha\beta\gamma}p_\gamma\partial_\beta\delta(\mathbf{r}) \quad , \tag{4.43}$$

where $\Phi = \eta\eta'/(\eta + \eta')$ is the harmonic mean of the viscosity and the rotational viscosity. We find the velocity field

$$v_\alpha = -\frac{\tilde{\zeta}\Delta\mu_0}{2\pi\eta}\frac{\Phi}{\kappa_0}\left(\frac{1}{r^3} + \frac{\Phi}{\kappa_0}\frac{1}{r^2}\right)e^{-|r|/\ell}\epsilon_{\alpha\beta\gamma}p_\gamma r_\beta \quad . \tag{4.44}$$

We also determine it numerically, see Fig 4.4 (a,b). The polar motor generates an intrinsic rotation field

$$\Omega_{\alpha\beta} = \frac{\tilde{\zeta}\Delta\mu_0}{2\pi\kappa_0|\mathbf{r}|}\epsilon_{\alpha\beta\gamma}p_\gamma e^{-2|\mathbf{r}|/\ell} - \frac{4}{\ell^2}\int e^{-2|\mathbf{r}-\mathbf{r}'|/\ell}\frac{\omega_{\alpha\beta}}{|\mathbf{r} - \mathbf{r}'|}d\mathbf{r}' \quad . \tag{4.45}$$

The velocity field $\mathbf{v}$ and the intrinsic rotation rate $\Omega_{\alpha\beta}$ both decay on the length scale ℓ, see (4.43) and (4.45). Therefore the polar chiral motor has no farfield. Note that $\Omega_{\alpha\beta} = \omega_{\alpha\beta} = 0$ for $r \gg \ell$. Interestingly, $\Omega_{\alpha\beta} \neq \omega_{\alpha\beta}$ in the near field for $r \ll \ell$, i.e. the rate of intrinsic rotation differs from the vorticity of the flow, see Fig 4.4 (c,d).

Figure 4.4: Polar chiral motor: Velocity fields (a,b) and difference of intrinsic rotation rate and vorticity (c,d) in 3d (a,c) and as a cut through the xz plane (b,d). Cones and arrows represent $\epsilon_{\alpha\beta\gamma}(\Omega_{\beta\gamma} - \omega_{\beta\gamma})$ in (a,c) and (b,d), respectively. Surfaces (a,c) and lines (b,d) represent equal magnitudes. The black scale-bar indicates the length ℓ. The parameters are $\eta/\eta' = 1$. The size of the periodic box is 26ℓ.

4.2.5 Polar ring

The angular momentum flux parametrized by the coefficient ζ_4 in Eq. (5.3) corresponds to the active polar ring motor sketched in Fig 4.1 (d). Unlike the other elementary motors we discussed this motor is not chiral. It is however generated by chiral processes on the microscopic scale. Consider an ensemble of torque dipoles of type (ii) that are distributed such that on average all $\mathbf{t} \cdot \mathbf{p} = 0$ and $\mathbf{p}^{(i)} \cdot \mathbf{p} = 0$, where the vector $\mathbf{p}$ is a macroscopic polarity vector. The angular momentum flux this distribution of dipoles generates is given by

$$M_{\alpha\beta\gamma}^{act} = \zeta_4 \Delta\mu \left(\delta_{\alpha\gamma} p_\beta - \delta_{\beta\gamma} p_\alpha \right) \quad , \tag{4.46}$$

with $\zeta_4 \Delta\mu = qdn(\mathbf{r})/2$. The stresses and angular momentum fluxes induced by a localized patch of polar ring motors in an otherwise passive Newtonian fluid are then given by

$$\sigma_{\alpha\beta} = 2\eta u_{\alpha\beta} \quad , \tag{4.47}$$

$$\sigma_{\alpha\beta}^a = 2\eta'(\Omega_{\alpha\beta} - \omega_{\alpha\beta}) \quad , \tag{4.48}$$

$$M_{\alpha\beta\gamma} = \kappa_0 \partial_\gamma \Omega_{\alpha\beta} + \zeta_4 \Delta\mu_0 \left(\delta_{\alpha\gamma} p_\beta - \delta_{\beta\gamma} p_\alpha \right) \delta(\mathbf{r}) \quad . \tag{4.49}$$

The equations of motion therefore read,

$$2\eta \partial_\gamma^2 v_\alpha = -\zeta_4 \Delta\mu_0 \left\{ \partial_\alpha \partial_\beta (\delta(\mathbf{r}) p_\beta) - \partial_\gamma^2 (\delta(\mathbf{r}) p_\alpha) \right\} + \frac{\kappa_0}{2\eta'}(\eta + \eta') \partial_\gamma^4 v_\alpha \quad , \tag{4.50}$$

$$0 = \kappa_0 \partial_\gamma^2 \Omega_{\alpha\beta} + \zeta_4 \Delta\mu_0 \partial_\gamma \left(\delta(\mathbf{r})(\delta_{\alpha\gamma} p_\beta - \delta_{\beta\gamma} p_\alpha) \right) - 4\eta'(\Omega_{\alpha\beta} - \omega_{\alpha\beta}) \quad . \tag{4.51}$$

We determine the velocity field and the intrinsic rotation field of the polar ring motor numerically. The velocity field is displayed in Fig. 4.5 (a,b). The motor generates a velocity field $\mathbf{v}$ that does not vanish in the limit of small r. This implies that the polar ring motor is a swimmer that propels itself in the direction set by the vector $\mathbf{p}$. The polar ring motor generates a velocity far field in the limit $\ell \to 0$ that can be determined analytically,

$$v_\alpha \simeq \frac{\zeta_4 \Delta\mu_0}{8\pi\eta} \left(\frac{3r_\alpha}{|\mathbf{r}|^5} \mathbf{r} \cdot \mathbf{p} - p_\alpha \frac{1}{|\mathbf{r}|^3} \right) \quad . \tag{4.52}$$

The polar ring motor also generates intrinsic rotations. The field of intrinsic rotations $\Omega_{\alpha\beta} \neq \omega_{\alpha\beta}$ in the near field $r \ll \ell$ and becomes equal to the vorticity in the far-field, $r \gg \ell$, see Fig. 4.5 (c,d).

4.3 Summary

We have shown that the active terms in the constitutive equations (2.67)-(2.71) correspond to distributions of chiral torque and force dipoles on the molecular scale in the fluid. We listed the different types of chiral force and torque dipoles that can be constructed.

We identified five types of elementary chiral motors, that correspond to localized distributions of torque and force dipoles in the fluid. Four of these elementary motors
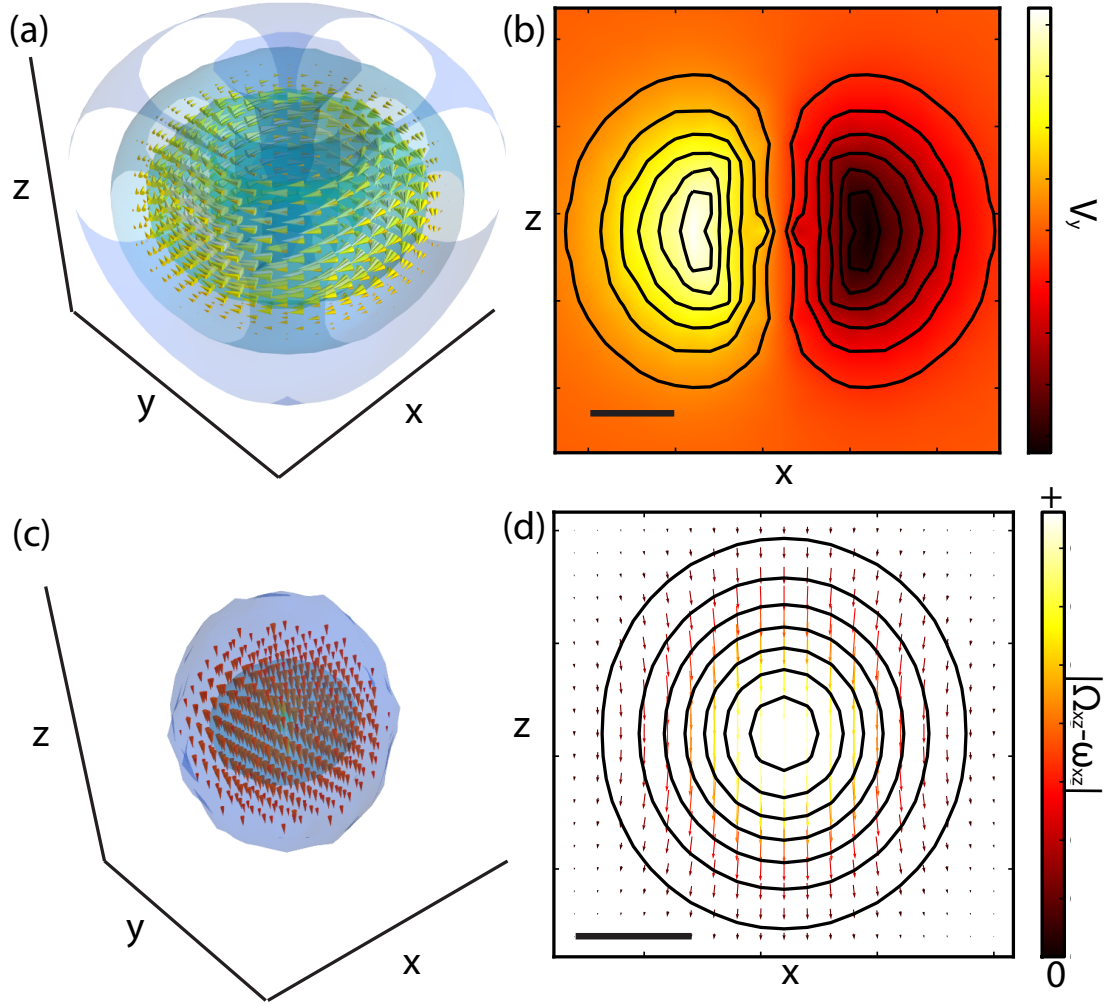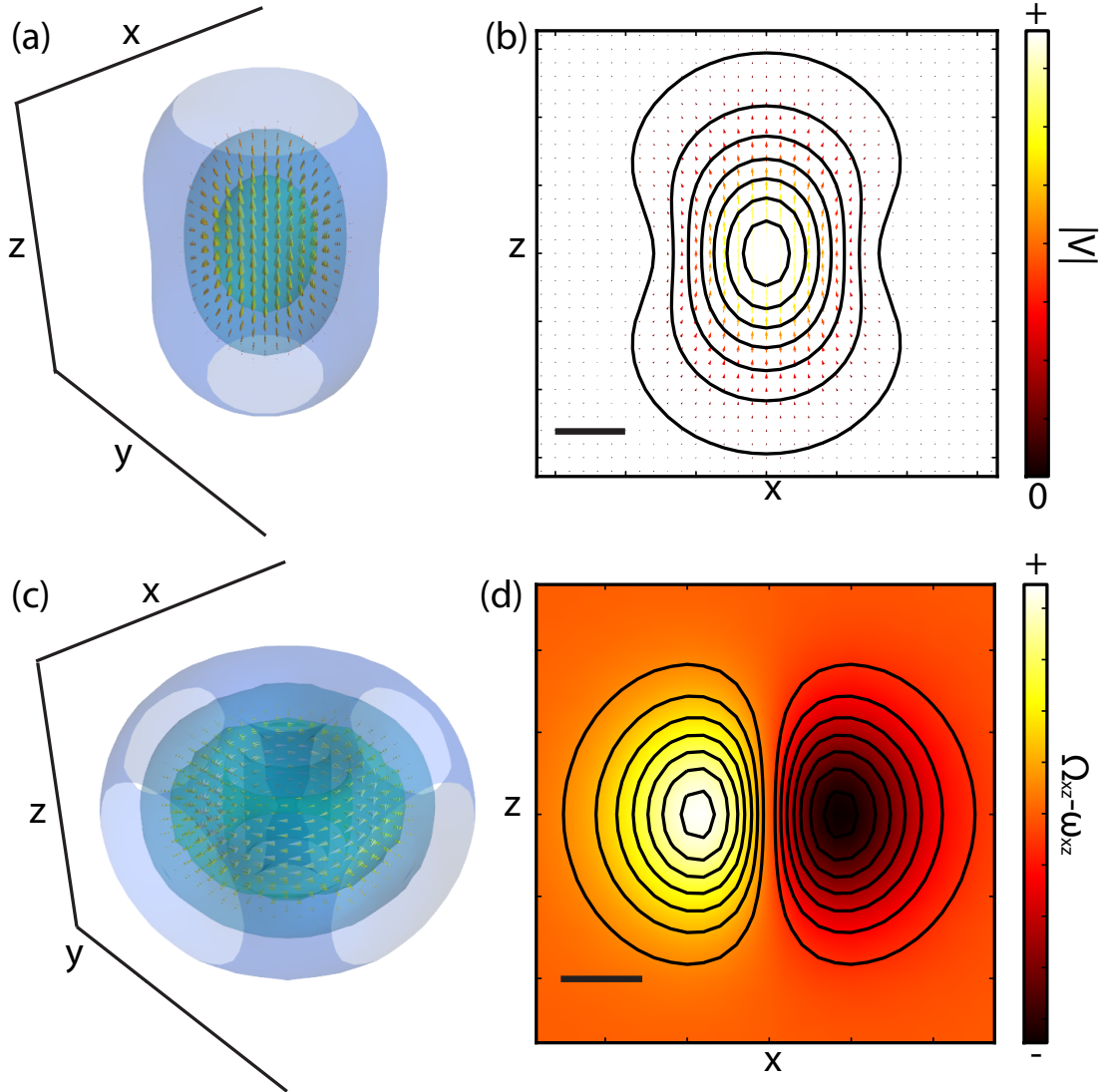
Figure 4.5: Polar chiral motor: Velocity fields (a,b) and difference of intrinsic rotation rate and vorticity (c,d) in 3d (a,c) and as a cut through the xz plane (b,d). Cones and arrows represent $\epsilon_{\alpha\beta\gamma}(\Omega_{\beta\gamma} - \omega_{\beta\gamma})$ in (a,c) and (b,d), respectively. Surfaces (a,c) and lines (b,d) represent equal magnitudes. The black scale-bar indicates the length ℓ. The parameters are $\eta/\eta' = 1$. The size of the periodic box is 26ℓ.

are chiral, one is not, although it is generated by microscopically chiral objects. The five elementary chiral motors we identify are (a) isotropic chiral motors; (b) chiral rods; (c) chiral rings ; (d) the polar ring and (e) polar chiral motors and differ by their symmetries.

Isotropic motors generate a field of local intrinsic rotations but no flow field. This rotation field decays on the length scale ℓ.

Chiral rods and rings both have nematic symmetry. They generate the same hydrodynamic far field with a velocity that decays as $v \sim |\mathbf{r}|^{-3}$. The intrinsic rotation fields differ at short distances but become both equal to the vorticity of v in the far field.

The polar chiral motor does not generate a hydrodynamic far field but both a flow and a intrinsic rotation field at short distances.

We also show that the polar ring motor (d) that is not chiral. The polar ring motor is a swimmer since the velocity field at the position of the swimmer is non-vanishing. The polar ring generates a hydrodynamic far field.

Chapter 5

Active chiral films

Active chiral processes are typically observed on surfaces or at interfaces. Key examples are carpets of beating cilia driving hydrodynamic flows parallel to the surface on which they are attached [13, 14] and rotating motors on a surface [75, 76, 102].

In the present chapter we discuss the interesting interactions of chiral motors and surfaces. We first discuss an example where an active chiral fluid confined between two surfaces gives rise to large scale chiral flows via a chiral boundary layer. To generalize this result, we develop theory for a thin films of fluid with chiral motors. Most results of the present chapter have been obtained in close collaboration with the diploma student Maria Strempel, and have been published here [103].

5.1 An active chiral fluid between two plates

To highlight the interesting rheological properties that can emerge in an active chiral fluids close to a surface, we now consider an active chiral fluid confined between two solid surfaces in the xy plane at distance d, see Fig. 5.1 (a). We choose no-slip boundary conditions on both surfaces. Furthermore we impose vanishing rotation field, $\Omega_{\alpha\beta} = 0$ on both surfaces. We assume the lower surface at $z = 0$ to be immobile, $\mathbf{v}(z = 0) = 0$. The upper surface moves at velocity Δv in y direction, $\mathbf{v}(z = d) = \Delta v \hat{\mathbf{e}}_y$. We choose the direction of the polarity $\mathbf{p}$ on both surfaces to point parallel to the surface in x-direction. The polarity field is governed by a free energy functional that is minimized if the polarity $\mathbf{p}$ is locally aligned and we impose the constraint $|\mathbf{p}| = 1$. The constitutive equations of the gel are

$$
\begin{aligned}
\sigma_{\alpha\beta} &= 2\eta u_{\alpha\beta} \quad, & (5.1) \\
\sigma_{\alpha\beta}^a &= 2\eta' \left(\Omega_{\alpha\beta} - \omega_{\alpha\beta}\right) + \tilde{\zeta}\Delta\mu\epsilon_{\alpha\beta\gamma}p_\gamma \quad, & (5.2) \\
M_{\alpha\beta\gamma} &= \kappa_0\partial_\gamma\Omega_{\alpha\beta} + \zeta_1\epsilon_{\alpha\beta\gamma}\Delta\mu + \zeta_2\Delta\mu\epsilon_{\alpha\beta\delta}p_\delta p_\gamma \\
&\quad + \zeta_3\Delta\mu(\epsilon_{\alpha\gamma\delta}p_\delta p_\beta - \epsilon_{\beta\gamma\delta}p_\delta p_\alpha) + \zeta_4\Delta\mu(\delta_{\alpha\gamma}p_\beta - \delta_{\beta\gamma}p_\beta) \quad. & (5.3)
\end{aligned}
$$

In the low Reynolds number limit where inertial terms can be neglected, the dynamic equations read

$$(\eta + \eta')\partial_\gamma^2 v_\alpha + 2\eta'\partial_\beta\Omega_{\alpha\beta} + \tilde{\zeta}\partial_\beta(\Delta\mu\epsilon_{\alpha\beta\gamma}p_\gamma) = \partial_\alpha\bar{P} \quad , \tag{5.4}$$

$$\kappa_0\partial_\gamma^2\Omega_{\alpha\beta} + \zeta_1\epsilon_{\alpha\beta\gamma}\partial_\gamma\Delta\mu + \zeta_2\partial_\gamma(\epsilon_{\alpha\beta\delta}p_\delta p_\gamma\Delta\mu) + \zeta_3\partial_\gamma\left(\Delta\mu(\epsilon_{\alpha\gamma\delta}p_\delta p_\beta - \epsilon_{\beta\gamma\delta}p_\delta p_\alpha)\right)$$

$$+ \quad \zeta_4\partial_\gamma\left(\Delta\mu(\delta_{\alpha\gamma}p_\beta - \delta_{\beta\gamma}p_\alpha)\right) - 4\eta'(\Omega_{\alpha\beta} - \omega_{\alpha\beta}) - 2\tilde{\zeta}\epsilon_{\alpha\beta\gamma}p_\gamma\Delta\mu = 0 \quad . \tag{5.5}$$

Here, the hydrostatic pressure $\bar{P}$ plays the role of a Lagrange multiplier. Taking the divergence of Eq. (5.4) we find $\partial_\gamma^2\bar{P} = 0$. Therefore the pressure $\bar{P} = const$ if no external pressure gradients are applied. From equations (5.4) and (5.5) we obtain a differential equation for the flow field,

$$2\eta\partial_\gamma^2 v_\alpha = -\partial_\beta\partial_\gamma\left\{(\zeta_2 + \zeta_3)\epsilon_{\alpha\beta\delta}p_\delta p_\gamma\Delta\mu\right\} - \zeta_4\left\{\partial_\alpha\partial_\beta(\Delta\mu p_\beta) - \partial_\gamma^2(\Delta\mu p_\alpha)\right\}$$

$$+ \quad \frac{\kappa_0}{2\eta'}\left((\eta + \eta')\partial_\gamma^4 v_\alpha + \tilde{\zeta}\epsilon_{\alpha\beta\gamma}p_\gamma\partial_\delta^2\partial_\beta\Delta\mu\right) \quad . \tag{5.6}$$

We first assume $\mathbf{p} = \hat{\mathbf{e}}_x$ also in the volume. Using Eqns. (5.4) and (5.5) we then find $\Omega_{xz} = \Omega_{xy} = 0$ and $v_x = v_z = 0$. The velocity v_y and the intrinsic rotation rate Ω_{yz} obey

$$(\eta + \eta')\partial_z^2 v_y + 2\eta'\partial_z\Omega_{yz} = 0 \quad , \tag{5.7}$$

$$(\kappa_0\partial_z^2 - 4\eta')\Omega_{yz} - 2\eta'\partial_z v_y - 2\tilde{\zeta}\Delta\mu = 0 \quad . \tag{5.8}$$

The dynamics of the polarity $\mathbf{p}$ is given by

$$\partial_t p_\alpha = \frac{1}{\gamma}h_\alpha^{tot} - v_\gamma\partial_\gamma p_\alpha - \Omega_{\alpha\beta}p_\beta \quad . \tag{5.9}$$

For constant $\mathbf{p} = \hat{\mathbf{e}}_x$, $\mathbf{h}^{tot} = 0$ and thus $\mathbf{p}$ is stationary. The active fluid exerts a wall shear stress,

$$\sigma_{yz}^{tot}|_{z=d} = \left\{(\eta + \eta')\partial_z v_y + \tilde{\zeta}\Delta\mu\right\}|_{z=d} \tag{5.10}$$

Fig. 5.1 (b) shows the profiles of velocity v_y and intrinsic rotation rate Ω_{zy} obtained by numerical solution of Eqns (5.4) and (5.5) as a function of z/d for two immobile plates, $\Delta v = 0$.

For the boundary condition $\sigma_{yz}^{tot}|_{z=d} = 0$, i.e. no shear stress between the plates, the plates move relative to each other, i.e. $\Delta v \neq 0$. The flow profile for this boundary condition is displayed in Fig. 5.1 (d). The system acts as a motor because Δv depends linearly on the shear stress imposed. The resulting stress-velocity relationships for different values of $\tilde{\zeta}\Delta\mu$ are displayed in Fig. 5.1 (b). Note that it is polar chiral term $\tilde{\zeta}$ that generates this relative motion of the plates. Interestingly even though an individual polar chiral motor does not generate a far field (see section 4.2.4), homogeneous distributions of such motors create relative flows at large separation. These flows are created in a thin boundary layer. The stress between the plates does not depend on d for $\ell \ll d$.

This example shows that interesting physical effects can appear in an active chiral fluid close to a surface by an active chiral boundary layer.
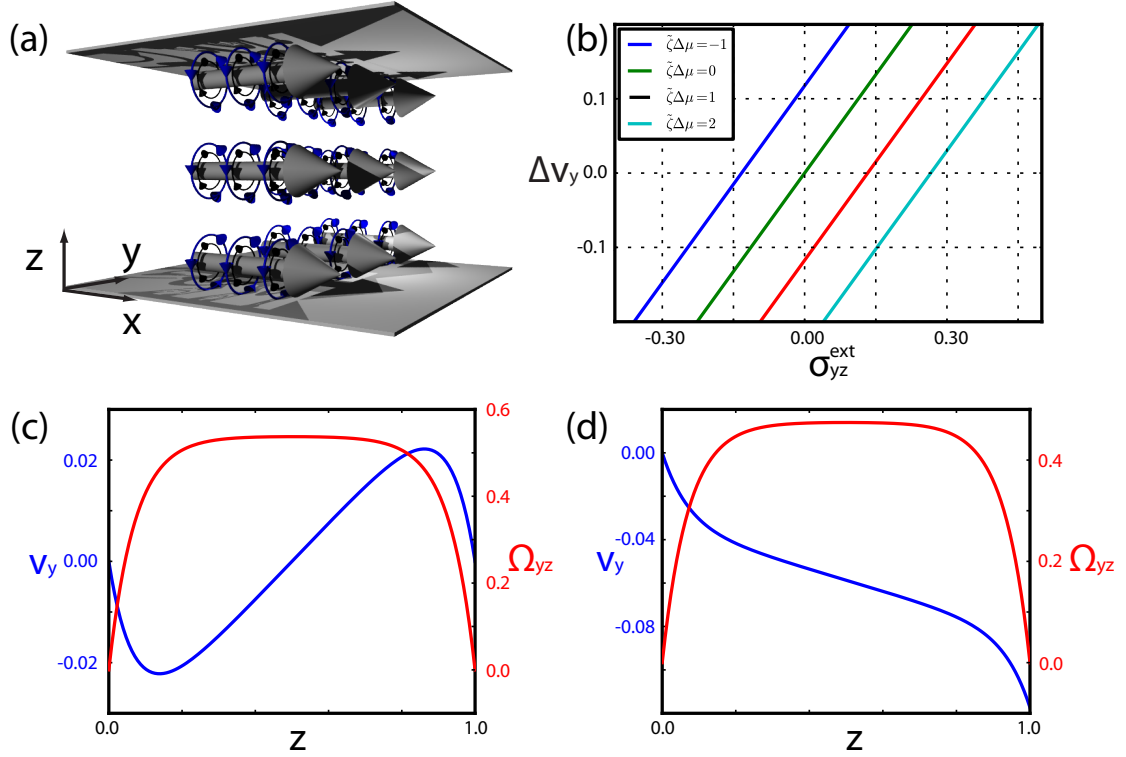
Figure 5.1: Chiral shear flows generated by active chiral processes with a constant polarity vector, enclosed between two surfaces of distance d. (a) Schematic representation of the system. (b) Velocity difference Δv_y between upper and lower plate as a function of external shear stress σ_{zy}^{ext}, applied to the surfaces for difference values of the parameter $\tilde{\zeta}\Delta\mu$. (c) Profile of velocity v_y and rotation rate Ω_{yz} as function of position z between the plates for fixed plates, $\Delta\mathbf{v} = 0$. (d) Profile of velocity v_y and rotation rate Ω_{yz} as function of position z between the plates for $\sigma_{zy}^{ext} = 0$. Parameter values are $\tilde{\zeta}\Delta\mu = 1$, $\eta/\eta' = 1$ and $\ell/d = 0.1$.

5.2　　Generic theory for thin active films

We now develop a generic theory for thin films of active fluids with chiral motors. In contrast to the example in the previous section we want to treat the boundary conditions on the film in a generalized way, describing them by a small set of phenomenological coefficients. We achieve this, by integrating the force and torque balance equations over the thickness of thin film. We express the boundary terms, which describe the interaction of the thin film with the surfaces, by writing all terms allowed by symmetry. The price we pay, is that we no longer resolve the internal structure of the film explicitly.

5.2.1　　Properties of the thin film

A thin film is a layer of fluid whose thin dimension h is much smaller than its extension L in the other two directions. In the following we will constrain ourselves to planar geometries and choose the thin dimension in Cartesian coordinates to be the z-direction for simplicity, see Fig. 5.2. However, all arguments that follow can be generalized to curved spaces. The thin film is constituted of a gel with the constitutive equations

$$
\begin{aligned}
\sigma_{\alpha\beta} &= 2\eta u_{\alpha\beta} + \bar{\zeta}\Delta\mu\delta_{ij} + \zeta' r\Delta\mu p_i p_j \quad, & (5.11)\\
\sigma_{\alpha\beta}^a &= 2\eta'\left(\Omega_{\alpha\beta} - \omega_{\alpha\beta}\right) + \tilde{\zeta}\Delta\mu\epsilon_{\alpha\beta\gamma}p_\gamma \quad, & (5.12)\\
M_{\alpha\beta\gamma} &= \kappa_0\partial_\gamma\Omega_{\alpha\beta} + \zeta_1\epsilon_{\alpha\beta\gamma}\Delta\mu + \zeta_2\Delta\mu\epsilon_{\alpha\beta\delta}p_\delta p_\gamma \\
&\quad + \zeta_3\Delta\mu(\epsilon_{\alpha\gamma\delta}p_\delta p_\beta - \epsilon_{\beta\gamma\delta}p_\delta p_\alpha) + \zeta_4\Delta\mu(\delta_{\alpha\gamma}p_\beta - \delta_{\beta\gamma}p_\beta) \quad. & (5.13)
\end{aligned}
$$

The thin film is a quasi-2D structure, and its dynamics can be described in terms of averages over the thickness of the film. In the case of the fluids we are interested in these quantities are the averaged velocity

$$
\bar{\mathbf{v}} = \frac{1}{h}\int_0^h \mathbf{v}\,dz \quad, \tag{5.14}
$$

and the averaged intrinsic rotation rate

$$
\bar{\Omega}_{\alpha\beta} = \frac{1}{h}\int_0^h \Omega_{\alpha\beta}\,dz \quad. \tag{5.15}
$$

Here and in the following bars denote averages over the film thickness. To obtain equations of motion for these averaged quantities, we discuss the force and the torque balance in thin films.
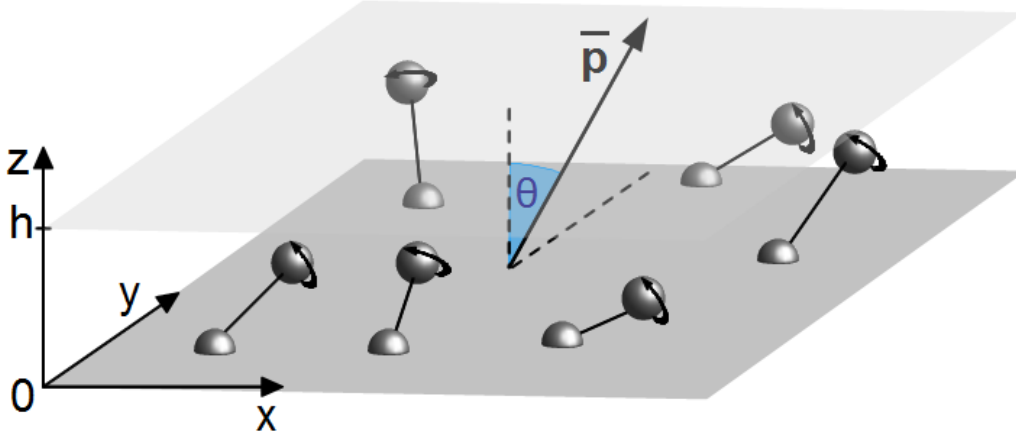
Figure 5.2: Schematics of a thin fluid film of height h that contains chiral motors. Motors are torque dipoles that consist of counter-rotating spheres, one of which is attached to the surface. The other rotates as indicated by the arrows. The average motor direction is described by the vector $\bar{\mathbf{p}}$ which is tilted at an angle θ in y-direction.

5.2.2   Force balance of the thin film

We obtain the force balance equation for a thin film by integrating Eq. (2.11) over the thickness h of the film,

$$0 = \frac{1}{h} \int_0^h \mathrm{d}z \partial_\beta \sigma_{i\beta}^{tot} = \partial_j \bar{\sigma}_{ij}^{tot} + \frac{1}{h} \sigma_{iz}^{tot}\big|_0^h \quad , \tag{5.16}$$

and

$$0 = \frac{1}{h} \int_0^h \mathrm{d}z \partial_\beta \sigma_{z\beta}^{tot} = \partial_j \bar{\sigma}_{zj}^{tot} + \frac{1}{h} \sigma_{zz}^{tot}\big|_0^h \quad . \tag{5.17}$$

Here and in the following roman indices denote the in-film directions x and y, while greek indices denote all three spacial directions. For boundary terms we adopt the notation,

$$\sigma_{iz}^{tot}\big|_0^h \equiv \sigma_{iz}^{tot}(z = h) - \sigma_{iz}^{tot}(z = 0) \quad . \tag{5.18}$$

The 2D force balance equations (5.16) and (5.17) consist of two parts each: (i) an in film flux; (ii) a boundary term that summarizes the interactions between the thin film and its support.

We now discuss Eq. (5.16) which is the force balance in the in-film directions . The flux term of Eq. (5.16) depends on the film tension $\bar{\sigma}_{ij}^{tot}$. An expression for the tension can be obtained by averaging the bulk constitutive Eqns. (5.11) and (5.12). We find

$$\bar{\sigma}_{ij}^{tot} = 2\eta \bar{u}_{ij} + 2\eta' \bar{\Omega}_{ij} - 2\eta' \bar{\omega}_{ij} + \bar{\zeta} \bar{\Delta}\mu \delta_{ij} + \zeta' \bar{\Delta}\mu p_i p_j + \tilde{\zeta} \bar{\Delta}\mu \epsilon_{ijz} p_z - \delta_{ij} \bar{P} \quad . \tag{5.19}$$

For simplicity we have assumed that the vector **p** is constant over the thickness the film. Releasing this constraint changes the relative magnitude of the different active stresses but does not create new terms. The hydrostatic tension in the film $\bar{P}$ can be found by considering that

$$\bar{\sigma}_{zz}^{tot} = -2\eta\partial_i\bar{v}_i + \zeta\bar{\Delta\mu} + \zeta'\bar{\Delta\mu}p_zp_z - \bar{P} = -P^{ext} \quad . \tag{5.20}$$

Here we used the incompressibility condition and P^{ext} is the external pressure. Inserting Eq. (5.20) in Eq. (5.19) we find

$$\begin{aligned}
\bar{\sigma}_{ij}^{tot} &= 2\eta(\bar{u}_{ij} + \partial_k\bar{v}_k\delta_{ij}) + 2\eta'\bar{\Omega}_{ij} - 2\eta'\bar{\omega}_{ij} + \zeta'\bar{\Delta\mu}(p_ip_j - p_z^2\delta_{ij}) \\
&+ \tilde{\zeta}\bar{\Delta\mu}\epsilon_{ijz}p_z - \delta_{ij}P^{ext} \quad .
\end{aligned} \tag{5.21}$$

The boundary term of Eq. (5.16) $\frac{1}{h}\sigma_{iz}^{tot}|_0^h$ expresses the friction forces between the film and its support. From the constitutive equations we find,

$$\begin{aligned}
\frac{1}{h}\sigma_{iz}^{tot}|_0^h &= \frac{1}{h}\left[2\eta u_{iz} + 2\eta'\Omega_{iz} - 2\eta'\omega_{iz} + \zeta'\bar{\Delta\mu}p_ip_z\right]_0^h \\
&\simeq \xi_f\bar{v}_i - \xi_\Omega\bar{\Omega}_{iz} + \zeta_{\text{glide}}\bar{\Delta\mu}p_i.
\end{aligned} \tag{5.22}$$

In Eq. (5.22) we introduced the coefficient ξ_f that describes friction forces due to the center mass flows of the thin film with respect to the substrate. The coefficient ξ_Ω parametrizes forces produced by intrinsic rotations. The active coefficient ζ_{glide} parametrizes the effects of motors pulling on the surface along the polarity vector **p**, and might be relevant to the description of gliding essays [112].

5.2.3   Torque balance of the thin film

Following the same procedure as for the force balance, we now obtain a 2D torque balance by averaging Eq. (2.22) over the thickness of the film,

$$0 = -2\bar{\sigma}_{ij}^a + \partial_k\bar{M}_{ijk} + \frac{1}{h}M_{ijz}|_0^h \tag{5.23}$$

$$0 = -2\bar{\sigma}_{iz}^a + \partial_k\bar{M}_{izk} + \frac{1}{h}M_{izz}|_0^h \quad . \tag{5.24}$$

Eqns. (5.23) and (5.24) both consist of (i) a flux in the film $\bar{M}_{\alpha\beta k}$, (ii) a boundary term $\frac{1}{h}M_{\alpha\beta z}|_0^h$ that describes frictional torques at between the film and its support and (iii) a source term $\bar{\sigma}_{\alpha\beta}^a$ that describes the conversion of orbital to spin angular momentum in the film. We start by discussing Eq. (5.23). The flux term in Eq. (5.23) can be obtained from the constitutive equations and reads,

$$\begin{aligned}
\bar{M}_{ijk} &= \kappa\partial_k\bar{\Omega}_{ij} + \zeta_2\bar{\Delta\mu}\epsilon_{ijz}p_zp_k \\
&+\zeta_3\bar{\Delta\mu}\left(\epsilon_{ikz}p_zp_j - \epsilon_{jkz}p_zp_i\right) + \zeta_4\bar{\Delta\mu}\left(\delta_{ik}p_kp_j - \delta_{jk}p_kp_i\right) \quad . \tag{5.25}
\end{aligned}$$

The source term in Eq. (5.23) is can be obtained by averaging Eq. (5.12) over the thickness of the film and reads

$$\bar{\sigma}_{ij}^a = 2\eta'(\bar{\Omega}_{ij} - \bar{\omega}_{ij}) + \tilde{\zeta}\bar{\Delta\mu}\epsilon_{ijz}p_z \quad . \tag{5.26}$$

Like in the case of the torque balance, we assume that **p** is constant over the thickness of the film for simplicity. The boundary term of Eq. (5.23) is

$$
\begin{aligned}
\frac{1}{h} M_{ijz}|_0^h &= \frac{1}{h} \left[\kappa \partial_z \Omega_{ij} + \zeta_1 \Delta\mu \epsilon_{ijz} + \zeta_2 \Delta\mu \epsilon_{ijz} p_z p_z + \zeta_3 \Delta\mu (\epsilon_{izk} p_k p_j - \epsilon_{jzk} p_k p_i) \right] \\
&\simeq \xi_r \Omega_{ij} + \bar{\zeta}_1 \bar{\Delta}\mu \epsilon_{ijz} + \bar{\zeta}_2 \bar{\Delta}\mu \epsilon_{ijz} p_z p_z + \bar{\zeta}_3 \bar{\Delta}\mu (\epsilon_{izk} p_k p_j - \epsilon_{jzk} p_k p_i) \quad , (5.27)
\end{aligned}
$$

where we introduced the rotational friction with the surface ξ_r and the active coefficients $\bar{\zeta}_1$, $\bar{\zeta}_2$ and $\bar{\zeta}_3$ that parametrize active angular momentum exchanging processes angular momentum between the surface and the film.

We now discuss the iz direction of the torque balance Eq. (5.24). The source term reads

$$
\bar{\sigma}_{iz}^a = 2\eta_l (\bar{\Omega}_{iz} - \bar{\omega}_{iz}) + \tilde{\zeta} \bar{\Delta}\mu \epsilon_{izj} p_j \quad . \tag{5.28}
$$

To obtain an expression for the averaged vorticity $\bar{\omega}_{iz} = \left(\partial_i \bar{v}_z - \bar{v}_i|_0^h / h \right) / 2 \simeq -\bar{v}_i|_0^h/(2h)$, we use $\partial_i v_z \ll \partial_z v_i$, valid in thin films. Also, since in thin films the shear stress is approximately constant throughout

$$
\sigma_{iz}^{ext} \simeq \bar{\sigma}_{iz} = \frac{1}{h}(\eta + \eta') v_i|_0^h + 2\eta' \Omega_{iz} + \zeta' \bar{\Delta}\mu p_i p_z + \tilde{\zeta} \bar{\Delta}\mu \epsilon_{izj} p_j \quad , \tag{5.29}
$$

and we find the expression

$$
\frac{1}{h} v_i|_0^h = -\frac{1}{(\eta + \eta')} \left(2\eta' \Omega_{iz} + \zeta' \bar{\Delta}\mu p_i p_z + \tilde{\zeta} \bar{\Delta}\mu \epsilon_{izj} p_j - \sigma_{iz}^{ext} \right) \quad , \tag{5.30}
$$

which in turn allows us to determine the averaged vorticity in the film. Thus, in the absence of external shear stresses, i.e. $\sigma_{ij}^{ext} = 0$,

$$
\bar{\sigma}_{iz}^a = \left(1 - \frac{\eta'}{\eta + \eta'} \right) \left(2\eta_l \bar{\Omega}_{iz} + \tilde{\zeta} \bar{\Delta}\mu \epsilon_{izj} p_j \right) - \frac{\eta'}{\eta + \eta'} \zeta' \bar{\Delta}\mu p_i p_z \quad . \tag{5.31}
$$

The flux term of Eq. (5.24) is given by

$$
\begin{aligned}
\bar{M}_{izk} &= \kappa \partial_k \bar{\Omega}_{iz} + \zeta_1 \bar{\Delta}\mu \epsilon_{izk} + \zeta_2 \bar{\Delta}\mu \epsilon_{izj} p_j p_k \\
&\quad + \zeta_3 \bar{\Delta}\mu (\epsilon_{ikz} p_z p_z - \epsilon_{zkj} p_j p_i) + \zeta_4 \bar{\Delta}\mu (\delta_{ik} p_k p_z - p_z p_z) \quad . \tag{5.32}
\end{aligned}
$$

Finally the boundary term is

$$
\begin{aligned}
\frac{1}{h} M_{izz}|_0^h &= \frac{1}{h} \left[\kappa \partial_z \Omega_{iz} + \zeta_2 \Delta\mu \epsilon_{izj} p_j p_z + \zeta_3 \Delta\mu (\epsilon_{izk} p_k p_z) \right] \\
&\simeq \xi_r \Omega_{iz} + \bar{\zeta}_2 \bar{\Delta}\mu \epsilon_{izj} p_j p_z + \bar{\zeta}_3 \bar{\Delta}\mu \epsilon_{izk} p_k p_z \tag{5.33}
\end{aligned}
$$

This completes our discussion of the torque balance in the thin film, and we are now ready to write down the equations of motion of the system.

5.2.4   Equations of motion of the thin film

Compiling the results from the previous section, we find the equations of motion of the thin film to be

$$
\partial_j \left(2\eta(\bar{u}_{ij} + \partial_k \bar{v}_k \delta_{ij}) + 2\eta'\bar{\Omega}_{ij} - 2\eta'\bar{\omega}_{ij} + \zeta'\bar{\Delta}\mu(p_i p_j - p_z^2 \delta_{ij}) + \tilde{\zeta}\bar{\Delta}\mu\epsilon_{ijz}p_z \right)
$$
$$
+ \quad \xi_f \bar{v}_i - \xi_\Omega \bar{\Omega}_{iz} + \zeta_{\text{glide}}\bar{\Delta}\mu p_i = 0 \quad , \tag{5.34}
$$

$$
\kappa\partial_k^2 \bar{\Omega}_{ij} + \partial_k \left[\zeta_2 \bar{\Delta}\mu\epsilon_{ijz}p_z p_k + \zeta_3 \bar{\Delta}\mu \left(\epsilon_{ikz}p_z p_j - \epsilon_{jkz}p_z p_i \right) + \zeta_4 \bar{\Delta}\mu \left(\delta_{ik}p_k p_j - \delta_{jk}p_k p_i \right) \right]
$$
$$
- \quad 2(2\eta'(\bar{\Omega}_{ij} - \bar{\omega}_{ij}) + \tilde{\zeta}\bar{\Delta}\mu\epsilon_{ijz}p_z) = \xi_r \Omega_{ij} + \bar{\zeta}_1 \bar{\Delta}\mu\epsilon_{ijz} + \bar{\zeta}_2 \bar{\Delta}\mu\epsilon_{ijz}p_z p_z
$$
$$
+ \quad \bar{\zeta}_3 \bar{\Delta}\mu(\epsilon_{izk}p_k p_j - \epsilon_{jzk}p_k p_i) \quad , \tag{5.35}
$$

$$
\kappa\partial_k^2 \bar{\Omega}_{iz} + \partial_k \left[\zeta_1 \bar{\Delta}\mu\epsilon_{izk} + \zeta_2 \bar{\Delta}\mu\epsilon_{izj}p_j p_k + \zeta_3 \bar{\Delta}\mu \left(\epsilon_{ikz}p_z p_z - \epsilon_{zkj}p_j p_i \right) + \zeta_4 \bar{\Delta}\mu \left(\delta_{ik}p_k p_z - p_z p_z \right) \right]
$$
$$
- \quad 2 \left(1 - \frac{\eta'}{\eta + \eta'} \right) \left(2\eta'\bar{\Omega}_{iz} + \tilde{\zeta}\bar{\Delta}\mu\epsilon_{izj}p_j \right) + 2\frac{\eta'}{\eta + \eta'}\zeta'\bar{\Delta}\mu p_i p_z
$$
$$
= \quad \xi_r \Omega_{iz} + \bar{\zeta}_2 \bar{\Delta}\mu\epsilon_{izj}p_j p_z + \bar{\zeta}_3 \bar{\Delta}\mu\epsilon_{izk}p_k p_z \quad , \tag{5.36}
$$

We next discuss some of the behaviors that emerge from these equations of motion in the context of carpets of chiral motors.

5.3   Fluid flows driven by carpets of chiral motors

Motivated by rotating cilia or bacteria attached to a surface, we consider a thin active film containing chiral motors that are aligned along the vector $\mathbf{p} = (\cos\varphi\sin\theta, \sin\varphi\sin\theta, \cos\theta)$. Here we have introduced the angle θ which describes the average tilt with respect to the surface normal vector and the angle φ which specifies the tilt direction with respect to the x-axis. For this discussion we constrain ourselves to simple nematic chiral motors, that are inspired by the structure of swimming *E. Coli* bacteria, see Fig. 1.7. For this case the coefficients $\zeta' = \bar{\zeta} = \tilde{\zeta} = \zeta_3 = \zeta_4 = \zeta_{glide} = 0$ Thus the equations of motion are greatly simplified and become

$$
\partial_j \left(2\eta(\bar{u}_{ij} + \partial_k \bar{v}_k \delta_{ij}) + 2\eta'\bar{\Omega}_{ij} - 2\eta'\bar{\omega}_{ij} \right) = \xi_f \bar{v}_i - \xi_\Omega \bar{\Omega}_{iz} \tag{5.37}
$$
$$
\kappa\partial_k^2 \bar{\Omega}_{ij} + \partial_k \zeta_2 \bar{\Delta}\mu\epsilon_{ijz}p_z p_k - 2(2\eta'(\bar{\Omega}_{ij} - \bar{\omega}_{ij}) = \xi_r \Omega_{ij} + \bar{\zeta}_1 \bar{\Delta}\mu\epsilon_{ijz} + \bar{\zeta}_2 \bar{\Delta}\mu\epsilon_{ijz}p_z p_z \tag{5.38}
$$
$$
\kappa\partial_k^2 \bar{\Omega}_{iz} + \partial_k \zeta_2 \bar{\Delta}\mu\epsilon_{izj}p_j p_k + \partial_k \zeta_1 \bar{\Delta}\mu\epsilon_{izk} - 2 \left(1 - \frac{\eta'}{\eta + \eta'} \right) \left(2\eta'\bar{\Omega}_{iz} \right) = \xi_r \Omega_{iz} + \bar{\zeta}_2 \bar{\Delta}\mu\epsilon_{izj}p_j p_z \tag{5.39}
$$

We first consider a homogeneous distribution of motors in an infinite system where all spatial derivatives vanish.
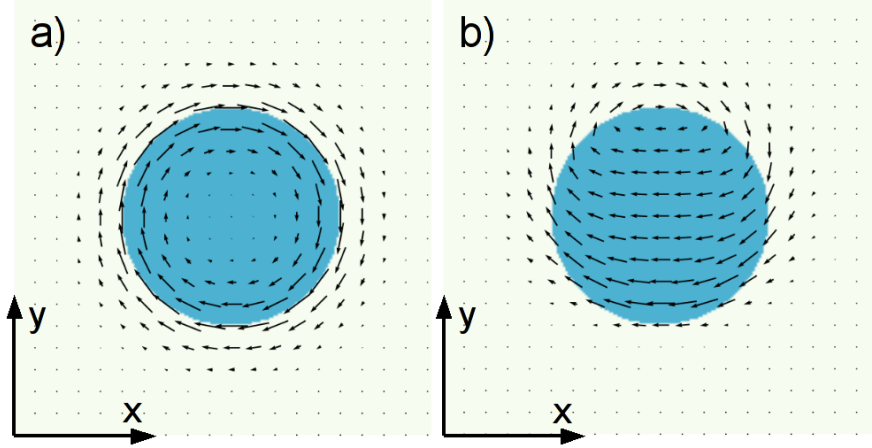
Figure 5.3: Flow fields (vectors) generated by a circular patch of chiral motors (blue). a) Average motor axis $\bar{\mathbf{p}}$ is perpendicular to the surface, i.e. $\theta = 0$. b) Average motor axis $\bar{\mathbf{p}}$ tilted at angle $\theta = \pi/4$ in y-direction. Flow fields were determined numerically in a square box of size L with periodic boundary conditions. Parameter values are $\eta' = \eta = h^2\kappa = h^2\xi_f = -h\xi_\Omega = \xi_r$, $\zeta_1 = -h\bar{\zeta}_1 = 10\zeta' = -10h\bar{\zeta}'$, $L = 20h$.

5.3.1 Homogeneous distribution of motors

In the case of a homogeneous distribution of motors on the surface Eq. (5.37) reads $\bar{v}_i = (\xi_\Omega/\xi_f)\bar{\Omega}_{iz}$. Using Eq. (5.39) we find

$$\bar{v}_i = \frac{\xi_\Omega \zeta_2 \bar{\Delta}\mu}{\xi_f} \frac{\epsilon_{izj}p_j p_z}{\xi_r + 4\eta\eta'/(\eta + \eta')} \quad . \tag{5.40}$$

A flow with a velocity $|\bar{\mathbf{v}}| \propto \sin(2\theta)$ is generated. The flow direction is perpendicular to the direction of tilt with respect to the surface normal vector. This case describes the collective generation of flow by carpets of cilia on a surface [18, 19, 67]. Note that ξ_Ω and therefore also the generated flow vanish in films that are symmetric with respect to $z \to h - z$. Ciliary carpets do have this asymmetry and can therefore generate flows [19]. Furthermore, we find from Eq. (5.38) an intrinsic rotation rate $\bar{\Omega}_{xy} = (\zeta_2\bar{\Delta}\mu\cos^2\theta + \bar{\zeta}_1\bar{\Delta}\mu)/(4\eta' + \xi_r)$ generated by the rotating motors with vorticity $\bar{\omega}_{xy} = 0$ in the hydrodynamic flow field.

5.3.2 A patch of chiral motors

As a second example we consider a circular patch of radius R that contains active motors. This is described by position dependent coefficients $\zeta_2\bar{\Delta}\mu(\mathbf{r}) = \zeta_2\bar{\Delta}\mu\Theta(R - |\mathbf{r}|)$ and by similar expressions for $\bar{\zeta}_1$, ζ_2 and ζ_1, where $\Theta(r)$ is the Heaviside function. We numerically solve Eqs. (5.37), (5.38) and (5.39) with periodic boundary conditions for boxsize $L = 4R$ using Fourier transforms, see Fig. 5.3. The velocity field for a tilt angle $\theta = 0$ is displayed in Fig. 5.3 (a). The patch generates a chiral flow field driven by

the intrinsic rotations $\bar{\Omega}_{xy}$. The stream lines are concentric circles. The flow velocity is maximal at the edge of the patch and decays exponentially outside. There is no net transport across the patch. If the motors are tilted with $\theta \neq 0$ along the y axis, a net transport in x direction across the patch with velocity proportional to $\sin(2\theta)$ appears in addition to the circular flow, see Fig. 4.3 (b).

5.4   Summary

We started the chapter with an example for the complex rheological behavior of a chiral fluid in the presence of boundaries. We investigated the flows that an active chiral fluid between to parallel plates creates. Even though individual polar chiral motors do not generate a hydrodynamic far field, a collection at sufficient density gives rise to flows at large distance from a surface which is induced by a boundary layer of thickness ℓ. As a result, an active chiral fluid with polar order confined between two plates can generate spontaneous relative motion of the plates and shear stresses between the plates. The direction of the motion Δv is proportional to $\mathbf{p} \times \mathbf{n}$, where $\mathbf{n}$ is the vector normal to the plate. We have shown that the stresses on the plates are linear in the density of chiral motors and does for $\ell \ll d$ not depend on the distance between plates.

We then generalized this result and developed a coarse grained description for thin active films in with active chiral processes.

We discussed our theory in the context of carpets of chiral beating cilia and bacteria attached to a surface. Specifically, we have shown that homogeneous distributions of chiral motors attached to a surface and tilted with respect to the surface normal vector, generate directed flows over large distances in the direction perpendicular to the tilt direction. The velocity of this net flow is maximal for tilt angles of $\theta = 45°$. This result accounts for the generation of net flows and left-right symmetry breaking by carpets of cilia in the mouse ventral node [17–19] and Kupffer's vesicle in zebrafish [71]. Note that in both cases a tilt angle with respect to the surface normal can be defined [67]. Interestingly, reported tilt angles vary between 30° and 50° [72], which is close to the angle of maximum transport velocity. Moreover in the case of finite patches of chiral motors, intrinsic rotation rates drive chiral flows along the edge of the patch. This phenomenon was reported in recent experiments on bacterial films on solid surfaces [74].

Our theory highlights the role of the intrinsic rotation field $\Omega_{\alpha\beta}$ for active chiral processes. In particular we find net flows without vorticity generated by intrinsic rotations in a homogeneous system, see Eq. (5.40). Note that in passive bulk fluids $\Omega_{\alpha\beta}$ converges to the flow vorticity after a relaxation time that in general is short [29].

Our work shows that the hydrodynamic flow velocity $\mathbf{v}$ and the intrinsic rotation rate $\Omega_{\alpha\beta}$ in active chiral films are coupled by the active processes and by the boundary conditions. This can give rise to complex flow patterns generated by carpets of chiral motors.

Another example of a thin film with chiral motors is the cell cortex of the one-cell stage embryo of the nematode worm *C. elegans*. Discussing this system is the content of the next chapter.

Chapter 6

The cell cortex is an active chiral fluid

In this chapter we discuss cortical flows in the cell cortex of the one cell stage embryo of the nematode worm *Caenorhabditis elegans*, (see Fig. 1.4). We present a theory that describes the cortex as an active chiral fluid, and compare theoretical predictions for cortical flows with experimental data.

The cortical flows in the *C. elegans* embryo are interesting for two reasons: (i) they are involved in the symmetry breaking process that enables the cell to divide asymmetrically, and plays an important role in the development of the whole organism [21, 65, 66]; (ii) they provide a simple setup that allows to test theoretical predictions on the rheology of active chiral fluids, against experimental data in a quantitative way.

The work in this chapter is an extension of earlier work on the *C. elegans* cell cortex published in [21], but unlike earlier work includes active chiral effects.

6.1 The *C. elegans* cell cortex

The cell cortex is a thin layer of filamentous proteins (actin) and molecular motors (non-muscle myosin II) directly beneath the cell membrane, see Fig. 6.1. The *C. elegans* embryo divides asymmetrically. This asymmetry between the anterior (A) and the posterior (P) is reflected in the material properties of the cortex [21, 66]. Specifically the concentration of myosin motors in the cell cortex shows gradients along the AP-axis. The embryo is however azimuthally symmetric. In the following we call the thin dimension of the cell cortex z, and the direction along the AP-axis x and the one orthogonal to it y, see Fig. 6.1.

Cortical actin filaments are believed nucleate at the cell membrane, and disassemble on the cytoplasmic side of the cortex [5, 104]. They grow almost parallel to the membrane and form an entangled network. Thus, the cortex has a broken symmetry in the thin dimension, but is isotropic within the cortical layer, see Fig. 6.1 (b) and (c), such that $\mathbf{p} = \hat{\mathbf{e}}_z$. Myosin motors set the network under stress [55].
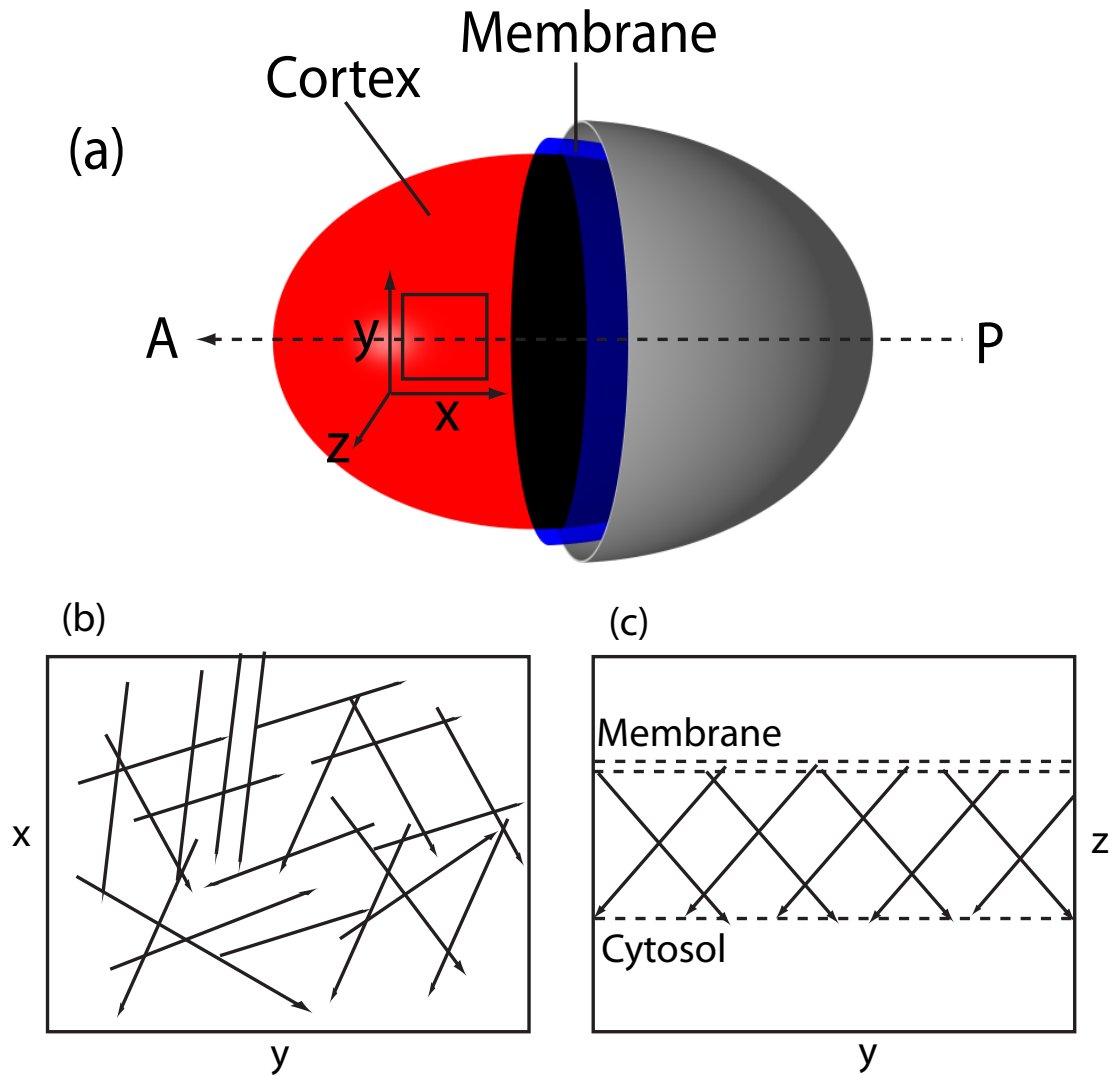
Figure 6.1: Schematic representation of the structure of the cell cortex. (a): The *C. elegans* cell cortex is a thin film of actin and molecular motors underlying the cell membrane. Immediately after fertilization it breaks the symmetry between anterior (A) and posterior (P). (b): Actin filament orientations (black arrows) are randomly distributed within the cortical plane (xy). (c): The symmetry is broken in the thin dimension since filaments nucleate at the membrane (arrow tail) and disassemble (arrow head) at the cytosolic side of the cortex.

The cortex is a highly dynamic structure. Actin filaments undergo tread-milling [45] and the motor molecules bind and unbind dynamically. The typical turnover time of the cell cortex in a wild type *C. elegans* embryo is estimated to be on the order of 30s [21]. Thus on time scales longer than this, the cortex is an active viscous fluid.

6.2   Measuring cortical flows

We measure cortical flows and concentration of myosin motors, closely following the experimental protocol outlined in [21]. We now summarize the techniques used.

6.2.1   Imaging and measurement scheme

A one-cell stage embryo of *C. elegans* is plated between two cover slips, and slightly compressed such that it is locally flattened, as illustrated in Fig. 6.2. The motor protein myosin II is tagged with Green Fluorescent Protein (GFP). The fluorescence intensity in the cortical layer is imaged at regular intervals using a confocal microscope. In this way a fluorescence movie is obtained. We evaluate the movies under the assumptions that:

- The fluorescence intensity is proportional to the local density of active myosin motors, such that the movies recorded are direct measurements of the instantaneous myosin distributions.

- The dynamics of the myosin distribution is dominated by advection on the time scale between two consecutive frames of the movie. We can therefore extract the center of mass flows of the cortical material through Particle Image Velocimetry (PIV) [105] of the myosin fluorescence images.

- The *C. elegans* embryo is azimuthaly symmetric. Deviations of the velocity vectors along the *y*-direction are due to fluctuations of the myosin density and average to zero.

We extract two key informations from the movie. The first is the instantaneous concentration of molecular motors. The second is the instantaneous flow velocity of the cell cortex.

Myosin density measurement

The density of cortical myosin is proportional to the measured fluorescence intensity. We exploit the azimuthal symmetry of the *C. elegans* embryo to obtain the profile of myosin density along the AP-axis. For each movie, we define the largest rectangular box that is entirely inside the embryo and oriented along the AP-axis. The box is then divided into equal sized bins along the AP-axis, see Fig. 6.3 (a). The integrated fluorescence intensity I in each bin is obtained by summing the fluorescence intensity values for each pixel in
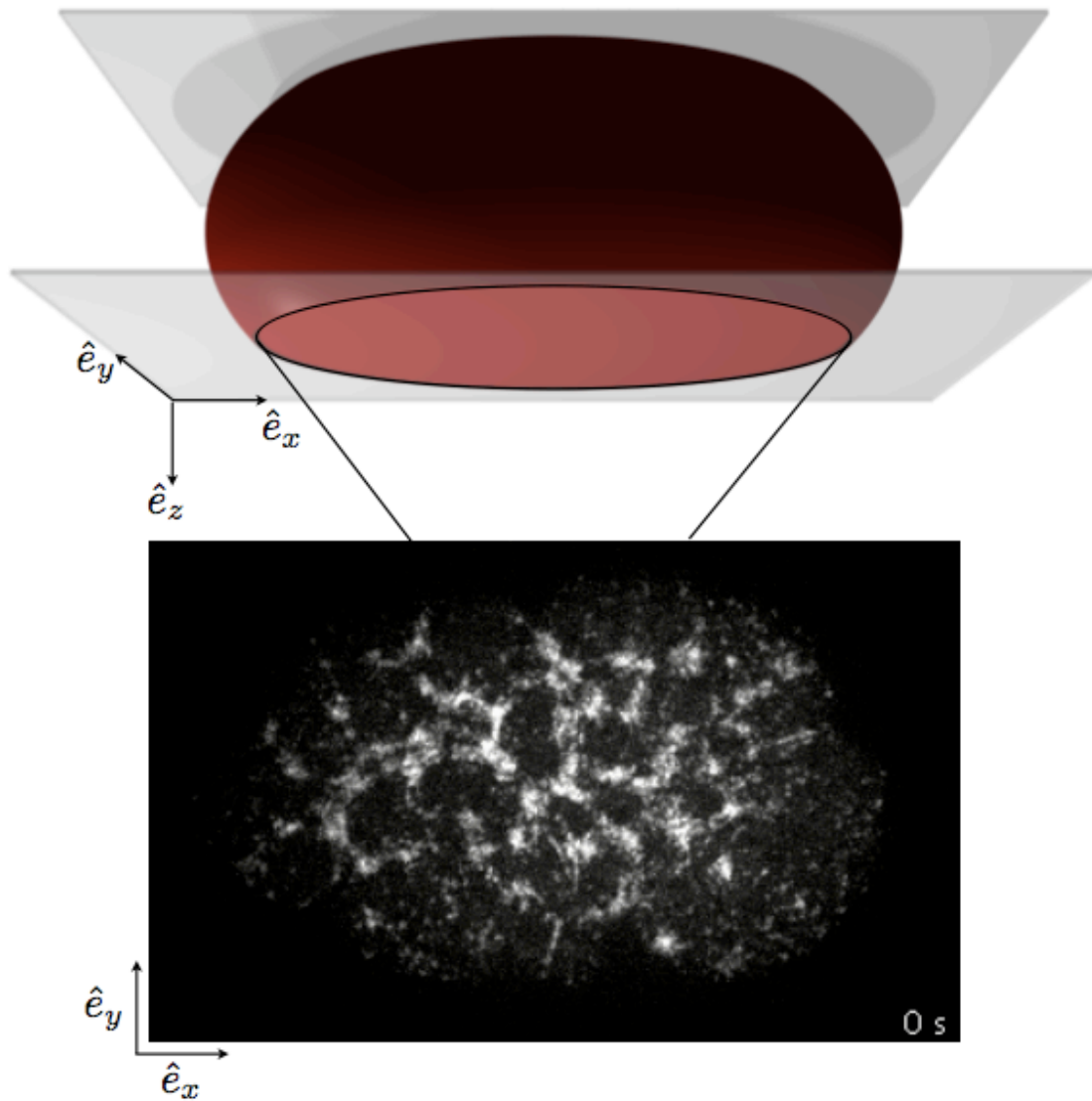
Figure 6.2: Schematic illustration of the imaging scheme [21]. The embryo is mounted between two cover slips. The cortex is imaged in the flat elliptical region of the egg that is pressed against the lower cover slip. A fluorescence movie is obtained in this way.

each bin. The integrated fluorescence intensity I is a measure for the active tension T in the cell cortex, such that

$$T = \alpha I \quad , \tag{6.1}$$

where α is an unknown proportionality constant, that relates fluorescence intensity to active tension. Note that α is a property of the imaging system, and could in principle be determined by careful calibration.

Flow velocity measurement

We measure velocities of the cortical flows using PIV [105]. The PIV method works as follows.

Let $P_n(x, y)$ denote the intensity value of the pixel at point (x, y) in the n-th frame of the movie. We first choose a template box of $d \times d$ pixels that is centered around the position (x, y) in the n-th frame. We then numerically evaluate the normalized cross-correlation function $X_n(x, y, \Delta x, \Delta y)$, that measures the similarity between the template box and a box of equal size centered around $(x + \Delta x, y + \Delta y)$ in the subsequent frame. Here Δx and Δy are displacements and the normalized cross-correlation function is given by

$$X_n(x, y, \Delta x, \Delta y) =$$

$$\frac{\sum\limits_{x'=x-d}^{x+d} \sum\limits_{y'=y-d}^{y+d} \left\{ \left[P_n(x', y') - \bar{P}_n(x, y) \right] \left[P_{n+1}(\Delta x + x', \Delta y + y') - \bar{P}_{n+1}(x + \Delta x, y + \Delta y) \right] \right\}}{\sqrt{\sigma_n^2(x, y)\sigma_{n+1}^2(x + \Delta x, y + \Delta y)^2}} \quad , \tag{6.2}$$

where

$$\bar{P}_n(x, y) = \left(\frac{1}{2d+1} \right)^2 \sum\limits_{x'=x-d}^{x+d} \sum\limits_{y'=y-d}^{y+d} P_n(x', y') \quad , \tag{6.3}$$

and

$$\sigma_n^2(x, y) = \left(\frac{1}{2d+1} \right)^2 \sum\limits_{x'=x-d}^{x+d} \sum\limits_{y'=y-d}^{y+d} P_n^2(x', y') - \bar{P}(x, y)^2 \quad . \tag{6.4}$$

We then search for the displacements $\Delta x = \Delta x_0$ and $\Delta y = \Delta y_0$ that maximize the normalized cross-correlation function $X_n(x, y, \Delta x, \Delta y)$. This can be done to sub-pixel accuracy using an interpolation scheme based on fast Fourier transforms [106]. The instantaneous velocity at time n and position (x, y) is then given by

$$\bar{v}_x = \frac{k}{\tau} \Delta x_0 \quad , \tag{6.5}$$

$$\bar{v}_x = \frac{k}{\tau} \Delta y_0 \quad , \tag{6.6}$$

where τ is the time between two subsequent frames and k is the size of a pixel.

We obtain binned averages of the velocities using the bins shown in Fig. 6.3 (a) and obtain velocity profiles along the AP-axis.

6.2.2 Cortical flows in the one cell stage embryo

Between fertilization and the first cell division several episodes of cortical flows occur. In the frameworks of this thesis we investigate two of them: (i) cortical retraction, which occurs around 15 min post fertilization and (ii) cortical rotation which occurs around 30 minutes post fertilization, shortly before the cell divides. Both of these flows are chiral and their chirality is conserved between different individuals. The chiral symmetry breaking in (i) and (ii) is thus clearly not spontaneous. This distinguishes the flows in the cell cortex of *C.elegans* qualitatively from the spontaneous symmetry breaking flows in the Taylor Couette motor that we discussed in chapter 3.

Cortical retraction

Around 15 minutes post-fertilization strong cortical flows occur, which are involved in the establishment of the anterior-posterior axis of the embryo [21, 66]. We quantify the myosin density and the flow velocities, see Fig. 6.3. The flow is predominantly oriented along the AP-axis, and goes from the posterior towards the anterior. The AP-component of the flow velocity v_x peaks at a velocity of $|v_x| \simeq 5\mu$m/min, see Fig. 6.3 (c).

The azimuthal flow component v_y is slower and peaks at around $|v_y| \simeq 2\mu$m/min, see Fig. 6.3 (d). The flow switches its direction at the boundary between the posterior and the anterior half of the embryo. The azimuthal flow has a well defined chirality. When viewed from the anterior pole of the embryo, the anterior half of the cell performs a clockwise rotation. Similarly, when viewed from the posterior pole of the embryo, the posterior half of the cell performs a clockwise rotation. This chirality is conserved between embryos. We can therefore rule out that the chiral symmetry is broken spontaneously.

The function of this twisting motion during cortical retraction is unclear. However, at later stages during the *C. elegans* development, cells perform similar chiral twisting motions during cell division. These twisting motion has been linked to the LR-symmetry breaking of the entire organism [107]. A similar mechanism seems to be at work during the LR-symmetry breaking of snails [108].

Cortical rotation

Around 30 minutes after fertilization, shortly before the embryo undergoes cell division the whole cell cortex rotates around the AP-axis by several tens of degrees. During the flow episode of cortical rotation the AP-flow velocity $v_x \simeq 0\mu$m/min is negligible. The azimuthal flow velocity v_y is peaks at $|v_y| \simeq 20\mu$m/min. This is substantially faster than the flows during cortical retraction. In wild-type animals the rotation is always right handed with respect to the AP-axis. Thus the symmetry is clearly not broken by spontaneous symmetry breaking mechanisms, but must be broken by a symmetry cue that is internal to the cell cortex. The exact quantification of the cortical rotation flows is still ongoing work, we thus do not include the preliminary data in this thesis.

The function of the cortical rotation is unclear. RNAi experiments show that worms deficient in some proteins, do not show the rotation, while cell division is still successful.
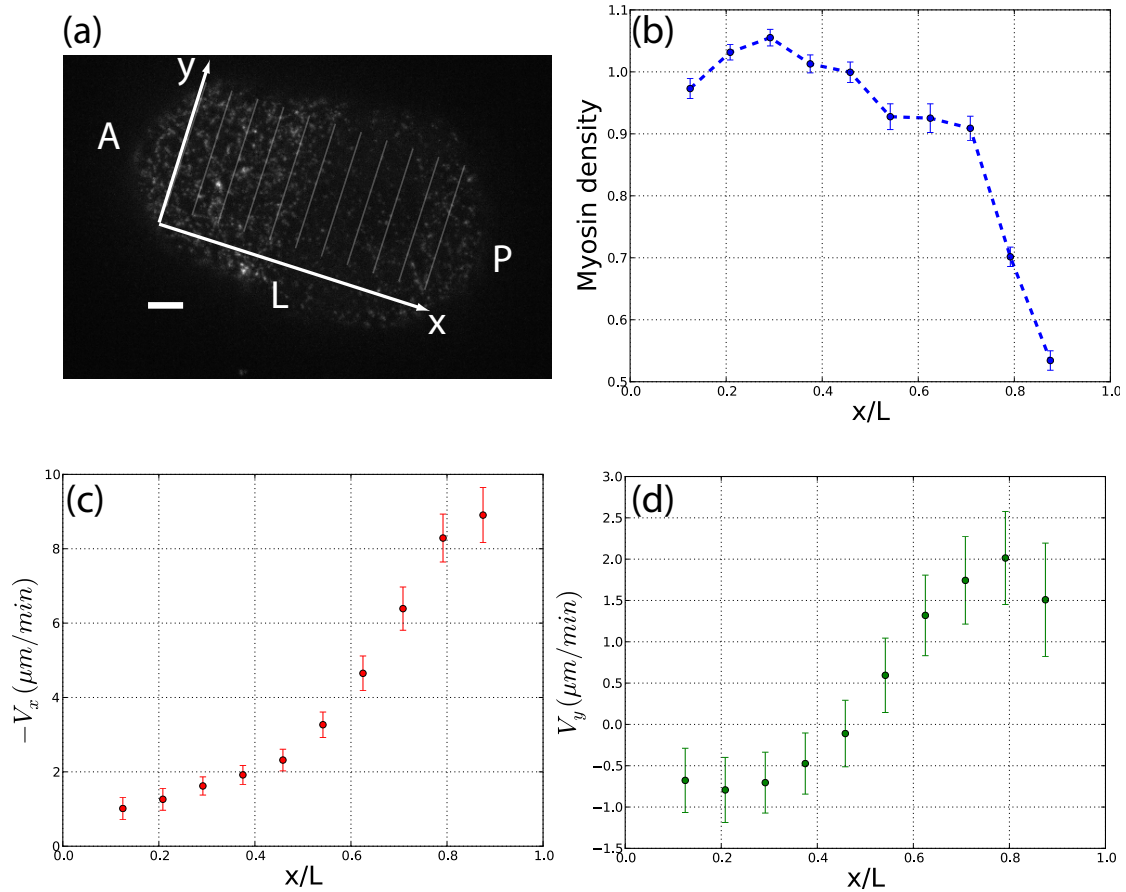
Figure 6.3: Measured flow velocities and myosin density profile during cortical retraction: (a): Image of one embryo. The x direction is chosen to from anterior (A) to posterior (P), the y direction is the azimuthal one. The total length of the embryo is L. Semitransparent lines indicate the binning we use for averaging the measurements. The white scale bar indicates 5 μm ; (b): myosin density profile along the AP-axis in arbitrary units; (c): x-velocity profile along the AP-axis in μm per minute; (d): y-velocity profile along the AP-axis in μm per minute. The data has been obtained by averaging over $N = 10$ wild type embryos over a time interval of 100 seconds, at 30% cortical retraction. The error-bars indicate 95% confidence intervals.

However there are no viability studies on these worms and it is unknown if they develop into healthy adults [109]. For us the cortical rotation is interesting since it reveals some of the underlying mechanical properties of the cell cortex.

6.3 Hydrodynamic description of the cell cortex

We now derive equations of motion for the cell cortex. The derivation closely follows the steps outlined chapter 5. However, since the intrinsic rotation rate $\Omega_{\alpha\beta}$ in the cell cortex, can not be measured directly, we simplify the theory from chapter 5 in such a way, that we do not need to refer to the intrinsic rotation rate explicitly. This is possible because the length scale $\ell = \sqrt{\eta'/\kappa_0}$, on which the intrinsic rotation rate $\Omega_{\alpha\beta}$ differs from the vorticity $\omega_{\alpha\beta}$, is much smaller than the characteristic length of the flows we are interested in. We start by discussing the constitutive equations for the cortical bulk material.

6.3.1 Constitutive equations

We consider the cell cortex as a chiral active fluid with the constitutive equations

$$\sigma_{\alpha\beta} = 2\eta u_{\alpha\beta} + \bar{\zeta}\Delta\mu\delta_{\alpha\beta} + \zeta\Delta\mu(p_\alpha p_\beta - \delta_{\alpha\beta}) \quad , \tag{6.7}$$

$$\sigma_{\alpha\beta}^a = 2\eta'(\Omega_{\alpha\beta} - \omega_{\alpha\beta}) + \tilde{\zeta}\Delta\mu\epsilon_{\alpha\beta\gamma}p_\gamma \quad , \tag{6.8}$$

$$M_{\alpha\beta\gamma} = \kappa\partial_\gamma\Omega_{\alpha\beta} + \zeta_0\Delta\mu\epsilon_{\alpha\beta\gamma} + \zeta_1\Delta\mu\epsilon_{\alpha\beta\nu}p_\nu p_\gamma \quad , \tag{6.9}$$

where $\mathbf{p} = \hat{e}_z$ is a local anisotropy of the material, that is given by the local average of actin filament orientations, see Fig. 6.1.

6.3.2 Equations of motion

To obtain equations of motion for the cortical material, we use the constitutive equations (6.7-6.9) together with the force balance Eq. (2.11) and the torque balance Eq. (2.22) at low Reynolds number. Since $\mathbf{p} = \hat{e}_z$ is constant the hydrostatic stress simplifies to the hydrostatic pressure and $\sigma_{\alpha\beta}^e = P\delta_{\alpha\beta}$. Moreover there are no hydrostatic fluxes of angular momentum $M_{\alpha\beta\gamma}^e = 0$. The 3D torque and force balances for the cortical material read,

$$(\eta + \eta')\partial_\gamma^2 v_\alpha + 2\eta'\partial_\beta\Omega_{\alpha\beta} + \partial_\alpha(\bar{\zeta}\Delta\mu - \zeta\Delta\mu + P) + \partial_\beta(\zeta\Delta\mu p_\alpha p_\beta + \tilde{\zeta}\Delta\mu\epsilon_{\alpha\beta\gamma}p_\gamma) = 0 \quad , \tag{6.10}$$

$$\kappa\partial_\gamma^2\Omega_{\alpha\beta} + \partial_\gamma(\zeta_0\Delta\mu\epsilon_{\alpha\beta\gamma} + \zeta_1\Delta\mu\epsilon_{\alpha\beta\nu}p_\nu p_\gamma) = 2\eta'(\Omega_{\alpha\beta} - \omega_{\alpha\beta}) + \tilde{\zeta}\Delta\mu\epsilon_{\alpha\beta\gamma}p_\gamma \quad , \tag{6.11}$$

where we used that the fluid is incompressible, i.e. that $\partial_\gamma v_\gamma = 0$. After a little algebra we obtain a fourth order differential equation for the velocity $\mathbf{v}$,

$$
\begin{aligned}
0 = \quad & \eta \partial_\gamma^2 v_\alpha + \partial_\alpha(\bar{\zeta}\Delta\mu - \zeta\Delta\mu + P) + \partial_\beta\left[\zeta\Delta\mu p_\alpha p_\beta + \partial_\gamma(\zeta_1\Delta\mu\epsilon_{\alpha\beta\nu}p_\nu p_\gamma)\right] \\
& -\frac{\kappa}{2\eta'}\partial_\nu^2\left[(\eta + \eta')\partial_\gamma^2 v_\alpha + \partial_\alpha(\bar{\zeta} - \zeta\Delta\mu + P) + \partial_\beta(\zeta\Delta\mu p_\alpha p_\beta + \tilde{\zeta}\Delta\mu\epsilon_{\alpha\beta\gamma}p_\gamma)\right] \quad .
\end{aligned}
$$

$$(6.12)$$

The length scale $\ell = \sqrt{\kappa/\eta'}$ is the length on which the intrinsic rotation rate $\Omega_{\alpha\beta}$ decays to the vorticity $\omega_{\alpha\beta}$ and is set by some molecular lengths in the system. An upper bound for an estimate to ℓ is the thickness d of the cell cortex, which is of the order of 1μm. Later will show that the characteristic range of flows in the cell cortex is much longer then this. Thus, for simplicity from we consider the limit of $\ell = \sqrt{\kappa/\eta'} \to 0$. The theory that we obtain only applies on length scales larger then ℓ. The equation of motion becomes,

$$
0 = \eta\partial_\gamma^2 v_\alpha + \partial_\alpha(\bar{\zeta}\Delta\mu - \zeta\Delta\mu + P) + \partial_\beta\left[\zeta\Delta\mu p_\alpha p_\beta + \partial_\gamma(\zeta_1\Delta\mu\epsilon_{\alpha\beta\nu}p_\nu p_\gamma)\right] \quad . \quad (6.13)
$$

Since we know that $\mathbf{p}$ points in the z direction and we are only interested in velocities in the in-film directions we can simplify this even further to,

$$
0 = \eta\partial_\gamma^2 v_i + \partial_i(\bar{\zeta}\Delta\mu - \zeta\Delta\mu + P) + \partial_j\partial_z(\zeta_1\Delta\mu\epsilon_{ijz}p_z^2) \quad , \quad (6.14)
$$

where roman indices only indicate the in film directions x and y. The cell cortex is a thin film. That means that its extension L the in film directions is much larger than its thickness d. In thin films

$$
\sigma_{zz}^{tot} \approx P^{ext} \quad , \quad (6.15)
$$

where P^{ext} is the external pressure. In the following we choose $P^{ext} = 0$, which we can do without loss of generality since we are not interested in the description of flows driven by externally applied pressure gradients. Equation (6.15) expression, together with the constitutive equation for the stress Eq. (6.7) yields,

$$
\eta\partial_z v_z + \bar{\zeta}\Delta\mu - \zeta\Delta\mu + P + \zeta\Delta\mu p_z^2 = 0 \quad . \quad (6.16)
$$

Using the incompressibility of the fluid $\partial_\gamma v_\gamma = 0$ we find,

$$
\eta\partial_i v_i - \bar{\zeta}\Delta\mu + \zeta\Delta\mu - P - \zeta\Delta\mu p_z^2 = 0 \quad . \quad (6.17)
$$

The equation of motion of the fluid can thus be expressed without referring to the hydrostatic pressure. Finally average the equation of motion over the thickness of the film. We introduce the averaged velocity

$$
\bar{v}_i = \frac{1}{d}\int_0^d dz v_i \quad , \quad (6.18)
$$

and the active cortical tension

$$T = \frac{1}{d} \int_0^d dz \zeta \Delta \mu \quad .$$

(6.19)

The cortical equation of motion in terms of $\bar{v}_i$ and T read

$$0 = \eta \partial_j^2 \bar{v}_i + \eta \partial_i \partial_j \bar{v}_j - p_z^2 \partial_i T + \partial_j \frac{1}{d} (\zeta_1 \Delta \mu \epsilon_{ijz} p_z^2)|_0^d + \frac{1}{d} \eta \partial_z v_i|_0^d \quad .$$

(6.20)

We express the boundary terms by,

$$\frac{1}{d} \eta \partial_z v_i|_0^d = -\gamma \bar{v}_i$$

(6.21)

and

$$\frac{1}{d} (\zeta_1 \Delta \mu \epsilon_{ijz} p_z^2)|_0^d = -c \epsilon_{ij} T \quad ,$$

(6.22)

where $\epsilon_{ij} = \epsilon_{ijz}$. Here we have introduced the friction coefficient γ and the dimensionless proportionality factor c, that quantifies the relative strength of active chiral and active contractile processes. Finally, using that $p_z^2 = 1$, we write the 2D equation of motion of the cell cortex,

$$\eta \partial_j^2 \bar{v}_i + \eta \partial_i \partial_j \bar{v}_j - \gamma \bar{v}_i \quad = \partial_j \left(\delta_{ij} T + c \epsilon_{ij} T \right) .$$

(6.23)

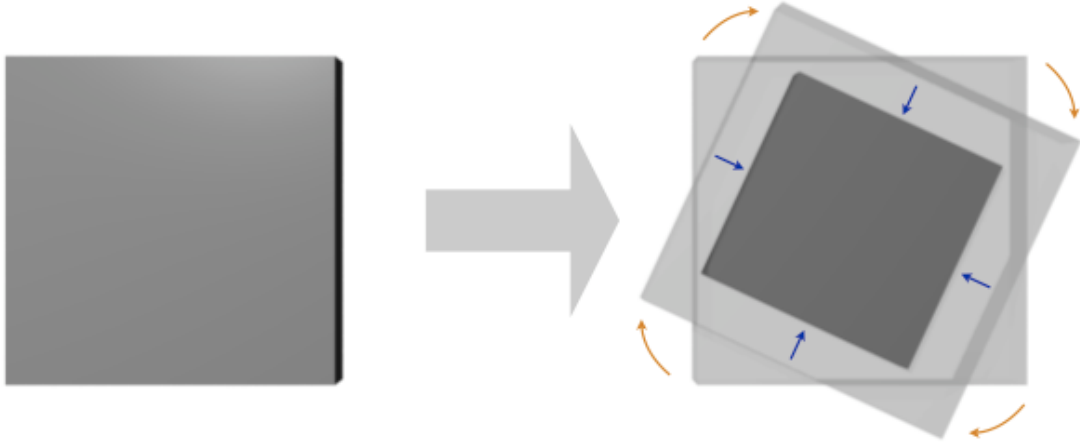Since the cell cortex is azimuthal symmetric Eq. (6.23) decouples into two different

Figure 6.4: Sketch of the equations of motion of the cell cortex. The activity of the cell cortex provides it with the tendency to actively contract (blue arrows) and rotate with respect to the cytosol (red arrows).

equations for the x and the y direction,

$$\begin{aligned} 2\eta \partial_x^2 \bar{v}_x - \gamma \bar{v}_x \quad &= \quad \partial_x T \\ \eta \partial_x^2 \bar{v}_y - \gamma \bar{v}_y \quad &= \quad -c \partial_x T \quad . \end{aligned}$$

(6.24)

Note, that in writing Eqs. (6.24) we implicitly assumed that the cortical viscosity η and the chirality index c do not depend on space. The active cortical tension T drives cortical flows that are resisted by viscous dissipative processes quantified by η and frictional dissipation quantified by γ. The relative magnitude of contractile and rotational processes is encoded in the chirality index c, see Fig. 6.4.

The active cortical tension T and the velocity of the cortex $\bar{\mathbf{v}}$ can be measured. We next discuss how compare equations (6.24) to experimental results to obtain measurements of the material properties of the cell cortex.

6.3.3 Material properties of the cell cortex

While our experiments do not permit to directly measure forces, we can determine some important material properties of the cell cortex using our theory. These material properties are the hydrodynamic length $l = \sqrt{2\eta/\gamma}$ and the chirality index c. The hydrodynamic length l is a measure of the distance over which local contractions of the cell cortex propagate. The dimensionless chirality index c quantifies the relative importance of active contractile and active chiral processes. We discuss how we can obtain estimators for c and l using the velocity and tension profiles determined from experiment, assuming that the cell cortex is well described by Eqs. (6.24).

The first and second moment of Eqs. (6.24) are given by

$$2\eta \left[\partial_x \bar{v}_x \right] |_{x_0}^{x_1} - \gamma \int_{x_0}^{x_1} \bar{v}_x dx = T|_{x_0}^{x_1} \tag{6.25}$$

$$\eta \left[\partial_x \bar{v}_y \right] |_{x_0}^{x_1} - \gamma \int_{x_0}^{x_1} \bar{v}_y dx = -cT|_{x_0}^{x_1} \tag{6.26}$$

$$2\eta \left[x\partial_x \bar{v}_x - \bar{v}_x \right] |_{x_0}^{x_1} - \gamma \int_{x_0}^{x_1} x\bar{v}_x dx = (xT)|_{x_0}^{x_1} - \int_{x_0}^{x_1} T dx \tag{6.27}$$

$$\eta \left[x\partial_x \bar{v}_y - \bar{v}_y \right] |_{x_0}^{x_1} - \gamma \int_{x_0}^{x_1} x\bar{v}_y dx = -c \left[(xT)|_{x_0}^{x_1} - \int_{x_0}^{x_1} T dx \right] \tag{6.28}$$

These expressions can be solved for $l = \sqrt{2\eta/\gamma}$, and we obtain an estimator for the hydrodynamic length, that depends on the measured tension profile, and the measured AP-velocity $\bar{v}_x$,

$$l \simeq \sqrt{ \frac{ T|_{x_0}^{x_1} \int_{x_0}^{x_1} x\bar{v}_x dx - \left((xT)|_{x_0}^{x_1} - \int_{x_0}^{x_1} T dx \right) \int_{x_0}^{x_1} \bar{v}_x dx }{ T|_{x_0}^{x_1} \left[x\partial_x \bar{v}_x - \bar{v}_x \right] |_{x_0}^{x_1} - \left((xT)|_{x_0}^{x_1} - \int_{x_0}^{x_1} T dx \right) \left[\partial_x \bar{v}_x \right] |_{x_0}^{x_1} } } \; . \tag{6.29}$$

In the same way we obtain a second estimator for the hydrodynamic length, that depends on the measured tension profile, and the measured AP-velocity $\bar{v}_y$,

$$l \simeq \sqrt{2} \sqrt{\frac{T|_{x_0}^{x_1} \int_{x_0}^{x_1} x\bar{v}_y dx - \left((xT)|_{x_0}^{x_1} - \int_{x_0}^{x_1} T dx\right) \int_{x_0}^{x_1} \bar{v}_y dx}{T|_{x_0}^{x_1} \left[x\partial_x \bar{v}_y - \bar{v}_y\right]|_{x_0}^{x_1} - \left((xT)|_{x_0}^{x_1} - \int_{x_0}^{x_1} T dx\right) \left[\partial_x \bar{v}_y\right]|_{x_0}^{x_1}}} \quad . \tag{6.30}$$

Finally we also determine an estimate for the chirality index c

$$c \simeq -\frac{2l^2 \left[\partial_x \bar{v}_x\right]|_{x_0}^{x_1} - 2\int_{x_0}^{x_1} \bar{v}_x dx}{l^2 \left[\partial_x \bar{v}_y\right]|_{x_0}^{x_1} - \int_{x_0}^{x_1} \bar{v}_y dx} \quad . \tag{6.31}$$

This shows that assuming Eqs. (6.24) capture the essential feature of cortical flows it is possible to estimate the hydrodynamic length l and the chirality index c, directly from the measured data. The approach sketched in this section seems appealing since only ratios of active tension appear in Eqs. (6.29) to (6.31), and thus the unknown proportionality constant α that links the measured fluorescence intensity to the active stress, drops out of the calculations. It requires however performing derivatives on measured data, which in practice is imprecise on noisy data. We will introduce an alternative approach to determining the material properties of the cell cortex that is robust against noise in the next section where we discuss flows in *C. elegans* cell cortex.

6.4 Cortical flows: comparing theory and experiment

To test the cortical equations of motion (6.24) that we derived, we now check if they can capture the flow behaviors observed during (i) cortical retraction and (ii) cortical rotation.

6.4.1 Flows during cortical retraction

We measured profiles of active tension T and the velocity profile along the AP-axis during cortical retraction, see Fig. 6.3. To compare our theory to experiment, we numerically solve Eqns (6.24) using the two extreme points of the measured velocity profile as boundary conditions. Equations (6.24) depend on three free parameters, the hydrodynamic length l, the chirality index c, and the constant α that relates the measured fluorescence intensity to the active tension. We adjust these parameters by performing a least square fit of the solutions to Eqns (6.24) to the measured velocity profile. In this way we obtain values for the hydrodynamic length l and and the chirality index c numerically. We obtain error estimates for l and c and α from the Hessian of the residual of the least square fit with respect to the fit parameters.
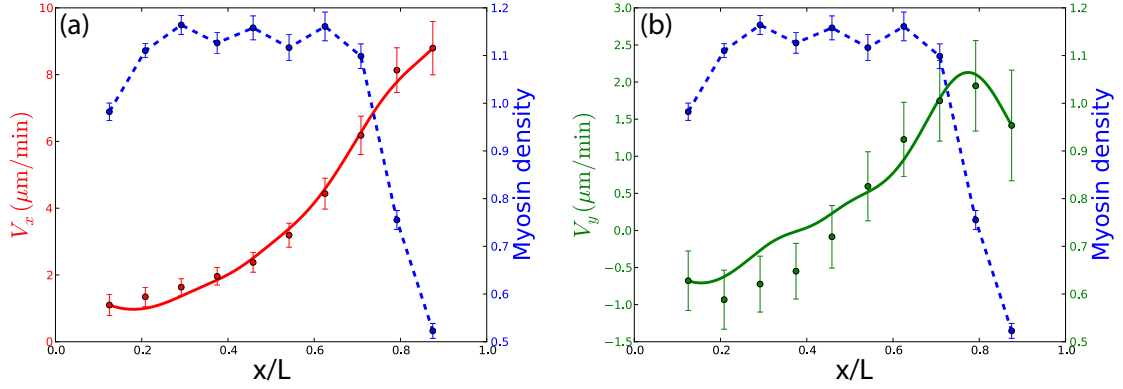
Figure 6.5: Velocities during cortical retraction. Theoretical prediction (solid lines) and experimental measurement (dots). The Myosin fluorescence intensity is shown in blue (dots and dashed line). In (a) we use only the x-velocity data to fit the theoretical flow profile to the experimental one. In (b) only the y-velocity data is used. The errorbars indicate 95% confidence intervals on the experimental data.

To check for consistency we do the fitting in two different ways: (i) we fit the x and y data separately using two independent two-parameter fits for l and α, and l and $c\alpha$, respectively; (ii) we perform a single three parameter fit for l, α and c. The best fit curves for method (i), using only the x or y data are shown in Fig. 6.5 (a) and (b), respectively. The fits obtained with strategy (ii) are shown in Fig. 6.6.

Both methods (i) and (ii) produce good agreement between the theoretical flow profile and the measured data. Moreover, they allow us to measure the material properties of the cell cortex.

The estimates for the hydrodynamic length we obtain from method (i) using the x-data is $l/L = 0.34 \pm 0.05$, where L is the length of the embryo. The error estimate we use is the standard deviation. From (i) using the y-data we find $l/L = 0.38 \pm 0.26$. From method (ii) we obtain $l/L = 0.33 \pm 0.09$. The three hydrodynamic length estimates are within each others errorbars and are thus consistent. The much larger standard deviation of method (i) using the y-data can be understood when remembering, that the peak velocity of the azimuthal flows during cortical retraction is much slower than the peak velocity of the x directed flows, while the absolute error in the velocity measurements remains the same. For this reason the relative measurement error on the y-velocities is larger, which is reflected in the larger error on the hydrodynamic length estimate.

Furthermore we obtain values for the chirality index c. Using method (i) we find $c = 0.52 \pm 0.56$, while with method (ii) we obtain $c = 0.47 \pm 0.43$. Both estimates are consistent, although subject to a large relative error. None the less, this result emphasizes the importance of active chiral processes in the cell cortex.
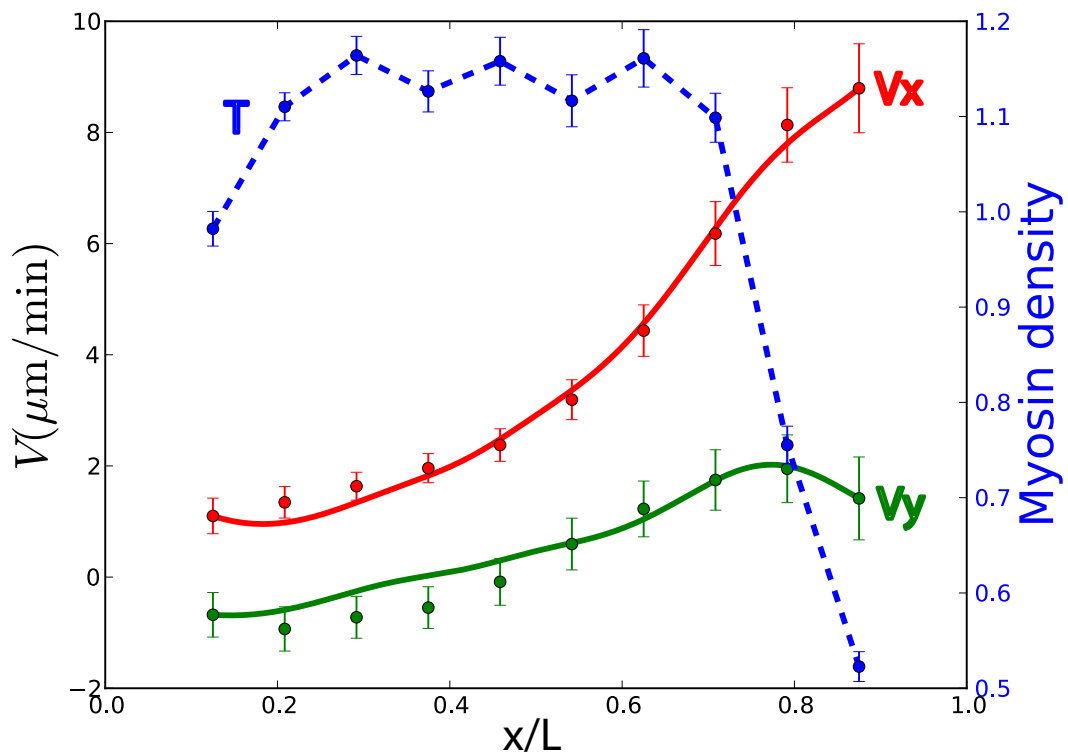
Figure 6.6: Velocities during cortical retraction. Theoretical prediction (solid lines) and experimental measurement (dots). The Myosin fluorescence intensity is shown in blue (dots and dashed line). One common fit using both x and y data has been performed. the x velocities are shown in red. The y-velocities in green. The errorbars indicate 95% confidence intervals on the experimental data.
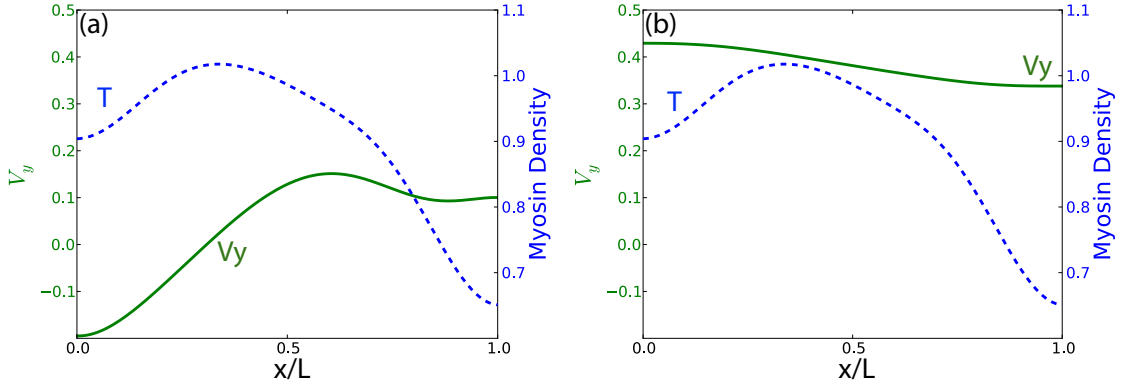
Figure 6.7: Velocity profile in the azimuthal direction (green) solved for the same myosin distribution (blue dashed line) for two different hydrodynamic length. (a): $l = 0.33L$ and (b): $l = 3.3L$.

6.4.2 Flows during cortical rotation

Shortly before the first cell division, the cell cortex performs a strong rotation around the AP-axis. Unlike the screw like twisting motion that is observed during cortical retraction, this motion is unidirectional, i. e. v_y has no sign-flip all along the x axis.

To understand how the equations of motion (6.23) can give rise to two behaviors that are so fundamentally different, we solve Eqs. (6.23) for the y velocities, using different values of for the hydrodynamic length l, imposing the active tension that is measured during the cortical retraction episode, see Fig. 6.7. We impose no flux boundary conditions on v_y. These are motivated, by the fact that the azimuthal symmetry of the embryo imposes a vanishing derivative of v_y at the poles.

For a small hydrodynamic length $l = 0.33L$, (Fig. 6.7 (a)) we find the screw like twist seen during cortical retraction. For large hydrodynamic length $l = 3.3L$ (Fig. 6.7 (b)), we find a uniform rotation of the cell cortex as the one observed in *C. elegans* prior cell division. Thus we hypothesize that the cell cortex actively up-regulates its hydrodynamic length prior cell division. While this hypothesis is in agreement with the observation that other cells round up prior cell division [110], it needs experimental verification.

6.5   Summary

In the present chapter we proposed a simplified version of the theory for thin active films developed in chapter 5, to describe flows in the cell cortex of the one cell stage embryo of the nematode worm *C. elegans*. The main difference between the simplified theory and the full description in chapter 5 is that the simplified theory for the cell cortex does not refer to the intrinsic rotation rate. The advantage of this is that the theory only depends on quantities that we directly measure. The price we pay is that the simplified theory is hydrodynamic and does not capture phenomena on length scales shorter than

$\sqrt{\kappa/\eta'} \approx 1\mu\mathrm{m}$.

From the theoretical description two material properties of the cell cortex emerge. The first one is the hydrodynamic length $l = \sqrt{2\eta/\gamma}$. The hydrodynamic length quantifies the distance over which the effects of local contractions decay. The second material property is the dimensionless chirality index c which quantifies the relative importance of active contractile effects and active chiral processes.

We use our theory to describe two episodes of cortical flows: (i) flows during cortical retraction; and (ii) flows during the cortical rotation prior cell division. To validate our theoretical description of the cell cortex we show that velocity data measured during (i) can be fit using the theoretical description, using the measured active tension as an input. The fit depends on the two material properties of the cell cortex, the hydrodynamic length l and the chirality index c.

We measure the hydrodynamic length l of the cell cortex and the chirality index c. We find $l \approx 1/3L$, where L is the length of the worm. Moreover we find $c \approx 0.5$, which points to the importance of chiral phenomena in the cell cortex.

During the flow episode (ii), the cell cortex preforms a strong chiral rotation around the AP-axis of the cell. We hypothesize that during (ii) the hydrodynamic length is actively up-regulated. We show that increasing the hydrodynamic length compared to the values that we measured during (i) reproduces the strong uniform rotation of the cell cortex around the AP-axis that is observed in experiments.

Chapter 7

Summary and Outlook

In this chapter we give an overview of our findings, discuss the implications of our results and point towards possible directions for future research.

In chapter 2 we developed a generic theory for fluids in which active chiral processes take place. The main difference between the theory we present here, and earlier theories for active fluids [32–34] is that we allow for non-equilibrium contribution to the anti-symmetric stress and the spin angular momentum flux. This can be done by explicitly considering a spin angular momentum degree of freedom of local volume elements of the fluid, and is a generalization of earlier work in passive liquid crystals [24, 29] to active systems. We identify novel active terms that generate active antisymmetric stresses and active angular momentum fluxes. The generic theory for active chiral fluids includes terms are not hydrodynamic. Specifically, we consider an intrinsic rotation rate $\Omega_{\alpha\beta}$ of local volume elements which decays to the vorticity $\omega_{\alpha\beta}$ on short time and length scales in a passive fluid [29]. We show how to obtain the Navier Stokes equation as a limiting case of the generic theory. Moreover we show how to recover earlier theories for active fluids that do not consider non-equilibrium spin angular momentum fluxes.

The theory in chapter 2 only considers the viscous limit of active chiral fluids. Recently systematic approaches to treat visco-elastic active fluids have been developed [35]. However, they do not account for active chiral processes in the fluid. The interplay of elastic time scales with active chiral processes is very likely to lead to interesting new physics. Developing a theory that incorporates viscoelasticity and active chiral processes would therefore be interesting. Moreover the theory we present here does not include noise. Approaches to incorporate equilibrium and non-equilibrium fluctuations into the frameworks of active fluid theories have been forwarded [111]. It would be interesting to see how these approaches can be extended to active chiral fluids.

In chapter 3 we investigated the rheological properties of an active fluid without chiral processes in a Taylor-Couette geometry. We showed that chiral symmetry can be broken spontaneously for high enough active stresses and rotating steady states emerge even in the absence of external forces and torques. The system can work against external

torques and is thus a motor. We characterized its motor properties and plot torque-angular velocity diagrams. Moreover we discuss possible experimental realizations of the Taylor Couette motor.

The Taylor Couette motor described in 3 could be realized experimentally using actin gels with myosin motors in small Taylor Couette rheometers and might also be a suitable candidate for the construction of a rotational micro-motor. It could be fabricated using the microfabrication techniques described in [101]. From a theoretical perspective it would be interesting to extend the stability analysis which we performed to states with broken rotational symmetry. New states, similar to Taylor vortices in the classical Taylor-Couette system, might appear.

In chapter 4 we presented a more detailed overview on the microscopic origins of the active chiral terms in the generic theory. We introduced microscopic chiral force and torque dipoles and have shown that they can generate active stresses and angular momentum fluxes. We have shown that distributions of chiral force and torque dipoles generate the active terms in the constitutive equations propsoed in chapter 2. We calculated the flow and rotation fields around five elementary motors, which are the higher symmetric objects that can be created by distributions of microscopic torque and force dipoles.

The work in chapter 4 opens up several possibilities for further studies. Here we investigate the flow fields generated by individual elementary motors. However the interaction of several such object might lead to interesting effects. Specifically, in recent years the flow fields generated by interacting microswimmers of the pusher and puller types, i.e. non-chiral force dipoles, have been studied intensively for their swarming properties and as candidates for micromixing devices [113, 114]. The elementary motors that we introduce here expand the realm of possible flow fields that can be generated by simple microscopic motors and would be interesting to study on this behalf.

In chapter 5 we discussed the interaction of chiral fluids and boundaries. We showed that a suspension of chiral swimmers between to plates will generate hydrodynamic flows, even though the flow fields of the individual swimmers are not long ranged, via a boundary effect and exert a wall shear stress that is independent of the distance between the plates. We then developed a generic theory for thin films of fluid with chiral processes. We discussed the theory we obtain in the context of bacterial suspensions and carpets of beating cilia. We show that cilia which are tilted with respect to the surface they are attached to can drive a fluid flow in a direction orthogonal to the cilia tilt direction even if the distribution of cilia is homogeneous. If their distribution is not homogeneous additional flows driven by the interplay between the intrinsic rotation rate and the surface emerge. These results are in qualitative agreement with experimental observations [19, 74].

The work in chapter 5 could expanded in several directions. The collective behavior of suspensions of chiral particles between boundaries that we predict opens up to further studies. From a theoretical point of view it would also be interesting to expand our stud-

ies to multiple component fluid, to include concentration gradients of active swimmers. A phase diagram of possible flow behaviors could be systematically explored and would be informative when discussing the swarming behavior os micro-swimmers in confined spaces. Our prediction of chiral shear flows in chiral swimmers between two plates can be experimentally tested. For instance, a dense suspension of *E. coli* aligned in a gradient of chemical attractant might generate the chiral shear flows that we predict.

Moreover, the generic theory for active chiral fluids could also be expanded. Here, we discuss the theory only with respect to chiral active processes. It is however also possible to treat gliding essays and other non chiral processes occurring in thin films using the same framework. It would be interesting to extend the approach we are taking here to a fluid with several components and obtain a phase diagram of gliding essays, which has been shown experimentally to feature very complex pattern formation depending on the concentrations of molecular motors and filamentous proteins [112]. Moreover, it would be interesting expand the theory to study metachronal waves.

Finally, in chapter 6 we developed a theory for the cell cortex of the *C. elegans* embryo in the one-cell stage that includes active chiral processes. The theory is a simplified version of the generic theory for thin films presented in chapter 5. The main difference between the simplified theory and the one in chapter 5 is that we eliminate intrinsic rotation rates from the equations of motion by going to the hydrodynamic limit in the simplified theory. This theory reproduces the flows observed in the cell cortex during cortical retraction. We obtain two fit parameters from fitting the experimental data. The first is the hydrodynamic length, which is the length over which local contractions in the cell cortex decay. It is on the order of one third of the embryos length, which is in good agreement with earlier findings [21]. The second is the ratio between of active chiral stress and active contractile stress. This ratio turn out to be one the order of one half in the *C. elegans* embryo. Thus we conclude that chiral processes can not be ignored in the description of the cell cortex. This is also confirmed by experimental observation of strong chiral cortical flows at a later stage of the embryos development, shortly before the embryo undergoes cell division for the first time. We forward a hypothesis on the origin of this strong cortical rotation, stating that the embryos hydrodynamic length increases prior to cell division which is reminiscent of the stiffening and rounding up observed in other cell types shortly before cell division [110].

The work in chapter 6 can be extended in several ways. First and foremost our hypothesis on the origin of cortical rotation needs to be experimentally verified. Secondly, the approach we take to describe the cell cortex allows to characterize it in terms of collective material properties, namely the hydrodynamic length and the ratio between active chiral motion and active contractility. This enables us to check for the influence of different proteins on the collective behavior of the cell cortex, by performing loss of function experiments using RNAi. While a lot is known on the properties of many cortical proteins from in-vitro experiments, it has so far been difficult to judge their role in the cell cortex in in-vivo experiments. Our approach might allow us to get more insight in this respect and enable us to quantify the influence of different pro-

teins on the mechanical properties of the cortex. Finally, in our analysis we used the azimuthal symmetry of the *C. elegans* embryo, for simplicity. This constraint might be lifted, allowing for an even deeper understanding of the cell cortex as a mechanical entity.

The work presented in this thesis shows that active chiral processes in soft biological matter are a field of research that is interesting both for the novel physics that can be found, as well as for their relevance to biological processes, such as the left right symmetry breaking of developing organisms. Here we provide the basic tools needed to approach many these problems and discuss some possible applications. We show that the physics of many biological systems, such as the *C. elegans* cell cortex, can not be fully understood without considering active chiral processes.

Bibliography

[1] L. Wolpert, *Principles of Development. 2nd edition,* Oxford University Press, Oxford (2002).

[2] C. L. Henley, *Possible mechanisms for initiating macroscopic left-right asymmetry in developing organisms*, arXiv:0811.0055v2 (2008).

[3] C. L. Henley, *Possible origins of macroscopic left-right asymmetry in organisms*, arXiv:1112.2317v1 [q-bio.SC] (2011)

[4] L. N. Vandenberg and M. Levin, *Perspectives and open problems in the early phases of left-right patterning.* Seminars in cell and developmental biology **20**, 456-463 (2009).

[5] B. Alberts, A. Johnson, J. Lewis, M. Raff, K. Roberts, and P. Walter. *Molecular Biology of the Cell.* Taylor and Francis Group, New York (2002).

[6] R. Ueshima and T. Asami, *Single-gene speciation by left-right reversal: A landsnail species of polyphyletic origin results from chirality constraints on mating.* Nature **425**, 679 (2003).

[7] M. Hoso, T. Asami, and M. Hori, *Right-handed snakes: convergent evolution of asymmetry for functional specialization.* Biology Letters **3**, 169-172 (2007).

[8] M. Danilchik, E. E. Brown, K. Riegert, *Intrinsic chiral properties of the Xenopus egg cortex: an early indicator of left-right asymmetry?* Development **133**, 4517-4526 (2006).

[9] J. Xu, A. Van Keymeulen, N. M. Wakida, P. Carlton, M. W. Berns, H. R. Bourne, *Polarity reveals intrinsic cell chirality*, Proc. Natl. Acad. Sci. USA **22**, 9296-9300 (2007).

[10] A. Tamada, S. Kawase, F. Murakami, H. Kamiguchi, *Autonomous right-screw rotation of growth cone filopodia drives neurite turning.* J Cell Biol. **188**, 429-41 (2010).

[11] I. Sase, H. Miyati, S. Ishiwata, and K. Kinosita Jr., *Axial rotation of sliding actin filaments revealed by single-fluorophore imaging*, Proc. Natl . Acad. Sci . USA **94**, 5646-5650 (1997).

[12] A. Vilfan, *Twirling motion of actin filaments in gliding assays with non-processive Myosin motors*, Biophysical Journal **97**, 1130-1137 (2009).

[13] I. R. Gibbons, *Cilia and flagella of eukaryotes*, J. Cell Biol. **91**, 107s-124s (1981).

[14] D. Bray, *Cell Movements*, Garland Publishing, New York, 2nd ed. (2001).

[15] H. Sui, and K. H. Downing. *Molecular architecture of axonemal microtubule doublets revealed by cryo-electron tomography.* Nature **442**, 475-478 (2006).

[16] A. Hilfinger and F. Jülicher, *The chirality of ciliary beats*, Phys. Biol. **5**, 016003 (2008).

[17] S. Nonaka, Y. Tanaka, Y. Okada, S. Takeda, A. Harada, Y. Kanai, M. Kido, and N. Hirokawa, *Randomization of left-right asymmetry due to loss of nodal cilia generating leftward flow of extraembryonic fluid in mice lacking KIF3B motor protein*, Cell **95**, 829-837 (1998).

[18] S. Nonaka, S. Yoshiba, D. Watanabe, S. Ikeuchi, T. Goto, W.F. Marshall, H. Hamada, *De novo formation of left-right asymmetry by Posterior Tilt of Nodal Cilia*, PLoS Biol **3**, e268 (2005).

[19] J. Buceta, M. Ibañes, D. Rasskin-Gutman, Y. Okada, N.Hirokawa, J. C. Izpisúa-Belmontey, *Nodal cilia dynamics and the specification of the left/right axis in early vertebrate embryo development*, Biophysical Journal **89**, 2199-2209 (2005).

[20] J. W. van de Meent, I. Tuval, R. E. Goldstein, *Nature's microfluidic transporter: rotational cytoplasmic streaming at high Péclet Numbers*, Phys. Rev. Lett. **101**, 178102 (2008).

[21] M. Mayer, M. Depken, J. S. Bois, F. Jülicher, S. W. Grill, *Anisotropies in cortical tension reveal the physical basis of polarizing cortical flows*, Nature **467**, 617-621 (2010).

[22] N. Hirokawa, Y. Okada, Y. Tanaka, *Fluid dynamic mechanism responsible for breaking the left-right symmetry of the human body: the nodal flow*, Annu. Rev. Fluid. Mech. **41**, 53-72 (2009).

[23] J. L. Ericksen, *Anisotropic Fluids* , Arch. Ration. Mech. Anal. **4**, 231 (1960).

[24] F. M. Leslie, *Some constitutive equations for anisotropic fluids*, Q. J. Mech. Appl. Math. **19**, 357 (1966).

[25] P. C. Martin, O. Parodi, P. S. Pershan, *Unified hydrodynamic theory for crystals, liquid crystals, and normal fluids*, Phys. Rev. A. **6**, (1972).

[26] S. R. de Groot and P. Mazur, *Non-equilibrium Thermodynamics* , Dover ed., Dover Pub. (1984).

[27] P. G. de Gennes and J. Prost, *The Physics of Liquid Crystals* (Oxford University Press, Oxford) Vol. 2. (1995).

[28] H. Stark and T. C. Lubensky , *Poisson-bracket approach to the dynamics of nematic liquid crystals*, Phys. Rev. E **67**, 061709 (2003).

[29] H. Stark and T. C. Lubensky, *Poisson-bracket approach to the dynamics of nematic liquid crystals: the role of spin angular momentum*, Phys. Rev. E **72**, 051714 (2005).

[30] R. A. Simha, S. Ramaswamy, *Hydrodynamic fluctuations and instabilities in ordered suspensions of self-propelled particles*, Phys. Rev. Lett. **89**, 058101 (2002).

[31] Y. Hatwalne, S. Ramaswamy, M. Rao, R. A. Simha, *Rheology of active-particle suspensions*, Phys. Rev. Lett. **92**, 118101 (2004).

[32] K. Kruse, J. F. Joanny, F. Jülicher, J. Prost and K. Sekimoto, *Asters, vortices, and rotating spirals in active gels of polar filaments*, Phys. Rev. Lett. **92**, 078101 (2004).

[33] K. Kruse, J. F. Joanny, F. Jülicher, J. Prost, and K. Sekimoto, *Generic theory of active polar gels: a paradigm for cytoskeletal dynamics*, Eur. Phys. J. E **16**, 5 (2005).

[34] J.-F. Joanny, F. Jülicher, K. Kruse, and J. Prost, *Hydrodynamic theory for multicomponent active polar gels,* New Journal of Physics **9**, 422 (2007).

[35] A. C. Callan-Jones and F. Jülicher, *Hydrodynamics of active permeating gels*, New. J. Phys. **13**, 093027 (2011).

[36] S. Fürthauer, M. Neef, S. W. Grill, K. Kruse, F. Jülicher, *The Taylor-Couette motor: spontaneous flows of active polar fluids between two coaxial cylinders,* New J. Phys. **14**, 023001 (2012).

[37] F. Jülicher, K. Kruse, J. Prost, d, J.-F. Joanny, *Active behavior of the cytoskeleton*, Physics Reports **449**, 3-28 (2007)

[38] J. Howard, *Mechanics of Motor Proteins and the Cytoskeleton*, Palgrave Macmillan (2001).

[39] F. Rivero, B. Koppel, B. Peracino, S. Bozzaro, F. Siegert, C.J. Weijer, M. Schleicher, R. Albrecht and A.A. Noegel, *The role of the cortical cytoskeleton: F-actin crosslinking proteins protect against osmotic stress, ensure cell size, cell shape and motility, and contribute to phagocytosis and development*, J Cell Sci **109**, 2679-2691 (1996).

[40] G. Salbreux, J. Prost, J. F. Joanny, *Hydrodynamics of Cellular Cortical Flows and the Formation of Contractile Rings*, Phys. Rev. Lett. **103**, 058102 (2009).

[41] T. D. Pollard, J. A. Cooper, *Actin and actin-binding proteins. A critical evaluation of mechanisms and function*, Annu. Rev. Biochem **55**, 987-1035 (1986).

[42] T. D. Pollard, L. Blanchoin, R. D. Mullins, *Molecular mechanisms controlling actin filament dynamics in non-muscle cells*, Annu. Rev. Biophys. and Biomol. Struct. **29**, 545-576 (2000).

[43] A. Ott, M. Magnasco, A. Simon, and A. Libchaber, *Measurement of the persistence length of polymerized actin using fluorescence microscopy*, Phys. Rev. E **48**, R1642-R1645 (1993).

[44] F Gittes, B Mickey, J Nettleton, and J Howard, *Flexural rigidity of microtubules and actin filaments measured from thermal fluctuations in shape*, JCB **120**, 923 (1993).

[45] A. Wegner, *Treadmilling of actin at physiological salt concentrations : An analysis of the critical concentrations of actin filaments*, Journal of Molecular Biology **161**, 607-615 (1982).

[46] T. D. Pollard, G. G. Borisy, *Cellular Motility Driven by Assembly and Disassembly of Actin Filaments*, Cell **113**, 549 (2003).

[47] J. W. Sanger *Changing patterns of actin localization during cell division*, Proc. Natl. Acad. Sci. USA **72**, 1913-1916 (1975).

[48] V. Hunyadi, D.Chretien, H. Flyvbjerg and I. M. Janosi, *Why is microtubule lattice helical*, Biol. Cell **99**, 117-128 (2007).

[49] E. Nogales, S. G. W. and K. H. Downing, *Structure of the a-b tubulin dimer by electron crystallography*, Nature **391**, 199-203 (1998).

[50] J. A. Kaltschmidt and A. H. Brand, *Asymmetric cell division: microtubule dynamics and spindle asymmetry*, J Cell Sci **115**, 2257-2264, (2002).

[51] S. W. Grill, J. Howard, E. Schäffer, E. H. K. Stelzer, A. A. Hyman, *The distribution of active force generators controls mitotic spindle position,* Science **301**, 51-52 (2003).

[52] Chad G. Pearson and Kerry Bloom, *Dynamic microtubules lead the way for spindle positioning*, Nature Reviews Molecular Cell Biology **5**, 481-492 (2004).

[53] M. Clarke, J.A. Spudich, *Non-muscle contractile proteins: the role of actin and myosin in cell motility and shape determination*, Annu. Rev. Biochem. **46**, 797-822 (1977).

[54] R. D. Vale, *The molecular motor toolbox for intracellular transport*, Cell **112**, (2003).

[55] A. E. Carlson, *Contractile stress generation by actomyosin gels*, Phys. Rev. E. Stat. Nonlinear Soft Matter Phys. **74**, 051912 (2006).

[56] R. Voituriez, J. F. Joanny, J. Prost, *Spontaneous flow transition in active polar gels*, Europhys. Lett. **96**, 028102 (2005).

[57] S. Brenner, *The Genetics of Caenorhabditis elegans*, Genetics **77**, 71-94 (1977).

[58] W. B. Wood, *The Nematode Caenorhabditis elegans.* Cold Spring Harbor Laboratory Press (1988).

[59] WormBook is a comprehensive, open-access collection of original, peer-reviewed chapters covering topics related to the biology of *Caenorhabditis elegans* and other nematodes, accessible at wormbook.org .

[60] Andrew Fire, SiQun Xu, Mary K. Montgomery, Steven A. Kostas, Samuel E. Driver and Craig C. Mello, *Potent and specific genetic interference by double-stranded RNA in Caenorhabditis elegans.* Nature **391**, 806-811 (1998).

[61] Ravi S. Kamath et al., *Systematic functional analysis of the Caenorhabditis elegans genome using RNAi*, Nature **421**, 231-236 (2003).

[62] J. S. Bois, F. Jülicher, S. W. Grill, *Pattern formation in active fluids*, Phys. Rev. Lett. **106**, 028103 (2011).

[63] J E Sulston, H R Horvitz, *Post-embryonic cell lineages of the nematode, Caenorhabditis elegans,* Developmental Biology **56**, (1977).

[64] Carrie R. Cowan and Anthony A. Hyman, *Asymmetric cell division in C. elegans: Cortical polarity and spindle positioning*, Annu. Rev. Cell Dev. Biol. **20**, 427-453 (2004).

[65] Juergen A. Knoblich, *Asymmetric cell division during animal development*, Nature Rev. Mol. Cell. Biol. **2**, (2001).

[66] Na. W. Goehring,P. Khuc Trong, J. S. Bois, D. Chowdhury, E. M. Nicola, A A. Hyman, S. W. Grill, *Polarization of PAR proteins by advective triggering of a pattern-forming system*, Science **334**, (6059): 1137-1141 (2011).

[67] D. J. Smith, J. R. Blake, E. A. Gaffney, *Fluid mechanics of nodal flow due to embryonic primary cilia*, J. R. Soc. Interface **5**, 567-573 (2008).

[68] John Blake, *On the movement of mucus in the lung*, Journal of Biomechanics **8**, 179-190 (1975).

[69] Michael A. Sleigh, John R. Blake and Nadav Liron, *The propulsion of mucus by cilia*, Am. J. Respir. Crit. Care Med. **137**, 726-741 (1988).

[70] W. Curtis Worthington, Jr. and Robert S. Cathcart III, *Ependymal cilia: distribution and activity in the adult human brain*, Science **18**, 221-222 (1963).

[71] J. J. Essner, J. D. Amack, M. K. Nyholm, E. B. Harris, H. J. Yost, *Kupffer's vesicle is a ciliated organ of asymmetry in the zebrafish embryo that initiates left-right development of the brain, heart and gut*, Development **132**, 1247-1260 (2005).

[72] Y. Okada, S. Takeda, Y. Tanaka, J. C. Izpisúa Belmonte, N. Hirokawa, *Mechanism of nodal flow: a conserved symmetry breaking event in left-right axis determination*, Cell **121**, 633-644 (2005).

[73] R. Di Leonardo, D. Dell´ Arciprete, L. Angelani, and V. Iebba, *Swimming with an image.* Phys Rev. Lett **106**, 038101 (2011).

[74] Y. Wu, B. G. Hosu, H. C. Berg, *Micro-bubbles reveal chiral fluid flows in bacterial swarms*, Proc. Natl. Acad. Sci. USA **10**, 4147-4151 (2011).

[75] H. Noji, R. Yasuda, M. Yoshida, K. Kinosita Jr, *Direct observation of the rotation of F1-ATPase*, Nature **386**, 299-302 (1997).

[76] P. Lenz, J. F. Joanny, F. Jülicher, J. Prost, *Membranes with rotating motors*, Phys. Rev. Lett. **91**, 108104 (2003).

[77] J. C. Tsai, F. Ye, J. Rodriguez, J. P. Gollub, T. C. Lubensky, *A chiral granular gas*, Phys. Rev. Lett. **94**, 214301 (2005).

[78] P.M. Chaikin and T.C. Lubensky, *Principles of Condensed Matter Physics,* Cambridge University Press (2000).

[79] J. Toner and Y. Tu, *Long-range order in a two-dimensional dynamical XY model: how birds fly together,* Phys. Rev. Lett. **75**, 4326 (1995).

[80] Y. Tu and J. Toner, *Sound waves and the absence of galilean invariance in flocks*, Phys. Rev. Lett. 80, 48194822 (1998)

[81] J. Toner and Y. Tu, *Flocks, herds, and schools: A quantitative theory of flocking*, Phys. Rev. E **58**, 48284858 (1998)

[82] D. Marenduzzo, E. Orlandini, and J.M. Yeomans, *Hydrodynamics and rheology of active liquid crystals: a numerical investigation*, Phys. Rev. Lett. **98**, 118102 (2007).

[83] S.M. Fielding, D. Marenduzzo, and M.E. Cates, *Nonlinear dynamics and rheology of active fluids: Simulations in two dimensions,* Phys. Rev. E **83**, 041910 (2011).

[84] L. Giomi, L. Mahadevan, B. Chakraborty, M. F. Hagan, *Excitable patterns in active nematics,* Phys. Rev. Lett **106**, 218101 (2011).

[85] J. Elgeti, M. E. Cates, D. Marenduzzo, *Defect hydrodynamics in 2D polar active fluids,* Soft Matter **7**, 3177 (2011).

[86] S. Günther and K. Kruse, *Spontaneous waves in muscle fibres,* New J. Phys. **9**, 417 (2007).

[87] B. Shiladitya and M.C. Marchetti, *Instabilities and oscillations in isotropic active gels,* Soft Matter **7**, 463 (2011).

[88] J. Ranft, M. Basan, J. Elgeti, J.-F. Joanny, J. Prost and F. Jülicher, *Fluidization of tissues by cell division and apoptosis,* Proc. Natl. Acad. Sci. USA **107**, 20863 (2010).

[89] T. B. Liverpool and M. C. Marchetti, *Instabilities of isotropic solutions of active polar filaments,* Phys. Rev. Lett. **90**, 138102 (2003).

[90] I. S. Aranson and L. S. Tsimring, *Model of coarsening and vortex formation in vibrated granular rods,* Phys. Rev. E **67**, 021305 (2003).

[91] I. S. Aranson and L. S. Tsimring, *Theory of self-assembly of microtubules and motors* Rev. Mod. Phys. **78**, 641-692 (2006).

[92] M.C. Cross and P.C. Hohenberg, *Pattern formation outside of equilibrium,* Rev. Mod. Phys. **65**, 851 (1993).

[93] A. Groisman and V. Steinberg, *Elastic turbulence in a polymer solution flow,* Nature **405**, 53 (2000).

[94] A.N. Morozov and W. van Saarloos, *Subcritical finite-amplitude solutions for plane couette flow of viscoelastic fluids,* Phys. Rev. Lett. **95**, 024501 (2005).

[95] F. Jülicher and J. Prost, *Cooperative molecular motor,* Phys. Rev. Lett. **75**, 2618 (1995).

[96] J. Uhde, N. Ter-Oganessian, D. A. Pink, E. Sackmann, and A. Boulbitch, *Viscoelasticity of entangled actin networks studied by long-pulse magnetic bead microrheometry,* Phys. Rev. E **72**, 061916 (2005).

[97] F.C. MacKintosh, J. Käs, and P.A. Janmey, *Elasticity of semi-flexible biopolymer networks,* Phys. Rev. Lett. **75**, 4425 (1995).

[98] F. Gerbal, P. Chaikin, Y. Rabin, and J. Prost, *An elastic analysis of Listeria monocytogenes propulsion,* Biophys. J. **79**, 2259 (2000).

[99] M.L. Gardel, J.H. Shin, F.C. MacKintosh, L. Mahadevan, P. Matsudarai and D.A. Weitz, *Elastic behavior of cross-linked and bundled actin networks.* Science **304**, 1301 (2004).

[100] F. Wottawah, S. Schinkinger, B. Lincoln, R. Ananthakrishnan, M Romeyke, J. Guck, and J. Käs, *Optical rheology of biological cells*, Phys. Rev. Lett. **94**, 098103 (2005).

[101] R. Di Leonardo, L. Angelani, D. Dell'Arciprete, G. Ruocco, V. Iebba, S. Schippa, M. P. Conte, F. Mecarini, F. De Angelis, and E. Di Fabrizio, *Bacterial ratchet motors,* Proc. Natl. Acad. Sci. USA **107**, 9541 (2010).

[102] N. Uchida and R. Golestanian, *Synchronization and collective dynamics in a carpet of microfluidic rotors*, Phys. Rev. Lett. **104**, 178103 (2010).

[103] Maria Strempel, Sebastian Fürthauer, Stephan W. Grill, Frank Jülicher, *Thin films of chiral motors*, arXiv:1112.3492v2 [physics.bio-ph] (2011).

[104] M. D. Welch, R. D. Mullins, *Cellular control of actin nucleation*, Ann. Rev. Cell and Dev. Biol. **18**, 247-288 (2002).

[105] Richard D. Keane and Ronald J. Adrian, *Theory of cross-correlation analysis of PIV images.* Appl. Sci. Res. **49,** 191-215 (1993).

[106] T. Roesgen, *Optimal subpixel interpolation in particle image velocimetry,* Experiments in Fluids **35**, 252-256 (2003).

[107] C. Pohl, Z. Bao, *Chiral forces organize left-right patterning in C. elegans by uncoupling midline and anteroposterior axis,* Dev. Cell **19**, 402-412 (2010).

[108] R. Kuroda, B. Endo, M. Abe, M. Shimizu, *Chiral blastomere arrangement dictates zygotic left-right asymmetry pathway in snails,* Nature **462**, 08597 (2009).

[109] S. Schonegg and A. A. Hyman, *personal communication.*

[110] M. P. Stewart, J. Helenius, Y. Toyoda, S. P. Ramanathan, D. J. Muller and A. A. Hyman, *Hydrostatic pressure and the actomyosin cortex drive mitotic cell rounding,* Nature **469**, 226-230 (2011).

[111] A. Basu, J. F. Joanny, F. Jülicher and J. Prost, *Thermal and non-thermal fluctuations in active polar gels,* Eur. Phys. J. E **27**, 149-160 (2008).

[112] V. Schaller, C. Weber, C. Semmrich, E. Frey and A. R. Bausch, *Polar patterns of driven filaments.* Nature **467**, 73-77 (2010).

[113] D. Saintillan and M. J. Shelley, *Orientational order and instabilities in suspensions of self-locomoting rods,* Phys. Rev. Lett. **99**, 058102 (2007).

[114] D. Saintillan and M. J. Shelley, *Instabilities, pattern formation, and mixing in active suspensions,* Phys. Fluids **20**, 123304 (2008).

Acknowledgements

Versicherung

Hiermit versichere ich, dass ich die vorliegende Arbeit ohne unzulässige Hilfe Dritter und ohne Benutzung anderer als der angegebenen Hilfsmittel angefertigt habe; die aus fremden Quellen direkt oder indirekt übernommenen Gedanken sind als solche kenntlich gemacht. Die Arbeit wurde bisher weder im Inland noch im Ausland in gleicher oder ähnlicher Form einer anderen Prüfungsbehörde vorgelegt. Die vorliegende Arbeit wurde vom 01.04.2008 bis 26.03.2012 unter der Aufsicht von Prof. Dr. Frank Jülicher und Dr. Stephan Grill am Max-Planck-Institut für Physik komplexer Systeme und am Max-Planck-Institut für molekulare Zellbiologie und Genetik in Dresden durchgeführt.

Ich versichere, dass ich bisher keine erfolglosen Promotionsverfahren unternommen habe. Ich erkenne die Promotionsordnung der Fakultät Mathematik und Naturwissenschaften der Technischen Universität Dresden an.

Dresden, den 26.03.2012, Sebastian Fürthauer